

Quantum transport through single molecules

Quantum transport through single molecules

Proefschrift

ter verkrijging van de graad van doctor
aan de Technische Universiteit Delft,
op gezag van de Rector Magnificus prof. dr. ir. J. T. Fokkema,
voorzitter van het College voor Promoties,
in het openbaar te verdedigen op dinsdag 7 april 2009 om 15.00 uur

door

Edgar Alberto OSORIO OLIVEROS

Master of Science in Physics, University of Orsay, Paris, France
geboren te Cali, Colombia.

Dit proefschrift is goedgekeurd door de promotor:

Prof. dr. ir. H. S. J. van der Zant

Samenstelling van de promotiecommissie:

Rector Magnificus,	voorzitter
Prof. dr. ir. H. S. J. van der Zant	Technische Universiteit Delft, promotor
Prof. dr. ir. J. E. Mooij	Technische Universiteit Delft
Prof. dr. ir. L. P. Kouwenhoven	Technische Universiteit Delft
Prof. dr. M. R. Wegewijs	RWTH Aachen
Prof. dr. J. van Esch	Technische Universiteit Delft
Dr. M. Ruben	Forschungszentrum Karlsruhe
Dr. ir. S. J. van der Molen	Leiden Universiteit



Keywords: single-molecule junction, three-terminal transport, vibrational modes, electronic excitations.

Cover design: E. A. Osorio

Front & back: Conductance map of an OPV-5 molecular junction.

Printed by: Ipskamp Drukkers B.V, Enschede, The Netherlands

Copyright © 2009 by E. A. Osorio Oliveros

Casimir PhD Series, Delft-Leiden 2009-02

ISBN 978-90-8593-050-1

Contents

1	Introduction to single-molecule electronics	1
1.1	Molecular electronics	2
1.2	Making contact to a single molecule	2
1.3	Transport through single molecules: the three-terminal approach	4
1.4	Are we measuring a molecule?	7
1.5	Contacting single molecules with gold nanorods	8
1.6	Thesis outline	10
	References	11
2	Theory, device fabrication and measurement techniques	15
2.1	Transport through molecular junctions	16
2.1.1	Weak-coupling regime	17
2.1.2	Intermediate coupling: cotunneling and Kondo effect	18
2.1.3	Vibrational effects	21
2.2	Three-terminal device fabrication	23
2.3	Electromigration and gap fabrication	23
2.4	Molecule-junction preparation and characterization	24
	References	27
3	Vibrational modes of a single OPV-5 molecule	33
3.1	Introduction	34
3.2	Sample preparation	34
3.3	Characterization and statistics	35
3.4	Addition energies and vibrational modes	37
3.5	Conclusion	40
	References	40
4	Electronic excitations of a single OPV-5 molecule	43
4.1	Introduction	44
4.2	Experiment details	44
4.3	Results	47
4.4	Conclusion	53
	Appendix	53

A.1	Addition energies and excitations	53
A.2	Negative Differential Resistance effect. <i>Maarten Wegewijs.</i>	54
A.3	Effective model for $N = 2$: Finite-bias singlet-triplet Kondo effect. <i>Jens Paaske.</i>	56
A.4	Stability diagram after transferring the probe to another dewar	61
	References	61
5	Electrical manipulation of spin states in a single gated transition-metal complex	65
5.1	Introduction	66
5.2	Experimental details and results	66
5.3	Conclusion	71
	Appendix	73
A.1	Molecule synthesis and characterization. <i>University of Copenhagen</i>	73
A.2	Assignment of the low-bias features: two molecules in parallel.	74
A.3	Details on the assignment of spin states.	77
A.4	Enhanced cotunneling near the singlet-triplet degeneracy. <i>J. Paaske and K. Flensberg.</i>	78
A.5	Kondo effects: Magnetic field and temperature dependence.	81
	References	83
6	Switching in molecular junctions containing a Co-based grid molecule	87
6.1	Introduction	88
6.2	Experiment details	88
6.3	Results and discussions	89
6.3.1	Vibrational excitations	89
6.3.2	Switching	91
	Appendix	95
A.1	Switching in a single-Mn atom molecular complex	95
	References	97
7	Three-terminal transport through two capacitively coupled dots in parallel: comparison to experiment	101
7.1	Introduction	102
7.2	Parallel double-dot system	102
7.3	Rate equation approach	105
7.4	Comparison with experiments	106
7.5	Non-equilibrium Green's function approach	111
	References	113
	Summary	115

Samenvatting	119
Curriculum Vitae	123
List of Publications	125

Chapter 1

Introduction to single-molecule electronics

1.1 Molecular electronics

Si-based technology will run into severe physical and economic limitations in the long term [1]. From the financial standpoint, miniaturization of the current silicon devices implies a non-negligible cost increase as this requires the construction of new fabrication lines for each generation of chips. On the other hand, physical limitations include the requirement of oxide layers to be at least four to five atom thick which are inadequately insulating, thereby resulting in leakage currents. Moreover, fundamental limits derived from quantum mechanics appear as the electronic components shrink in size. One alternative to the top-down approach of silicon device fabrication that has been put forward as the ultimate miniaturization of logic devices consist in using molecules as building blocks for electronic switches and storage elements. Molecular construction of computational circuitry would have the appealing characteristic of taking advantage of self-assembly properties at the nanometer scale in order to build in a fast and cost-efficient way complex circuitry. Furthermore, as the physical properties of molecules can be tailored by chemical synthesis this would offer the possibility of engineering specific electronic functionalities such as diode, switch or memory effects.

The first ideas to use molecules as building blocks to perform electronic functions were put forward in 1974. Aviram and Ratner thought at that time that a molecule with a donor-acceptor structure would exhibit a diode-like I - V characteristic [2]. Since then a new field with fast growing interest, named *Molecular Electronics* was born. It should be noted that the definition of *Molecular Electronics* does not englobe research in which films or crystals with specific dielectric or electronic conduction properties are employed; in such case these amorphous or polycrystalline structures contain trillions of molecules. For this, scientist have rather suggested the terminology of molecular materials for electronics. In short, molecular electronics deals with single molecular systems in which individual molecules are thought as the fundamental unit of future computational components.

The development of molecular electronics in the past decades has been possible due to the invention and advances of scanning probe techniques as well as to progress in micro- and nanotechnology processes which have allowed manipulation and operation down to the atomic level. For instance, the work presented in this thesis would not have been possible without the use of current electron beam lithography techniques, crucial for the fabrication of devices which allow us to probe electrical transport through single molecules.

1.2 Making contact to a single molecule

One of the obvious questions that arises when thinking about molecular electronics is: How do we make contact to a single molecule? Given the size of a molecule, typically few nanometers, it is necessary to be able to build a pair of electrodes with nanometer-sized spacing if we want to drive a current through individual molecules. The first successful attempts [3] to measure electrical transport through single molecules were possible thanks to the development of scanning probe methods such as scanning tunneling microscopes

(STM) and atomic force microscopes (AFM).

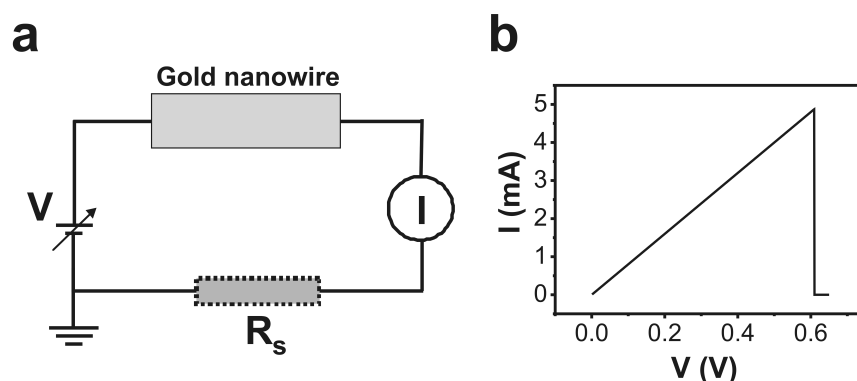


Figure 1.1: **a**, Electrical circuit used to break a thin gold wire. R_s denotes the series resistance in the circuit. **b**, “Break curve” for a gold nanowire. The current, I , is measured as a function of the voltage, V , which is ramped linearly in time.

In this thesis we used electromigration [4–6] of thin gold wires in order to fabricate the nanometer scale gaps required to trap single molecules. Electromigration is a process that has been studied extensively in the past to prevent failure of wires in microelectronics [5–7]. When a current density flows through a thin conducting wire scattered electrons transfer momentum to the atoms of the lattice. If this current density is large enough, metal atoms start to move under the effect of a large number of collisions with the electrons. This process, known as electromigration, leads eventually to the “breaking” of the wire in two physically separated electrodes with a spacing typically of few nanometers. Electromigration-induced nanogap formation has been imaged in situ by transmission (and scanning) electron microscopy [8, 9].

The simplest way of creating an electromigrated nanogap consists of ramping a voltage across a thin wire until failure; figure 1.1a illustrates the electronic circuit used for this purpose. As shown in figure 1.1b, the current through the gold wire increases by ramping the voltage of the source, and above a certain threshold value the current drops rapidly down to zero indicating the wire has broken. In figure 1.2 we present SEM images of a device before and after the electromigration has been carried out. It is important to note that although some control has been obtained over the electromigration process by using a feedback mechanism, the resulting nanogap geometry or size remains uncontrollable.

Once a gap has been made by electromigration, the molecular wire needs to bridge the gap as illustrated in figure 1.3. This can be done by depositing molecules which have suitable anchoring groups at both ends. A very frequently used one is the thiol group (-SH) which allows a covalent link between the sulfur atom and a Au atom from the electrode surface. For the deposition of molecules in the work presented in this thesis we have used solutions containing the molecule of interest. The nanogaps created by electromigration are exposed to these solutions, and it is expected that a molecule bridges a gap of a suitable size. This implies that a successful measurement depends much on such a “lucky event”,

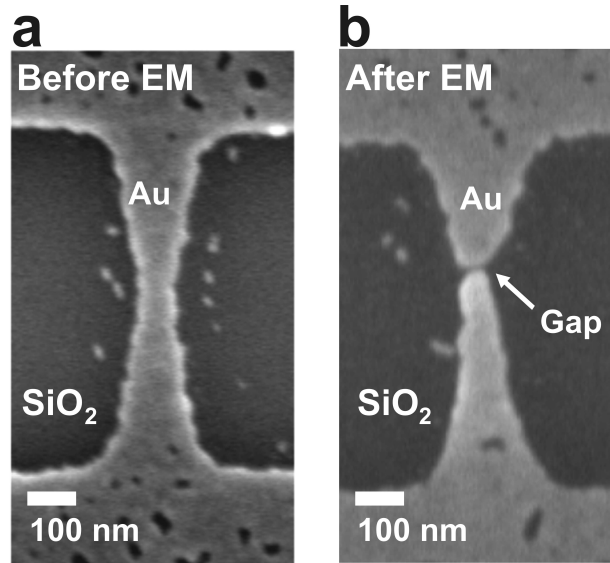


Figure 1.2: SEM images of thin gold wires on top a SiO₂ substrate before, **a**, and after electromigration, **b**. Note that the pictures do not belong to the same device

and that's why reported yields are low, in the order of few percent.

1.3 Transport through single molecules: the three-terminal approach

Transport through single molecules [10–14] is a field of intense investigation, and to date, several techniques are used to study transmolecular conduction; each with their advantages and disadvantages. For instance, scanning tunneling microscopy (STM) has proven to be a powerful tool for investigating inelastic electron tunneling spectroscopy (IETS) on single molecules [15–18]. STM offers imaging capabilities which allows spectroscopic studies in a well defined experimental geometry. Single molecules in planar three-terminal devices, on the other hand, cannot be imaged easily. Moreover, the coupling to the leads and the molecular environment can differ from sample to sample (same holds for two-terminal techniques such as mechanical break junctions). Nevertheless, the gate electrode in three-terminal devices -which is absent in STM and two-terminal techniques- allows studies in which the molecule can be oxidized or reduced; this makes them particularly interesting to study transmolecular conduction in different transport regimes. To be more specific, the third electrode can bring molecular levels into and out of resonance with the Fermi energy of the electrodes probing excited states and allowing different charge states to be accessed. Excited states can either be vibrational [19–21], electronic [22] or related to spin transitions [23, 24]. These excitations serve as a fingerprint of the molecule under study. Furthermore, three-terminal devices allow the determination of addition energies in

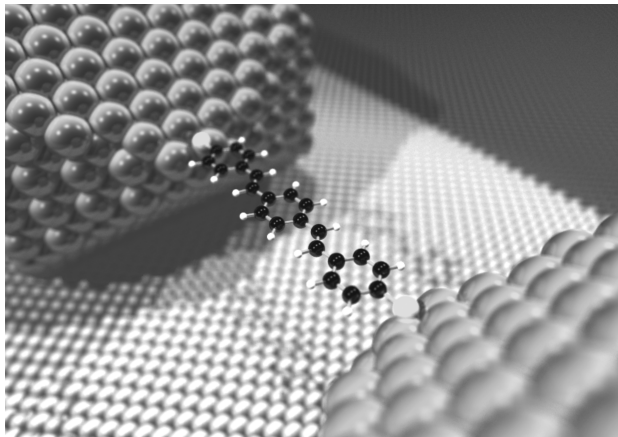


Figure 1.3: Artistic impression of an OPV-3 molecule bridging an electromigrated gap.

single-molecule junctions. Although it is possible to perform spectroscopy studies in two-terminal techniques [25], accurate estimates of the addition energies are hard to obtain if consecutive charge states cannot be probed.

The shift at which the orbital levels, E_n , can be moved up and down by the gate electrode potential, V_G , is quantified by the gate coupling parameter β . In an experiment, it should be as large as possible in order to access as many charge states as possible. The geometry plays an important role in the gate coupling and one should take care that the electrodes themselves do not screen the gate potential as this would decrease β . The electrode separation (and therefore the length of the molecule) and the break-through voltage of the gate oxide are other important parameters. Currently, two gate materials are frequently used: heavily doped silicon substrates with thermally grown SiO_2 on top and aluminum strips with a native Al_2O_3 oxide of only a few nanometers. For aluminum gates with an oxide thickness of 3 nm, the gate coupling is about 0.1 (for samples in which transport is attributed to transport through single molecules) so that with a typical break-through voltage of 4 V at low temperatures, the potential of the molecular levels can be shifted by ± 0.4 eV. On the other hand for silicon devices with an SiO_2 thickness of 250 nm, the gate coupling is about 10^{-3} . With a typical breakthrough voltage of 100 V, the range over which the potential on the molecule can be varied equals ± 0.1 eV.

Three-terminal devices have been fabricated using different techniques. They notably differ in the way the nanogap or the molecular junction is created. As mentioned above, we use the electromigration technique in order to form nanometer spaced electrodes. By using standard electron-beam lithography, several of these electrodes pairs can be fabricated on top of a conducting substrate (coated by an insulating layer) which can then serve as a gate electrode. The advantage of electromigrated devices on a $\text{Al}/\text{Al}_2\text{O}_3$ gate electrode is their large gate coupling ($\beta_{MAX} \sim 0.27$). The planar geometry (see figure 1.4a) offers a large stability for systematic studies as a function of gate voltage, temperature and magnetic

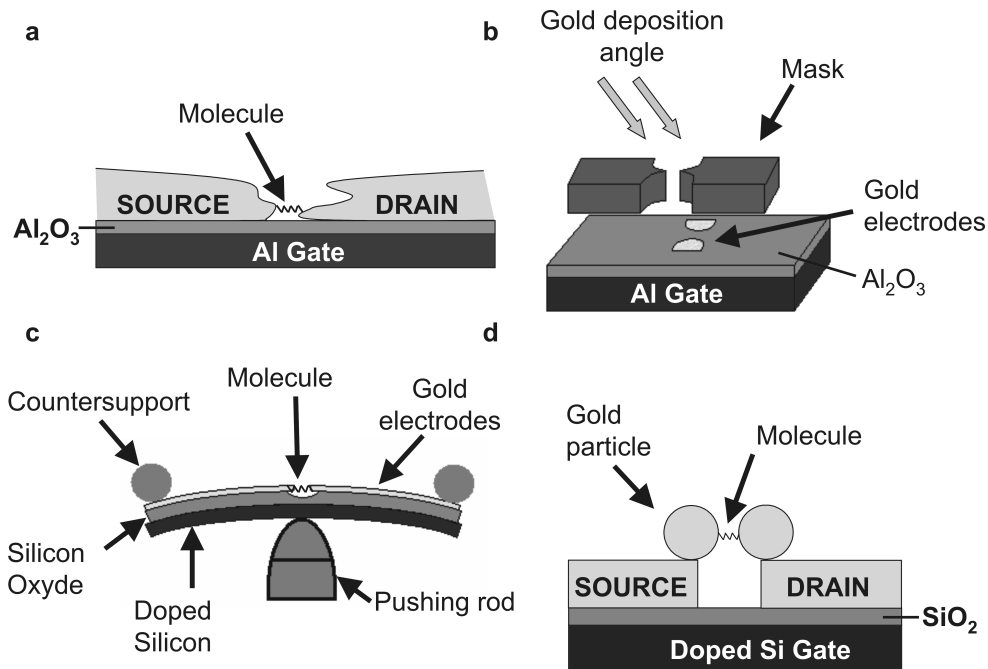


Figure 1.4: Schematic diagrams of different three-terminal device techniques. **a**, Electromigrated thin metal wire on top of a $\text{Al}/\text{Al}_2\text{O}_3$ gate electrode. **b**, Angle evaporation technique to fabricate planar electrodes with nanometer separation on top of a $\text{Al}/\text{Al}_2\text{O}_3$ gate electrode. **c**, Gated mechanical break junction. **d**, The dimer contacting scheme (see text).

field. Molecules are deposited from solution either prior to gap formation or afterwards.

A second technique involves the fabrication -on top of a gate electrode- of two gold electrodes using a shadow mask technique as illustrated in figure 1.4b. If the tilt angle of evaporation is high there is no overlap between the source and drain shadows. Reducing the tilt angle decreases the source-drain gap. In-situ measurements of the conductance allows for fine tuning of the gap distance when performed at low temperatures ($\sim 4.2\text{K}$). Molecules are subsequently deposited by quench condensation without disruption of the vacuum [26, 27]. The advantages of this evaporation technique include all the ones from the electromigrated devices, plus the control over the gap distance and the ability of molecule deposition inside a clean environment. Typical gate-coupling values are of the same order as the ones for electromigrated junctions.

Only recently it has been possible to integrate a gate electrode in mechanical controllable break junctions (MCBJs) [28]. In a MCBJ, suspended metallic wires with predefined breaking points are patterned on top of a bendable substrate (see figure 1.4c). By bending the substrate in a three point support, the metallic wire can be broken in two electrodes; the gap distance can then be tuned with picometer resolution. So far it has been possible to place the gate electrode from the gap at a distance of 40 nm [28]. Although the gate coupling remains low as compared to other techniques with a planar geometry ($\beta \sim 0.006$ in reference [28] with a reported break-through voltage of 12 V), MCBJ have the clear

advantage of precise control over the gap distance. Molecule deposition is carried out from solution.

Another three-terminal approach was recently reported by Dadosh *et al* [29]. Their method is based on synthesizing in solution a dimer structure consisting of two colloidal gold particles connected by a dithiolated molecule. The dimer is then electrostatically trapped between two gold electrodes defined on top of a gate electrode (see figure 1.4d). According to the authors, this dimer-based contacting scheme provides several advantages such as the ability to fabricate single-molecule devices with high certainty in which the contacts to the molecule are well defined. The gold particles in this setup, however, efficiently screen the gate potential. Moreover at low temperatures, spectroscopic features of the gold particles were sometimes observed to be superimposed on the characteristics of the molecule conduction.

1.4 Are we measuring a molecule?

Techniques like STM offer the possibility of imaging what is being measured. In most of the existing three terminal devices such capability does not exist¹ and one has to rely on the interpretation of electrical (or optical) measurements in order to conclude whether we are measuring a single molecule or not, even if we are measuring a molecule at all. The situation gets even more complicated with electromigrated three-terminal junctions since it is known that electromigration can lead to the formation of small metallic grains inside the gap which can display conduction characteristic comparable to that of molecules. Therefore the always recurring question can be asked: are we measuring transport through a molecule or a gold grain? In this thesis key elements to answer this question are discussed. In some cases the measurements show that transport is indeed taking place through a molecule rather than a gold grain or vice versa. In some other cases it is impossible to make definite statement about this issue.

Another approach consists of improving the fabrication scheme such that the formation of small metallic particles can be avoided. It has been shown that to a certain extent electromigration can be controlled [31, 32]. By use of fast electronics, it is possible to stop (continue) in time the electromigration process. It is therefore possible to narrow a gold wire such as the one presented in figure 1.2a down to a few atoms with high reproducibility. We've noticed through the work carried out in this thesis, that gold nanowires narrowed in this way and left unperturbed, i.e., with no voltages applied, "self-break" after some time (minutes or hours) [32]. Figure 1.5 shows the conductance versus time of such a gold nanowire at room temperature when initially narrowed to 2 k Ω . Although very little has been reported about the self-breaking mechanism [32, 33], we believe that residual stress in the narrowed wire after electromigration in combination with the high mobility of gold at room temperature are the driving forces behind it. Interestingly, we have found that

¹One exception, however, is the work presented by Soldatov *et al.* (1996) in which a STM was used together with a gold gate electrode in order to study transport through a single carborane cluster molecule [30].

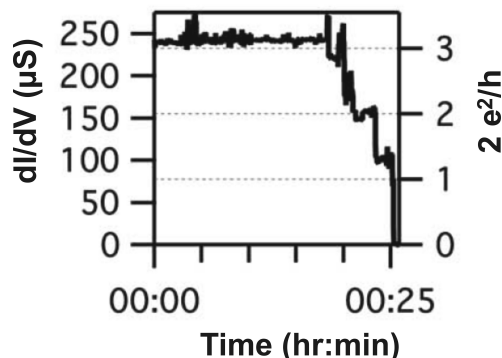


Figure 1.5: Self-breaking data in which conductance (in S on the left axis and conductance quanta $2e^2/h$ on the right axis) is plotted against time (in hours and minutes), measured at room temperature.

the formation of gold clusters is largely reduced in these self-broken junctions and more details can be found in chapter 2.

With this self-breaking technique, one route to discriminate transmolecular transport from transport through gold grains would be to characterize first the bare electromigrated nanogaps and then characterize the same junctions after the deposition of molecules. The first characterization would require to cool down the junction to cryogenic temperatures. The junctions are then warmed up in order to do the molecule deposition from solution and cooled down once again for a second characterization. This sounds like an ideal method on how to proceed but gold electromigrated gaps are unstable at room temperature: the conductance decreases in time by orders of magnitude, i.e., the gap size increases. Thus, this method would require stable gaps at room temperature or the ability of depositing the molecules at low temperatures since gold electromigrated junctions are stable below 200 K. The latter would require to implement inside a ^4He cryostat a small unit which sublimates the molecules of interest.

1.5 Contacting single molecules with gold nanorods

Present single-molecule devices have some serious drawbacks that hampers progress in device fabrication and electronic studies thereof: the contacts are generally not stable at room temperature and they are fabricated with a low yield and poor reproducibility. To a large extent this is due to the ill-defined electrode geometry and the uncontrolled introduction of molecules between the electrodes, which is usually performed by spontaneous adsorption from molecular solution to a pre-prepared electrode geometry. The resulting limitations can be summarized as follows: (i) the molecular attachment location remains unknown and control over the number and orientation of the adsorbed molecules is not possible (ii) the local geometry of the electrode-molecule contact remains unknown (iii) verification or characterization by other, independent methods is impossible for the same sample, or has limited value because of the many uncertainties mentioned above. There is

thus an urgent need to develop alternative approaches for the preparation of molecular electronic devices which allow for a large flexibility in the device configuration in combination with good yields and reproducibility.

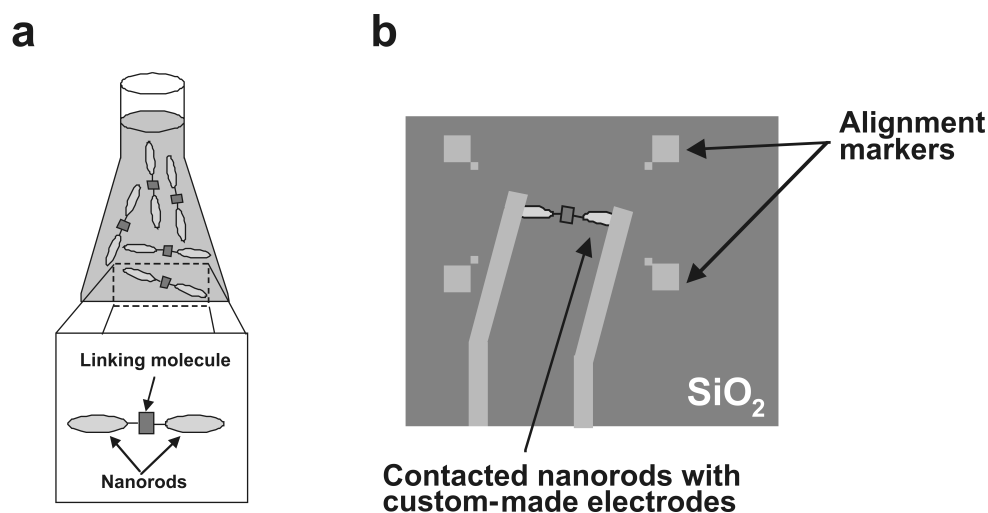


Figure 1.6: **a**, Linked nanorods by a molecule in solution. **b**, Contacted nanorods assemblies by custom made electrodes.

We started therefore working on a new scheme in which self-assembly and top-down fabrication techniques are combined, which allows for the controlled fabrication of stable and complex devices down to the single-molecule level. In short the idea consists of synthesizing gold nanorods with a diameter of a few nanometers, which are end-to-end connected by the molecules of interest (figure 1.6a). We plan to contact the nanorods with macroscopic electrodes and measure three-terminal transport through the molecule assemblies or single molecules that bridge the nanorods (figure 1.6b). The advantages of the method are (i) the contact distance is determined by the molecules, (ii) the nanorods are crystalline resulting in stable contacts at room temperature and (iii) the nanorod assemblies can be characterized by independent methods (optical for instance). This method will enable new research directions in the field of multi-terminal molecular devices, single-molecule surface enhanced Raman spectroscopy and room-temperature sensors.

At the chemistry department in Delft (Delft Chem Tech), we have synthesized gold nanorods according to previously reported methods [34]. Preliminary results have shown that it is possible to make a reliable low ohmic contact to a single nanorod by using standard e-beam lithography techniques. Figure 1.7a shows a SEM image of a gold nanorod contacted by two electrodes; the resistance measured in this device was 180 Ohms and figure 1.7b shows its I - V characteristic. Work towards linking nanorods is still in progress but has given as well some preliminary results (see figure 1.8).

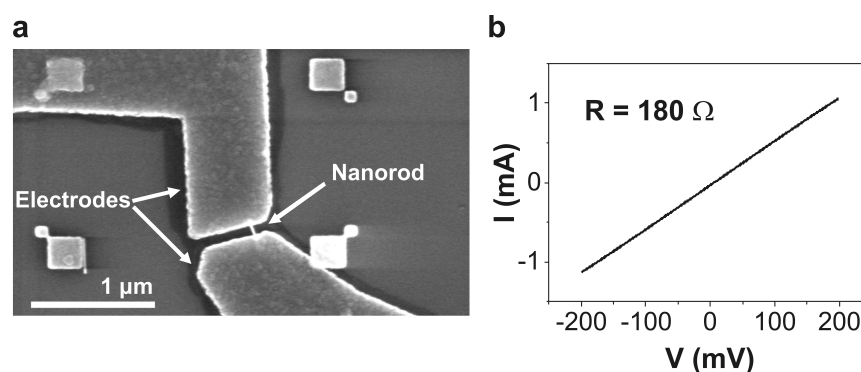


Figure 1.7: **a**, Contacted single rod by gold electrodes. **b**, Current, I , versus voltage, V , characteristic of the rod contacted in **a**.

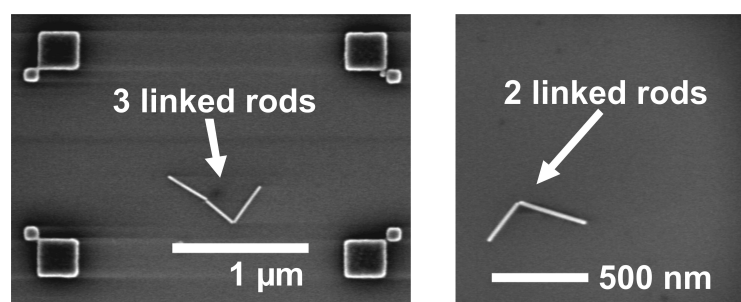


Figure 1.8: SEM pictures of linked rods.

1.6 Thesis outline

The content of this Thesis is outlined below:

Chapter 2: This chapter gives an introduction to the theoretical concepts used throughout this work. We start by discussing Coulomb blockade and the constant interaction model (CIM). We then discuss two different transport regimes, the weak and intermediate coupling limits. Next we describe our sample fabrication, and we detail how we prepare and characterize our molecular junctions.

Chapter 3: This chapter presents measurement carried out on OPV-5 molecular junctions. We show clear evidence of molecular vibration excitations in a weakly coupled junction and we corroborate that addition energies of OPV-5, placed in metallic nanogaps, are reduced relative to the energy scale set by the optical HOMO-LUMO gap.

Chapter 4: If the molecule is intermediately coupled to the source, and drain-electrodes, higher-order tunnelling processes also become important and one enters a new regime of correlated transport, exhibiting many-body effects such as the Kondo-effect. In this chapter we show that by performing temperature and magnetic field dependent measurements on these higher-order processes it is possible to infer the charge filling sequence in a

OPV-5 molecular junction. Experimental results show as well that the molecule-lead and molecule-gate couplings are dependent on the charge state of the molecular quantum dot. Furthermore we show that a conjugated molecule cannot be thought as a molecular wire since charges localize due to the role of image charges at the electrode-molecule interface.

Chapter 5: In this chapter, we study transport through another type of molecular system in which a Mn -ion is surrounded on either side by ligands. The transport measurements occur in the intermediate coupling regime and show that by changing the gate voltage the spin ground-state of the molecule can be tuned. We explain this finding by assuming that orbitals in the ligands and metal ion couple differently to the gate electrode. Calculations support our interpretation.

Chapter 6: Electrical switching in molecular junctions has attracted a lot of interest, but reports on the nature of the switching mechanism remain controversial. In this chapter we show that switching in junctions incorporating a grid type complex may be due to the presence of charged species in the vicinity of the molecular junction.

Chapter 7: Often, it happens that transport measurements in molecular junctions show features that cannot be explained by using a single dot framework. In this chapter we show that features, such as kinks in the diamond edges and switches, can be well reproduced by using a parallel double dot model in which the dots are only capacitively coupled to each other.

References

- [1] M. Schulz, "The end of the road for silicon?," *Nature*, vol. 399, no. 6738, pp. 729–730, 1999.
- [2] A. Aviram and M. A. Ratner, "Molecular rectifiers," *Chem. Phys. Lett.*, vol. 29, no. 2, pp. 277–283, 1974.
- [3] J. K. Gimzewski, E. Stoll, and R. R. Schlittler, "Scanning tunneling microscopy of individual molecules of copper phthalocyanine adsorbed on polycrystalline silver surfaces," *Surf. Sci.*, vol. 181, no. 1-2, pp. 267–277, 1987.
- [4] H. Park, A. K. L. Lim, A. P. Alivisatos, J. Park, and P. L. McEuen, "Fabrication of metallic electrodes with nanometer separation by electromigration," *Appl. Phys. Lett.*, vol. 75, no. 2, pp. 301–303, 1999.
- [5] P. S. Ho and T. Kwok, "Electromigration in metals," *Rep. Prog. Phys.*, vol. 52, no. 3, pp. 301–348, 1989.
- [6] J. R. Black, "Electromigration failure modes in aluminum metallization for semiconductor devices," *Proc. of the IEEE*, vol. 57, no. 9, pp. 1587–1594, 1969.
- [7] C. Durkan, M. A. Schneider, and M. E. Welland, "Analysis of failure mechanisms in electrically stressed Au nanowires," *J. Appl. Phys.*, vol. 86, no. 3, pp. 1280–1286, 1999.

-
- [8] H. B. Heersche, G. Lientschnig, K. O'Neill, H. S. J. van der Zant, and H. W. Zandbergen, "In situ imaging of electromigration-induced nanogap formation by transmission electron microscopy," *Appl. Phys. Lett.*, vol. 91, no. 7, p. 072107, 2007.
- [9] T. Taychatanapat, K. Bolotin, F. Kuemmeth, and D. Ralph, "Imaging electromigration during the formation of break junctions," *Nano Lett.*, vol. 7, no. 3, pp. 652–656, 2007.
- [10] D. Natelson, *Single molecule transistors. Handbook of organic electronics and photonics vol 3.* ed. H. S. Nalwa (Stevenson Ranch, CA: American Scientific Publishers), 2007.
- [11] A. Nitzan and M. A. Ratner, "Electron Transport in Molecular Wire Junctions," *Science*, vol. 300, no. 5624, pp. 1384–1389, 2003.
- [12] M. Paulsson and S. Stafström, "Self-consistent-field study of conduction through conjugated molecules," *Phys. Rev. B*, vol. 64, no. 3, p. 035416, 2001.
- [13] M. Di Ventra, S. T. Pantelides, and N. D. Lang, "First-principles calculation of transport properties of a molecular device," *Phys. Rev. Lett.*, vol. 84, no. 5, pp. 979–982, 2000.
- [14] M. Paulsson, F. Zahid, and S. Datta, "Resistance of a molecule," *cond-mat.*, no. 0208183, 2002.
- [15] X. H. Qiu, G. V. Nazin, and W. Ho, "Vibronic states in single molecule electron transport," *Phys. Rev. Lett.*, vol. 92, no. 20, p. 206102, 2004.
- [16] B. C. Stipe, M. A. Rezaei, and W. Ho, "Single-Molecule Vibrational Spectroscopy and Microscopy," *Science*, vol. 280, no. 5370, pp. 1732–1735, 1998.
- [17] B. C. Stipe, M. A. Rezaei, and W. Ho, "Coupling of vibrational excitation to the rotational motion of a single adsorbed molecule," *Phys. Rev. Lett.*, vol. 81, no. 6, pp. 1263–1266, 1998.
- [18] J. Gaudioso, H. J. Lee, and W. Ho, "Vibrational analysis of single molecule chemistry: Ethylene dehydrogenation on Ni(110)," *J. Am. Chem. Soc.*, vol. 121, no. 37, pp. 8479–8485, 1999.
- [19] E. A. Osorio, K. O'Neill, N. Stuhr-Hansen, O. F. Nielsen, T. Bjørnholm, and H. S. J. van der Zant, "Addition energies and vibrational fine structure measured in electromigrated single-molecule junctions based on an oligophenylenevinylene derivative," *Adv. Mater.*, vol. 19, no. 2, pp. 281–285, 2007.
- [20] L. H. Yu, Z. K. Keane, J. W. Ciszek, L. Cheng, M. P. Stewart, J. M. Tour, and D. Natelson, "Inelastic electron tunneling via molecular vibrations in single-molecule transistors," *Phys. Rev. Lett.*, vol. 93, no. 26, p. 266802, 2004.

- [21] H. Park, J. Park, A. K. L. Lim, E. H. Anderson, A. P. Alivisatos, and P. L. McEuen, "Nanomechanical oscillations in a single-C₆₀ transistor," *Nature*, vol. 407, no. 6800, pp. 57–60, 2000.
- [22] E. A. Osorio, K. O'Neill, M. Wegewijs, N. Stuhr-Hansen, J. Paaske, T. Bjørnholm, and H. S. J. van der Zant, "Electronic excitations of a single molecule contacted in a three-terminal configuration," *Nano Lett.*, vol. 7, no. 11, pp. 3336–3342, 2007.
- [23] H. B. Heersche, Z. de Groot, J. A. Folk, H. S. J. van der Zant, C. Romeike, M. R. Wegewijs, L. Zobbi, D. Barreca, E. Tondello, and A. Cornia, "Electron transport through single Mn₁₂ molecular magnets," *Phys. Rev. Lett.*, vol. 96, no. 20, p. 206801, 2006.
- [24] M.-H. Jo, J. Grose, K. Baheti, M. Deshmukh, J. Sokol, E. Rumberger, D. Hendrickson, J. Long, H. Park, and D. Ralph, "Signatures of molecular magnetism in single-molecule transport spectroscopy," *Nano Lett.*, vol. 6, no. 9, pp. 2014–2020, 2006.
- [25] R. H. M. Smit, Y. Noat, C. Untiedt, N. D. Lang, M. C. van Hemert, and J. M. van Ruitenbeek, "Measurement of the conductance of a hydrogen molecule," *Nature*, vol. 419, no. 6910, pp. 906–909, 2002.
- [26] S. Kubatkin, A. Danilov, M. Hjort, J. Cornil, J. L. Bredas, N. Stuhr-Hansen, P. Hedegård, and T. Bjørnholm, "Single-electron transistor of a single organic molecule with access to several redox states," *Nature*, vol. 425, no. 6959, pp. 698–701, 2003.
- [27] S. Kubatkin, A. Danilov, M. Hjort, J. Cornil, J.-L. Brdas, N. Stuhr-Hansen, P. Hedegård, and T. Bjørnholm, "Single electron transistor with a single conjugated molecule," *Curr. Appl. Phys.*, vol. 4, no. 5, pp. 554–558, 2004.
- [28] A. R. Champagne, A. N. Pasupathy, and D. C. Ralph, "Mechanically adjustable and electrically gated single-molecule transistors," *Nano Lett.*, vol. 5, no. 2, pp. 305–308, 2005.
- [29] T. Dadosh, Y. Gordin, R. Krahne, I. Khivrich, D. Mahalu, V. Frydman, J. Sperling, A. Yacoby, and I. Bar-Joseph, "Measurement of the conductance of single conjugated molecules," *Nature*, vol. 436, no. 7051, pp. 677–680.
- [30] E. S. Soldatov, V. V. Khanin, A. S. Trifonov, D. E. Presnov, S. A. Yakovenko, G. B. Khomutov, C. P. Gubin, and V. V. Kolesov, "Single-electron transistor based on a single cluster molecule at room temperature," *JETP. Lett.*, vol. 64, no. 7, pp. 556–560, 1996.
- [31] D. R. Strachan, D. E. Smith, D. E. Johnston, T.-H. Park, M. J. Therien, D. A. Bonnell, and A. T. Johnson, "Controlled fabrication of nanogaps in ambient environment for molecular electronics," *Appl. Phys. Lett.*, vol. 86, no. 4, p. 043109, 2005.

- [32] K. O'Neill, E. A. Osorio, and H. S. J. van der Zant, "Self-breaking in planar few-atom Au constrictions for nanometer-spaced electrodes," *Appl. Phys. Lett.*, vol. 90, no. 13, p. 133109, 2007.
- [33] M. Tsutsui, K. Shoji, M. Taniguchi, and T. Kawai, "Formation and self-breaking mechanism of stable atom-sized junctions," *Nano Lett.*, vol. 8, no. 1, pp. 345–349, 2008.
- [34] B. D. Busbee, S. O. Obare, and C. J. Murphy, "An improved synthesis of high-aspect-ratio gold nanorods," *Adv. Mat.*, vol. 15, no. 5, pp. 414–416, 2003.

Chapter 2

Theory, device fabrication and measurement techniques

Parts of this chapter were published as E. A. Osorio, T. Bjørnholm, J. M. Lehn, M. Ruben and H. S. J. van der Zant, *J. Phys.: Condens. Matter.* **20**, 374121 (2008)

2.1 Transport through molecular junctions

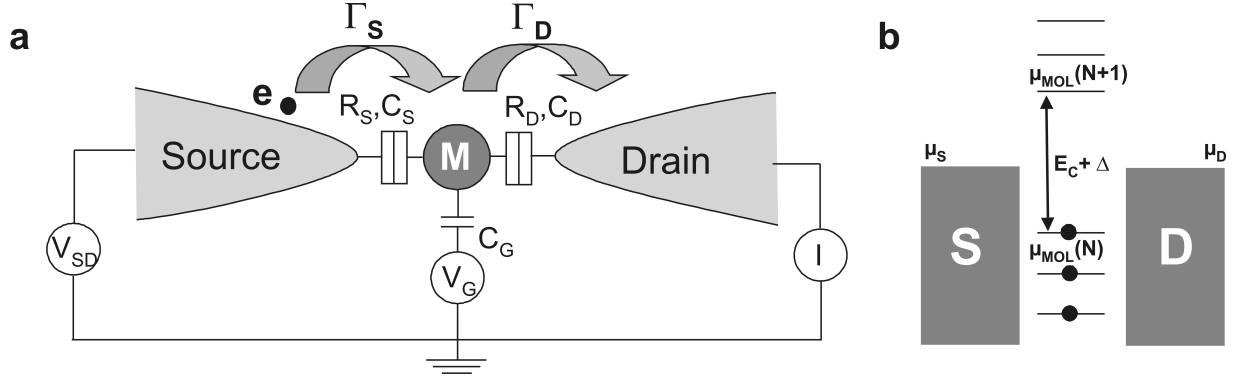


Figure 2.1: Schematic picture and energetics of a molecular quantum dot. **a**, The molecular quantum dot (represented by a disk “M”) is connected to source and drain contacts via tunnel barriers, allowing charge carriers to tunnel to and from the quantum dot. The current through the device, I , is measured in response to a bias voltage, V and a gate voltage, V_G . **b**, Electrochemical potentials $-\mu_{MOL}(N)$ for different electron numbers, with $\Delta(N)$ = level spacing, and E_C =charging energy.

In describing three-terminal transport through molecular junctions at cryogenic temperatures, the molecule is viewed as a confined electronic system –or quantum dot– coupled by tunneling barriers to source and drain electrodes as schematically shown in figure 2.1a [1–4]. The discrete electronic spectrum of such an object is illustrated in figure 2.1b; available states for transport are denoted by the electrochemical potential $\mu_{MOL}(N)$, which by definition is the minimum energy for adding the N th electron to the dot: $\mu_{MOL}(N) = U(N) - U(N - 1)$, where $U(N)$ is the total ground state energy for N electrons on the dot. The energy to add an extra electron or addition energy, E_{add} , equals the level spacing, $\Delta(N)$, plus the charging energy, E_C (see figure 2.1b). The latter quantity accounts for the Coulomb interactions between electrons in the dot and is defined as $E_C = e^2/C$. Here, C is the total capacitance to the “outside world”, i.e. $C = C_S + C_D + C_G$, where C_S is the capacitance to the source, C_D to the drain and C_G the capacitance to the gate. The overlap of the molecular wavefunction with that of the conduction electrons of the leads is described by the molecule-lead couplings Γ_S , Γ_D , which can be also related to the bare tunneling rates between the molecular level and each of the leads. The total coupling, $\Gamma = \Gamma_S + \Gamma_D$, is a measure of the resulting broadening of the molecular levels. In principle Γ can be charge-state dependent as the overlap between the wave functions of the metal electrodes and the molecule can vary strongly with N (i.e. $\Gamma = \Gamma(N)$).

At cryogenic temperatures, $E_C, \Delta \gg k_B T$ (thermal energy). Depending on the value of Γ with respect to these parameters, we can distinguish two regimes of special interest. We will shortly discuss both in the next two sections.

2.1.1 Weak-coupling regime

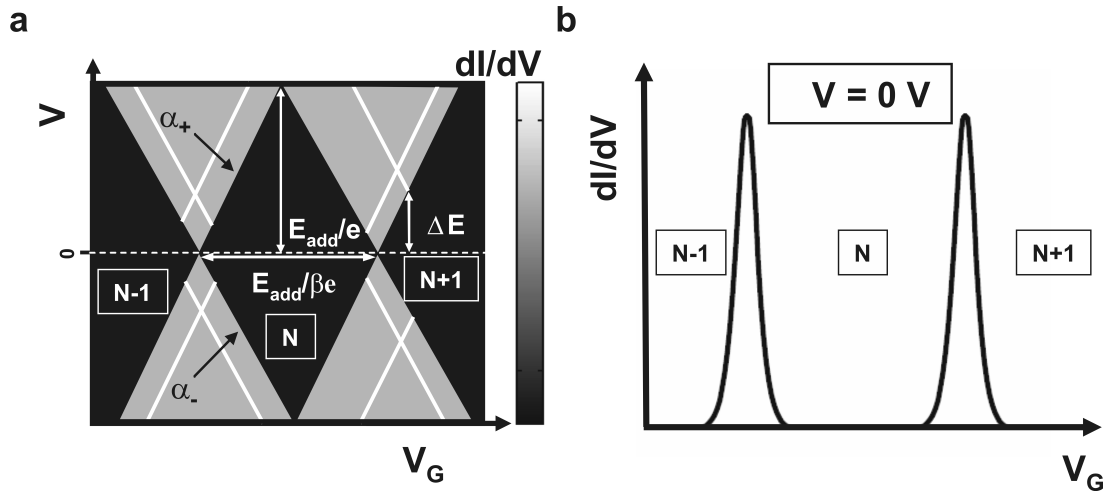


Figure 2.2: Electron transport through a weakly-coupled molecular quantum dot; the gate voltage probes three different charge states. **a**, Conductance map of the differential conductance, dI/dV , versus V and V_G (stability diagram). The edges of the diamond-shaped regions (black) correspond to the onset of current (gray). Diagonal lines emanating from the diamonds (white) indicate the onset of transport through excited states. **b**, Coulomb peaks in differential conductance, dI/dV , versus gate voltage in the linear-response regime (small bias voltage).

When Γ is very small ($\Gamma \ll E_C, \Delta$), one is in the weak coupling limit. Figure 2.2a schematically illustrates the result of a typical transport measurement in the form of a so-called stability diagram. Slanted lines separate regions of high conductance (single-electron tunneling (SET) regime, grey regions) from enclosed diamond-shaped regions (Coulomb diamonds) with almost¹ zero conductance (black regions). Inside the SET regime, lines running parallel to the diamond edges correspond to the onset at which excited states start contributing to the conductance; their energy, ΔE , can be read off as the distance from the zero-bias axis to the crossing point with the diamond edge as illustrated in figure 2.2a. Inside the black diamond-shaped regions the number of electrons on the molecule is fixed to an integer value. Between consecutive black regions (charge states) the charge on the molecule increases (decreases) by one unit as we go to more positive (negative) gate voltages. It should be noted that it is difficult to assign a particular charge state of the free molecule to these states. For instance, the charge state measured at zero bias and zero-gate voltage may not be the neutral charge state of the molecule. At zero bias, partial charging of the molecule can take place in order to equilibrate the chemical potentials across the junction. Background charges from electron-traps in the vicinity of the device may also introduce an offset in the level positions of the molecular quantum dot.

¹ In first order, the conductance is zero. Higher-order processes, however, lead to a finite current in this regime, which is negligible small if Γ is small.

Resonant tunneling, which is a first-order process, lifts Coulomb blockade. It occurs when a charge state, $\mu_{MOL}(N)$, lies in between the voltage-bias window defined by μ_S and μ_D . This can be done by independently sweeping the bias or gate voltage “towards” the grey regions where current starts flowing by a sequential tunneling process (charges are taken from the source to the molecule and subsequently from the molecule to the drain). Sweeping the gate voltage and measuring the differential conductance at low bias results in a series of peaks as shown in figure 2.2b. Each of these peaks represents a charge degeneracy point or Coulomb oscillation. At these points, the two charge states N ($N-1$) and $N+1$ (N) of the quantum dot have the same energy and hence an electron can hop on and off the dot freely.

The slopes of the diamond boundaries in figure 2.2a give quantitative information about the capacitances. Along the line with positive slope, $\alpha_+ = C_G/(C_G + C_D)$, the electrochemical potential level is aligned with the source and along the line with negative slope, $\alpha_- = -C_G/C_S$, it is aligned with the drain. The maximum extent of the diamond in V (V_G) is E_{add} ($E_{add}/\beta e$) as illustrated in figure 2.2a. The gate coupling defined as $\beta = C_G/C_\Sigma$ can either be determined from the diamond slopes ($\beta = \alpha_+\alpha_-/(\alpha_+ + \alpha_-)$) or by measuring the sizes of the diamond. From the conductance map it is also possible to determine the molecule-lead coupling Γ . One way of doing this, is to evaluate the full width at half maximum (FWHM) of the conductance peak along a diamond edge from the dI/dV versus V trace. In a similar way, the FWHM of the Coulomb peak (figure 2.2b) multiplied by β is a measure of Γ .

2.1.2 Intermediate coupling: cotunneling and Kondo effect

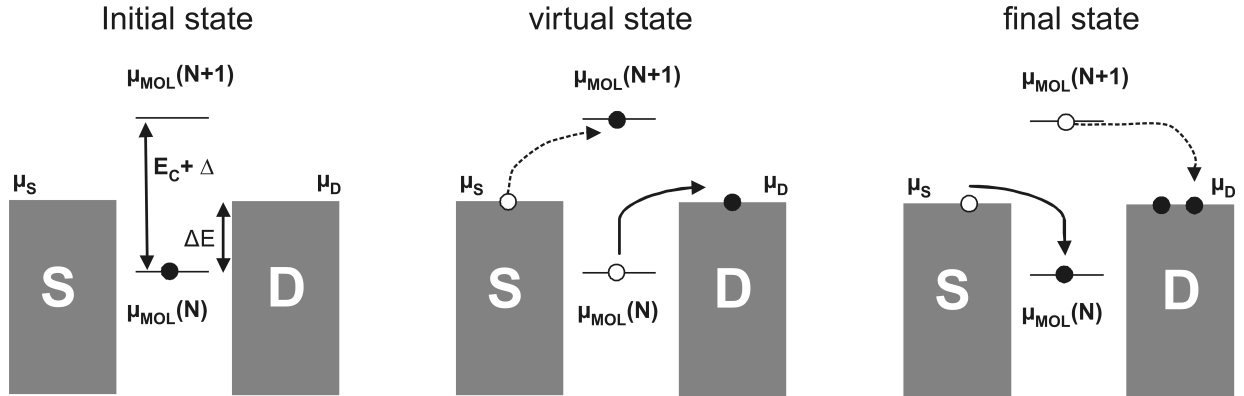


Figure 2.3: Elastic cotunneling. The N -th electron on the dot jumps to the drain (virtual state) to be immediately replaced (final state) by an electron from the source (solid arrows sequence). A similar process involves the unoccupied state (dashed arrows sequence). In both examples, an electron is effectively transported from source to drain.

Higher-order tunneling [5] processes become more apparent when the tunnel coupling, Γ , is enhanced. In the so-called strong coupling regime ($\Gamma \gg E_C, \Delta(N), k_B T$) the

electronic states on the dot and electrode are significantly hybridized, elastic coherent tunneling dominates transport and signatures of the Coulomb blockade are washed out by quantum fluctuations of the molecular charge; the resistance is close to the resistance quantum $R_Q = h/e^2 = 25.8 \text{ k}\Omega$. Between the weak coupling and strong coupling regimes we identify a third regime which we will refer as the intermediate coupling regime. In this regime it is still possible to observe Coulomb diamonds, but higher-order processes lead to a non-negligible current inside the blockade regions. In this section we will discuss three different types of higher-order tunneling processes: elastic cotunneling, the Kondo effect which is a particular elastic many-body effect, and inelastic cotunneling.

Figure 2.3 illustrates an elastic cotunneling process. Energy conservation forbids the number of electrons to change as this would cost an energy ΔE . Nevertheless, an electron can tunnel off the molecule, leaving it temporarily in a classically forbidden “virtual state” (middle diagram in figure 2.3). By virtue of Heisenberg’s energy-time uncertainty principle this is allowed, as long as another electron tunnels into the molecule in the same quantum process in order not to violate energy conservation. The final state then has the same energy as the initial one, but one electron has been transported through the molecule. This elastic cotunneling process is analogous to the superexchange mechanism in chemical electron transfer theory [6, 7]. It occurs at arbitrarily low bias as the energy of the tunneling electron and the molecule are unchanged, and it leads to a nonzero background conductance in the blockade regions.

If the electron spin is taken into account, one can encounter another elastic-cotunneling process connected to the Kondo effect [8–16]. Whenever a single localized state in the molecule is spin-degenerate and partially filled, the molecule has a net spin (magnetic moment). This for example occurs for an odd occupancy in the molecule (one electron is unpaired, $S=1/2$). We shall consider this simple case. The conduction mechanism for the Kondo effect involves spin-flip events such as the one illustrated in figure 2.4. We refer to other papers [17–22] for a more detailed theoretical discussion. Here, we concentrate on its main transport characteristics, which are summarized in figures 2.5 and 2.6.

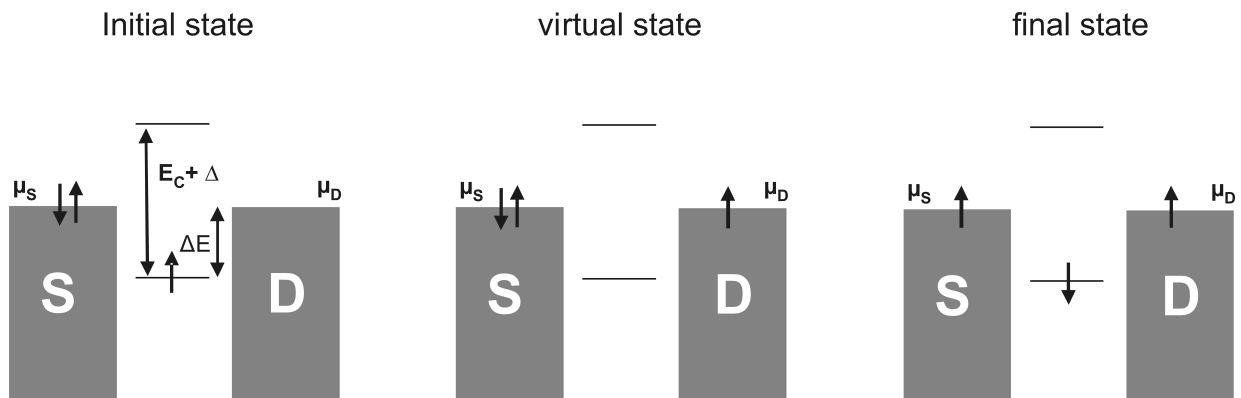


Figure 2.4: Spin-flip cotunneling. A spin-up electron jumps out of the dot (virtual state) to be immediately replaced by a spin-down electron (final state).

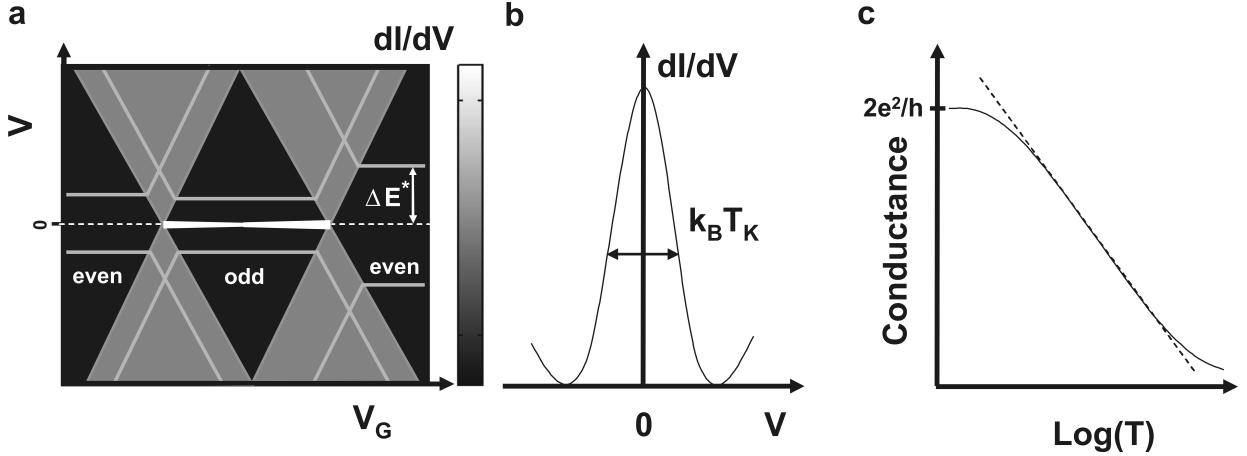


Figure 2.5: Schematic representation of the main characteristics of the Kondo effect in electron transport through a molecular quantum dot. **a**, In the stability diagram, the Kondo effect results in a zero-bias resonance (white line) for an odd number of electrons in the dot. Inelastic cotunneling excitations appear as lines running parallel to the gate axis at finite bias. **b**, For $T \ll T_K$, the full width at half maximum (FWHM) of the Kondo resonance is $\sim k_B T_K$. **c**, Temperature dependence of the Kondo-peak height in the middle of the Coulomb diamond.

For an odd number of electrons the stability plot shows a zero-bias resonance in the differential conductance, dI/dV , versus V , inside the Coulomb diamond “connecting” both degeneracy points as shown in figures 2.5a. For an even number of electrons with all spins paired, $S=0$ and there is no Kondo resonance. This even-odd-asymmetry is very helpful in assigning the parity of the charge state which can then add extra information to the understanding of the spectroscopic features observed in the stability plots. In the low temperature limit ($T \ll T_K$), the full width at half maximum (FWHM) of the Kondo resonance is of order $k_B T_K$ (see figure 2.5b). Typical Kondo temperatures are $T_K \sim 1\text{K}$ for semiconductor quantum dots [11], $T_K \sim 1\text{K}-10\text{K}$ for carbon nanotubes [23, 24] and $T_K \sim 20\text{K}-50\text{K}$ for molecular devices [13–16]. In the middle of the Coulomb diamond, the height of the Kondo-peak as function of temperature is expected to show the characteristic form [10, 11]:

$$G(T) = G_c + G_a [1 + (2^{1/s} - 1)(T/T_K)^2]^{-s} \quad (2.1)$$

where G_a is the maximum conductance, G_c is a temperature-independent offset and $s=0.22$ for $S=1/2$. This dependence is drawn in figure 2.5c and the characteristic features include a conductance that increases logarithmically with decreasing temperature, and saturates at a value $2e^2/h$ at the lowest temperatures in case of symmetric lead-dot coupling. The latter is commonly referred to as Kondo in the unitary limit [25]. In a magnetic field the Zeeman splitting of the Kondo resonance leads to the observation of two peaks symmetric in bias, separated by twice the Zeeman energy as schematically illustrated in figure 2.6a. Its evolution in a magnetic field is shown in figure 2.6b. Although we have only considered $S=1/2$, it is important to note that other types of Kondo systems are possible owing to

orbital degeneracies [26] or triplet states [27–29]; these can lead to a violation of the parity effect.

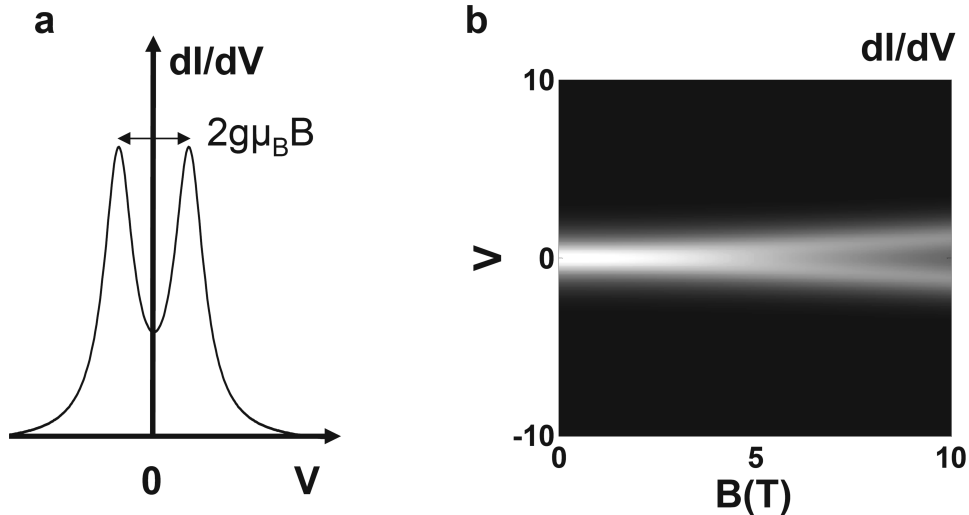


Figure 2.6: Characteristics of the Kondo effect in the presence of a magnetic field. **a**, Zeeman splitting of the Kondo resonance at finite magnetic field. **b**, Calculated gray scale plot of dI/dV versus V and B .

A cotunneling event that leaves the molecule in an excited state is called inelastic. An example of such a process is depicted in figure 2.7; as shown, the onset of the cotunneling event occurs at $eV = \Delta E^*$, the condition dictated by the energy conservation principle. In transport measurements, inelastic cotunneling appears in the stability diagram inside the Coulomb diamonds as two symmetric lines running parallel to the gate axis as represented by the grey lines in figure 2.5a; their energy, ΔE^* , is the distance of the excitation to the zero bias axis as illustrated in figure 2.5a. Furthermore the inelastic cotunneling line is expected to intersect, at the diamond boundary, the corresponding excitation line inside the SET region [30].

As a final remark, we note that higher-order coherent processes appear as sharp spectroscopic features as the conductance of the i -th order process is proportional to Γ_i . For first order incoherent single-electron tunneling, the current is proportional to Γ .

2.1.3 Vibrational effects

Molecules are “flexible” objects, and can for instance undergo conformational changes that can strongly affect transport behavior [31–33]; vibrational modes lie typically between a few meV to tens of hundred meV for free molecules. Inelastic effects in molecular junctions originate from coupling between electronic and nuclear degrees of freedom. The nuclei are much heavier than the electrons. Therefore the nuclear and electronic dynamics can be separated as is usually done in the Born-Oppenheimer approximation. The nuclear motion can be described by a series of uncoupled harmonic oscillators and for simplicity

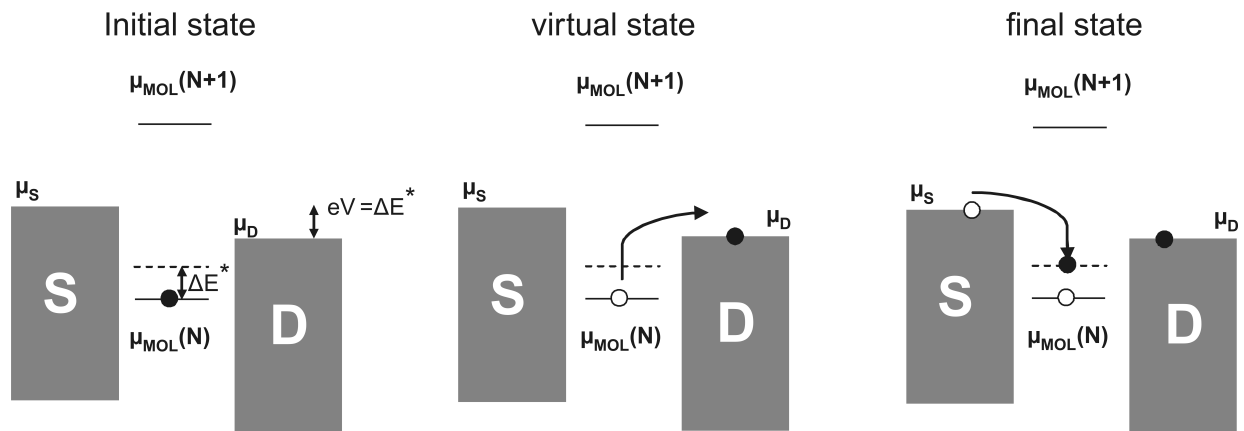


Figure 2.7: Inelastic cotunneling. For $eV = \Delta E^*$, the N -th electron on the dot may jump from the ground state to the drain (virtual state) to be immediately replaced by an electron from the source (final state), which enters the excited state. It will then relax to the ground state.

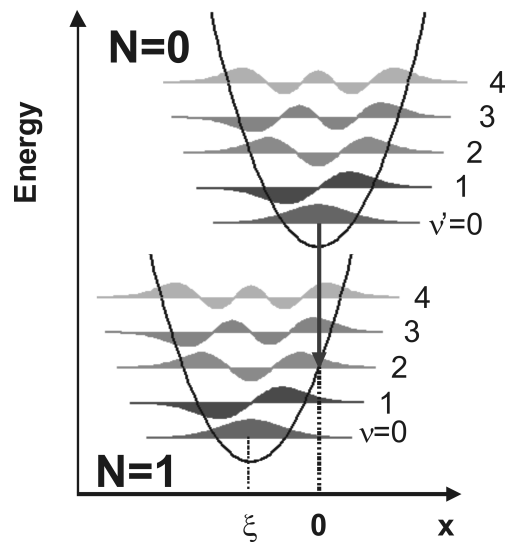


Figure 2.8: Franck-Condon principle. The schematic plot shows vibrational states and their wave functions of the neutral ($N=0$, top) and charged molecule ($N=1$, bottom). Electronic transitions are fast compared to changes in nuclear coordinates (x). Hence, transitions between vibrational states are vertical (blue arrow) and the transition matrix elements are given by the overlap of the corresponding wave function.

we consider one single vibrational mode. When an electron tunnels onto the molecule, the minimum of the nuclear (harmonic) potential is shifted from $x=0$ to $x=\xi$ (new equilibrium position) as illustrated in figure 2.8. This shift is induced by the new electronic configuration in the molecule. The displacement is described by the parameter λ which is the electron phonon coupling. It is the ratio of the displacement and the quantum mechanical uncertainty, x_0 , of the position in the vibrational ground state: $\lambda = \xi/x_0$.

Excitation of a molecular vibration is governed by the Franck-Condon principle (figure 2.8): assuming that initially the (neutral) molecule was in its ground vibrational state, the probability that the molecule ends in a particular vibrational level of the charged molecule is proportional to the square of the overlap integral between the vibrational wave functions of the initial, Ψ_i , and final state, Ψ_f ; the last quantity is commonly referred to as the Franck-Condon factor [34]. As a consequence, the tunnel rates are modified to $\Gamma \rightarrow \Gamma_{elec} |\langle \Psi_f | \Psi_i \rangle|^2$. Note, that when there are no vibrational degrees of freedom the overlap is one and the coupling Γ remains purely electronic. Once the electron hops off, the molecule can be left in a vibrational excited state (the vibrational energy being provided by the outgoing electron). In the sequential tunneling process described before, vibrational states of the charged molecule serve as additional resonance levels; the intensity of the excitation line inside the SET region are then determined by the corresponding Franck-Condon factors. The observation of multiple excitations lines with equal spacing may result from the excitation of an integer number of vibrational quanta as was first presented by Park *et al.* [35] in C_{60} three-terminal molecular junctions. This is only possible for sufficient electron-phonon coupling and in the work of Park, λ was estimated to be around one.

2.2 Three-terminal device fabrication

Three-terminal devices are made using standard electron-beam lithography. In short, four fabrication steps are needed (see figure 2.9a). In the first step, contact pads and alignment markers are defined by evaporation of 3 nm Ti, 35 nm Au and 15 nm AuPd on top of an oxidized Si substrate. Secondly, the gate is defined by evaporating 75 nm Al. Subsequent exposure to O_2 for 15 min. at 50 mTorr allows the formation of a 2-4 nm thick aluminium oxide layer. The third step involves the fabrication of a narrow (100 nm) and thin (12 nm) gold wire –without an adhesion sublayer– on top of the aluminium gate. In a final step, the thin gold wire is connected to the coarse pads by evaporation of 110 nm of AuPd. Figure 2.9b shows a SEM picture of a completed device.

2.3 Electromigration and gap fabrication

For the creation of a nanometer-size gap suitable for contacting single molecules we first narrow the thin gold wire by electromigration to a few-atom constriction. The instability of this gold nanoconstrictions at room temperature –due to mobility and stress in

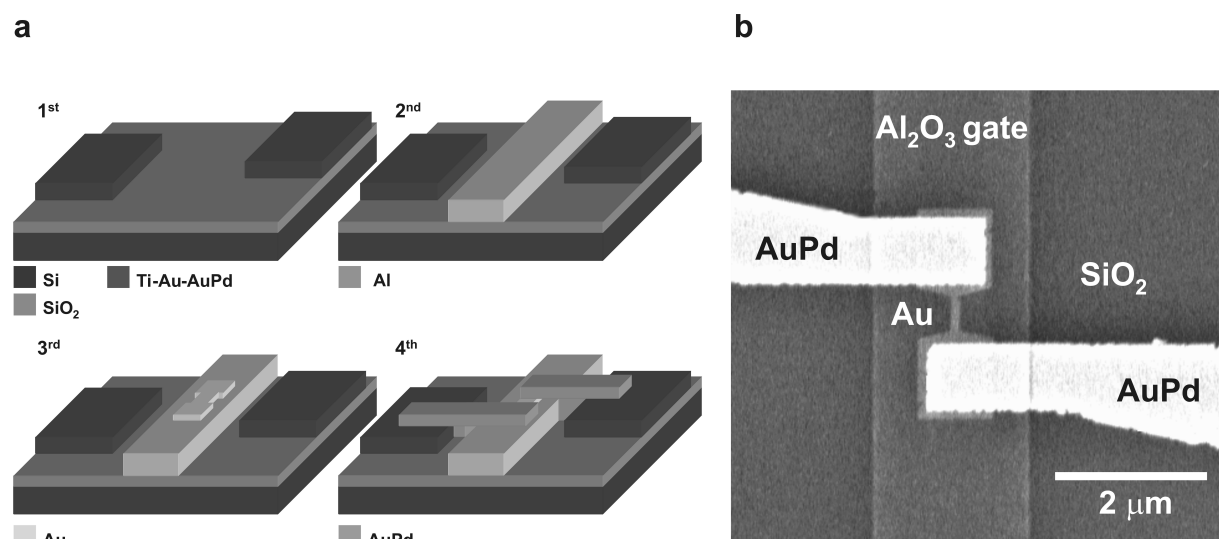


Figure 2.9: Three-terminal device fabrication. **a**, Schematic overview of the four electron beam lithography steps. **b**, SEM image of a completed device prior to breaking.

the material- allows spontaneous breaking of the wire resulting in two separate electrodes [36, 37]: on a time scale of tens of minutes or hours the wires break until they reach conductance values well below 100 mS without any applied bias. The uncontrolled nature of the “self-breaking” process produces nanogaps in a range of sizes.

Electromigration to a few-atom contact is performed using an active breaking scheme, similar to the ones previously reported [38]. In the active breaking process, the voltage is increased from below the electromigration threshold (~ 200 mV) while sampling the current. If the absolute resistance of the wire increases by a value determined during the sweep, typically around 10%, the applied voltage is reduced back to 100 mV, and the sweep is repeated with a new value for the wire resistance. A typical example of this process is shown in figure 2.10. With this method, nanoconstrictions with a resistance in the kOhm range can be achieved with high reproducibility.

2.4 Molecule-junction preparation and characterization

For the deposition of a molecule in the junction we use a home-made liquid cell, placed inside a ⁴He cryostat, containing a 1 mM molecule solution. At room temperature, electromigration is performed in the liquid environment on about 16 junctions which are rinsed with the pure solvent, dried and cleaned in an oxygen plasma beforehand. Nanoconstrictions with a resistance in the kOhm range are first prepared as described above in

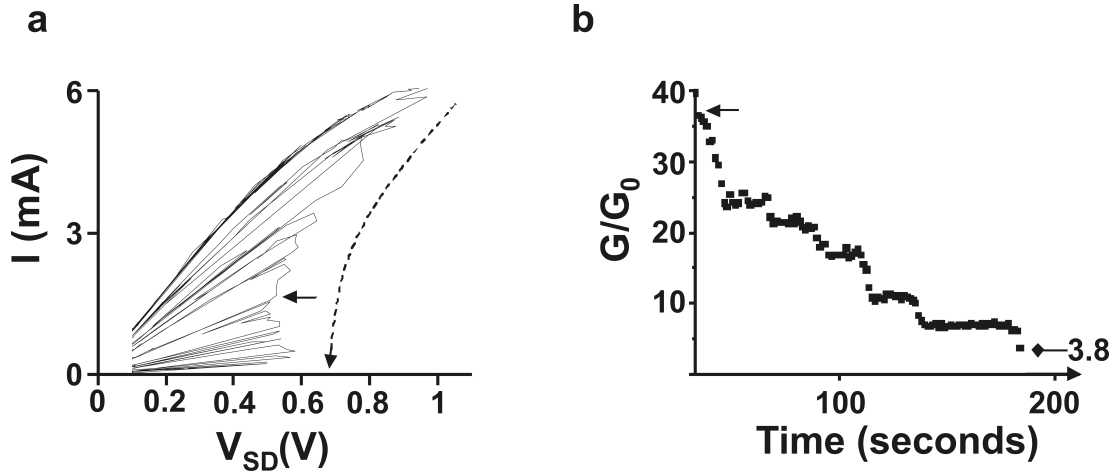


Figure 2.10: Electromigration with an active breaking scheme. **a**, I - V data from a succession of ramps across a junction. The dashed arrow indicates its evolution as the nanoconstriction forms. **b**, Same data truncated at the solid arrow position in **a** with conductance (normalized by $G_0 = 2e^2/h$) versus data point. The final conductance is $3.8G_0 \approx 3.4k\Omega$.

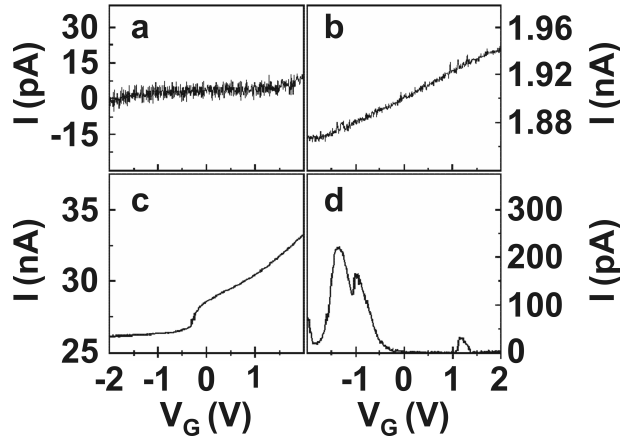


Figure 2.11: Junction characterization. The current as a function of gate voltage in the range of -2 to 2 V, measured at a bias voltage of 50 mV. **a**, **b**, **c**, and **d** illustrate the different behaviours as discussed in the main text.

the solution containing the molecules. The electromigrated junctions are then left in the molecule solution for about 1 hour to allow for molecular self-assembly (if appropriate binding groups are used) and “self-breaking” of the constricted gold wire. Junctions which did not “self-break” within this time are then intentionally broken at conductances higher than G_0 . Last, the sample space is evacuated and the cooling procedure to 1.7 K starts. The molecule deposition technique is similar to the one reported by Riel and co-workers in mechanical break junctions [39]. During electromigration, the junction temperature can reach few hundred Kelvins [40]; performing the self-breaking in solution avoids excessive temperatures on the molecules and allows immediate exposure of the freshly created gap to the molecule solution. We should emphasize that sample contamination could still be an issue since preparation of the molecular junctions is not carried out under ultraclean high-vacuum conditions; layers of water or hydrocarbon molecules may then be present at the contact interface.

Once at base temperature, we characterize our junctions by measuring the current at a source-drain voltage in the range of 10–100 mV as a function of gate voltage from -3 to 3 V; above these voltages, gate leakage usually starts to set in. The gate traces can be categorized in four different ways, and typical examples are shown in figure 2.11:

1. No current within the measurement accuracy (< 10 pA for $V = 50$ mV), indicating that the gap distance is a few nanometers or larger (figure 2.11a).
2. Very weak, linear dependence on gate voltage (figure 2.11b) with less than a few percent change in the current; the origin of which is not understood.
3. Nonlinear, monotonic increase/decrease of the current (figure 2.11c).
4. Traces showing one or more Coulomb peaks (figure 2.11d).

The traces in the two last categories may be a result of transmolecular conduction. Conductance maps are recorded for all these devices. The differential conductance, dI/dV , is either measured directly, with a lock-in technique or obtained from numerical derivation of the I - V characteristics. The stability diagrams of samples that exhibited nonlinear monotonic traces usually show the presence of one partial Coulomb diamond with a weak gate coupling ($\beta < 0.05$) and large addition energies > 200 meV (figure 2.12a). It is difficult to make conclusive statements about these junctions since it is known that electromigration may lead to the formation of small gold clusters [41] which can also exhibit signatures of Coulomb blockade and the Kondo effect [12]. These junctions may then contain a molecule that is well-shielded from the gate by the leads, or a gold grain that is well-coupled to one of the electrodes (figure 2.12a).

Samples that exhibit several Coulomb peaks (more than five), and addition energies smaller than 100 meV are unambiguously treated as junctions containing gold grains in direct contact with the gate dielectric. We find that these junctions show a high gate coupling ($\beta \sim 0.27$); two examples are shown in figure 2.12b,c. Furthermore it is very unlikely for a molecule to show more than five charge states with almost constant addition

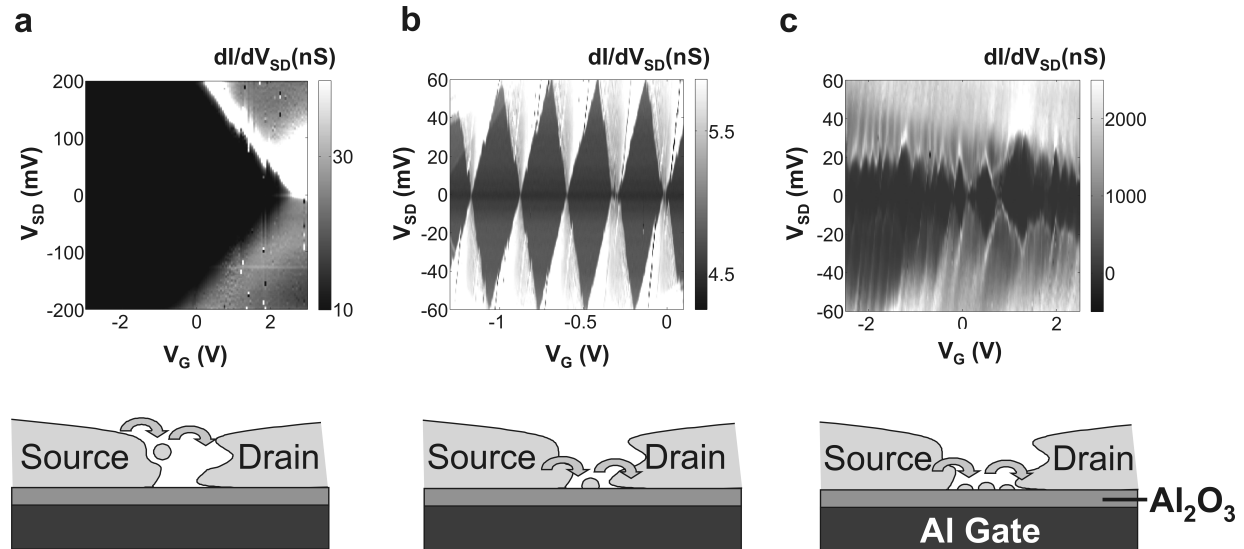


Figure 2.12: Stability diagrams and corresponding illustrations for three different cases. **a**, Well-coupled island (very small gold grain or molecule) to the source electrode, but well shielded from the gate (low gate coupling): $\beta = 0.03$ and $\Gamma = 17.5$ meV. Electron transport through one **b** and several gold grains in series **c** lying on top of the gate dielectric (high gate coupling) : $\beta = 0.27$, $\Gamma = 5.4$ meV in **b** and $\beta > 0.2$, $\Gamma = 8$ meV in **c**. Γ values were estimated from dI/dV versus V traces along the diamond edges as explained in section 2.1.1.

energies as this would mean that for such a small object the electronic spectrum remains unchanged upon the addition of extra charges (figure 2.12b). We note that when using the self-breaking scheme multiple Coulomb diamonds with high gate coupling are not observed; Figure 2.12b,c, are from junctions that were actively broken into high conductances (no self-breaking).

At this point the remaining question is what are the characteristic features for transport through single molecules. Electron addition energies for molecules are expected to be larger than 100 meV. In addition, transport that is due to single molecules has consistently shown a gate coupling that does not exceed 0.15 which can be explained by the fact that molecules are elevated from the gate oxide when connected to gold. Last, we look at generic features present in measurements carried out on the same molecule, such as addition energies, electronic excitation energies and vibrational excitations. This can only be done if a large ensemble of samples has been measured. Furthermore, stability diagrams may contain subtle information about the presence of molecules. For example, one may expect the gate and electronic couplings to be charge dependent because the charge density may differ from orbital to orbital. For gold grains, where the interaction is dominated by the Coulomb repulsion of the electrons (classical dot regime, see figure 2.12b) the smallness of the quantum splitting indicates that the charge distribution of successive orbitals is very similar. Hence we do not expect strong variations of the couplings in that case.

References

- [1] L. P. Kouwenhoven, C. M. Marcus, P. L. Mceuen, S. Tarucha, R. M. Westervelt, and N. S. Wingreen, “Mesoscopic electron transport,” in *Proc. NATO Advanced study institute (Curacao, Netherlands Antilles, 25 June-5 July 1996)*, pp. 105–214, (Kluwer Series E345) ed. L. L. Sohn, L. P. Kouwenhoven and G Schön (Berlin: Springer), 1997.
- [2] K. Likharev, “Single-electron devices and their applications,” *Proceedings of the IEEE*, vol. 87, no. 4, pp. 606–632, 1999.
- [3] L. I. Glazman and M. Pustilnik, *Low-temperature transport through a quantum dot. Nanophysics: Coherence and Transport*. ed H. Bouchiat (Amsterdam: Elsevier), 2005.
- [4] Y. Ono, A. Fujiwara, K. Nishiguchi, H. Inokawa, and Y. Takahashi, “Manipulation and detection of single electrons for future information processing,” *J. Appl. Phys.*, vol. 97, no. 3, p. 031101, 2005.
- [5] D. V. Averin and Y. V. Nazarov, *Single Charge Tunneling: Coulomb Blockade Phenomena in Nanostructures*. ed. H. Grabert and M. H. Devoret (New York: Plenum and NATO Scientific Affairs Division), 1992.
- [6] R. A. Marcus, “On the theory of oxidation-reduction reactions involving electron transfer,” *J. Chem. Phys.*, vol. 24, no. 5, pp. 966–978, 1956.
- [7] H. M. McConnell, “Intramolecular charge transfer in aromatic free radicals,” *J. Chem. Phys.*, vol. 35, no. 2, pp. 508–515, 1961.
- [8] L. Kouwenhoven and L. Glazman, “Revival of the Kondo effect,” *Phys. World.*, pp. 33–38, 2001.
- [9] M. Grobis, I. G. Rau, R. M. Potok, and D. Goldhaber-Gordon, *Kondo effect in mesoscopic quantum dots 2007. Handbook of magnetism and advanced magnetic materials*. ed. H. Kronmuller (New York: Wiley), 2007.
- [10] D. Goldhaber-Gordon, H. Shtrikman, D. Mahalu, D. Abusch-Magder, U. Meirav, and M. A. Kastner, “Kondo effect in a single-electron transistor,” *Nature*, vol. 391, no. 6663, pp. 156–159, 1998.
- [11] D. Goldhaber-Gordon, J. Göres, M. A. Kastner, H. Shtrikman, D. Mahalu, and U. Meirav, “From the Kondo regime to the mixed-valence regime in a single-electron transistor,” *Phys. Rev. Lett.*, vol. 81, no. 23, pp. 5225–5228, 1998.
- [12] A. A. Houck, J. Labaziewicz, E. K. Chan, J. A. Folk, and I. L. Chuang, “Kondo effect in electromigrated gold break junctions,” *Nano Lett.*, vol. 5, no. 9, pp. 1685–1688, 2005.

-
- [13] J. Park, A. N. Pasupathy, J. I. Goldsmith, C. Chang, Y. Yaish, J. R. Petta, M. Rinkoski, J. P. Sethna, H. D. Abruna, P. L. McEuen, and D. C. Ralph, “Coulomb blockade and the Kondo effect in single-atom transistors,” *Nature*, vol. 417, no. 6890, pp. 722–725, 2002.
- [14] L. H. Yu, Z. K. Keane, J. W. Ciszek, L. Cheng, J. M. Tour, T. Baruah, M. R. Pederson, and D. Natelson, “Kondo resonances and anomalous gate dependence in the electrical conductivity of single-molecule transistors,” *Phys. Rev. Lett.*, vol. 95, no. 25, p. 256803, 2005.
- [15] W. Liang, M. P. Shores, M. Bockrath, J. R. Long, and H. Park, “Kondo resonance in a single-molecule transistor,” *Nature*, vol. 417, no. 6890, pp. 725–729, 2002.
- [16] L. H. Yu and D. Natelson, “The Kondo effect in C₆₀ single-molecule transistors,” *Nano Lett.*, vol. 4, no. 1, pp. 79–83, 2004.
- [17] J. Kondo, “Resistance minimum in dilute magnetic alloys,” *Prog. Theor. Phys.*, vol. 32, p. 37, 1964.
- [18] M. Pustilnik and L. Glazman, “Kondo effect in quantum dots,” *J. Phys.: Condens. Matter.*, vol. 16, no. 16, pp. R513–R537, 2004.
- [19] P. W. Anderson, “Localized magnetic states in metals,” *Phys. Rev.*, vol. 124, no. 1, pp. 41–53, 1961.
- [20] L. I. Glazman and M. E. Raikh, “Resonant Kondo transparency of a barrier with quasilocal impurity states,” *JETP. Lett.*, vol. 47, p. 452, 1988.
- [21] T. A. Costi, A. C. Hewson, and V. Zlatic, “Transport coefficients of the Anderson model via the numerical renormalization group,” *J. Phys.: Condens. Matter.*, vol. 6, no. 13, pp. 2519–2558, 1994.
- [22] M. Pustilnik, L. I. Glazman, D. H. Cobden, and L. P. Kouwenhoven, “Magnetic field-induced Kondo effects in Coulomb blockade systems,” *cond-mat.*, no. 0010336, 2000.
- [23] M. R. Buitelaar, A. Bachtold, T. Nussbaumer, M. Iqbal, and C. Schönenberger, “Multiwall carbon nanotubes as quantum dots,” *Phys. Rev. Lett.*, vol. 88, no. 15, p. 156801, 2002.
- [24] J. Nygård, D. H. Cobden, and P. E. Lindelof, “Kondo physics in carbon nanotubes,” *Nature*, vol. 408, no. 6810, pp. 342–346, 2000.
- [25] W. G. van der Wiel, S. D. Franceschi, T. Fujisawa, J. M. Elzerman, S. Tarucha, and L. P. Kouwenhoven, “The Kondo Effect in the Unitary Limit,” *Science*, vol. 289, no. 5487, pp. 2105–2108, 2000.

- [26] P. Jarillo-Herrero, J. Kong, H. S. J. van der Zant, C. Dekker, L. P. Kouwenhoven, and S. De Franceschi, “Orbital Kondo effect in carbon nanotubes,” *Nature*, vol. 434, no. 7032, pp. 484–488, 2005.
- [27] S. Sasaki, S. De Franceschi, J. M. Elzerman, W. G. van der Wiel, M. Eto, S. Tarucha, and L. P. Kouwenhoven, “Kondo effect in an integer-spin quantum dot,” *Nature*, vol. 405, no. 6788, pp. 764–767, 2000.
- [28] M. Pustilnik, Y. Avishai, and K. Kikoin, “Quantum dots with even number of electrons: Kondo effect in a finite magnetic field,” *Phys. Rev. Lett.*, vol. 84, no. 8, pp. 1756–1759, 2000.
- [29] M. Eto and Y. V. Nazarov, “Enhancement of Kondo effect in quantum dots with an even number of electrons,” *Phys. Rev. Lett.*, vol. 85, no. 6, pp. 1306–1309, 2000.
- [30] S. De Franceschi, S. Sasaki, J. M. Elzerman, W. G. van der Wiel, S. Tarucha, and L. P. Kouwenhoven, “Electron cotunneling in a semiconductor quantum dot,” *Phys. Rev. Lett.*, vol. 86, no. 5, pp. 878–881, 2001.
- [31] M. Galperin, M. A. Ratner, and A. Nitzan, “Molecular transport junctions: vibrational effects,” *J. Phys.: Condens. Matter.*, vol. 19, no. 10, p. 103201 (81pp), 2007.
- [32] A. Troisi and M. Ratner, “Molecular signatures in the transport properties of molecular wire junctions: What makes a junction “molecular”?,” *Small*, vol. 2, no. 2, pp. 172–181, 2006.
- [33] J. Gaudioso, L. J. Lauhon, and W. Ho, “Vibrationally mediated negative differential resistance in a single molecule,” *Phys. Rev. Lett.*, vol. 85, no. 9, pp. 1918–1921, 2000.
- [34] G. C. Schatz and M. A. Ratner, *Quantum mechanics in chemistry*. (Mineola, New York: Dover), 2002.
- [35] H. Park, J. Park, A. K. L. Lim, E. H. Anderson, A. P. Alivisatos, and P. L. McEuen, “Nanomechanical oscillations in a single-C₆₀ transistor,” *Nature*, vol. 407, no. 6800, pp. 57–60, 2000.
- [36] K. O’Neill, E. A. Osorio, and H. S. J. van der Zant, “Self-breaking in planar few-atom Au constrictions for nanometer-spaced electrodes,” *Appl. Phys. Lett.*, vol. 90, no. 13, p. 133109, 2007.
- [37] M. Tsutsui, K. Shoji, M. Taniguchi, and T. Kawai, “Formation and self-breaking mechanism of stable atom-sized junctions,” *Nano Lett.*, vol. 8, no. 1, pp. 345–349, 2008.
- [38] D. R. Strachan, D. E. Smith, D. E. Johnston, T.-H. Park, M. J. Therien, D. A. Bonnell, and A. T. Johnson, “Controlled fabrication of nanogaps in ambient environment for molecular electronics,” *Appl. Phys. Lett.*, vol. 86, no. 4, p. 043109, 2005.

-
- [39] E. Lortscher, J. Ciszek, J. Tour, and H. Riel, “Reversible and controllable switching of a single-molecule junction,” *Small*, vol. 2, no. 8-9, pp. 973–977, 2006.
- [40] G. Esen and M. S. Fuhrer, “Temperature control of electromigration to form gold nanogap junctions,” *Appl. Phys. Lett.*, vol. 87, no. 26, p. 263101, 2005.
- [41] J. I. Gonzalez, T. H. Lee, M. D. Barnes, Y. Antoku, and R. M. Dickson, “Quantum mechanical single-gold-nanocluster electroluminescent light source at room temperature,” *Phys. Rev. Lett.*, vol. 93, no. 14, p. 147402, 2004.

Chapter 3

Vibrational modes of a single OPV-5 molecule

E. A. Osorio, K. O'Neill, N. Stuhr-Hansen, O. F. Nielsen, T. Bjørnholm, and H. S. J. van der Zant

We report on charge transport at low temperatures in three-terminal molecular junctions containing a thiol end-capped oligophenylenevinylene molecule (OPV5). Measured addition energies are an order of magnitude smaller than the optically determined HOMO-LUMO gap, corroborating previous reported results. In addition, electron-phonon scattering in our molecular junctions allows determination of the energy of vibrational modes, which are found to be in good agreement with the energies determined from the IR and Raman spectra yielding further evidence that OPV-5 is the molecule trapped in the gap.

3.1 Introduction

Several methods exist to fabricate molecular junctions [1, 2] in which a single molecule bridges the gap between two metallic electrodes. Three-terminal devices [3–13] have the advantage that a voltage on the gate electrode varies the electrostatic potential of the molecule independently of the bias voltage. With the gate electrode, the addition (redox) energies and the excitation spectrum can accurately be determined at low temperature for molecules coupled weakly to the electrodes. The resulting data can serve as a fingerprint of the molecule in the junction. Vibrational modes are commonly observed in these molecular junctions [7–9, 11, 12] but there have been only few reports [6, 11, 12] in which the addition energy of a single molecule trapped in between two leads could be determined. In this letter we discuss transport in three-terminal molecular junctions containing a thiol end-capped oligophenylenevinylene molecule in which five benzene rings are connected through four double bonds (OPV-5, see figure 3.1a). Addition energies measured for eight different devices range between 65 and 220 meV. The present data provide the first independent experimental evidence, confirming that addition energies of OPV-5, placed in metallic nanogaps, are reduced relative to the energy scale set by the optical HOMO-LUMO gap (≈ 2.6 eV) by an order of magnitude as previously reported by Kubatkin et al.[6]. In addition, the unprecedented quality of the data shows clear evidence of vibrational excitations induced by electron-phonon scattering in the molecular junctions, consistent with spectroscopic vibrational excitations of OPV-5 determined by IR and Raman techniques.

3.2 Sample preparation

Electrodes with nanometer separation are fabricated by electromigration. Briefly, we create a thin, 10 nm thick gold wire (width 100 nm, length 500 nm) on top of an Al/Al₂O₃ gate electrode using e-beam lithography (figure 3.1c). The aluminum is oxidized in air forming a 2 to 4 nm thick Al₂O₃ layer, which, at low temperatures, starts to show leakage currents for voltages above typically ± 4 V. AuPd leads, one hundred nm thick, are used to contact the thin gold bridge. To create a nanogap, a technique is employed which is similar to the one developed by Strachan et al.[14]. Electromigration is performed at room temperature by ramping a voltage over the bridge using an active feedback loop: the voltage is ramped until a decrease in the conductance is observed, upon which the applied voltage is returned to zero; the loop is repeated until a target resistance has been reached.

Molecule deposition is done from solution and a derivative of OPV-5 has been chosen that has C₁₂H₂₅ side arms to make it soluble (figure 3.1a). It also contains acetyl protected thiol end-groups to ensure bonding with the gold electrodes [15, 16]. Different approaches have been used to trap molecules in the gap. In one method, the molecules first self-assemble on the gold wires for 4–12 hours from a 1 mM acetone or chloroform solution and then the wire is broken in the vacuum of a ⁴He probe or of a low-temperature probe station. A modification of this method consists of electromigrating the wire in a home-made liquid cell with the molecule solution at room temperature. After breaking the wire,

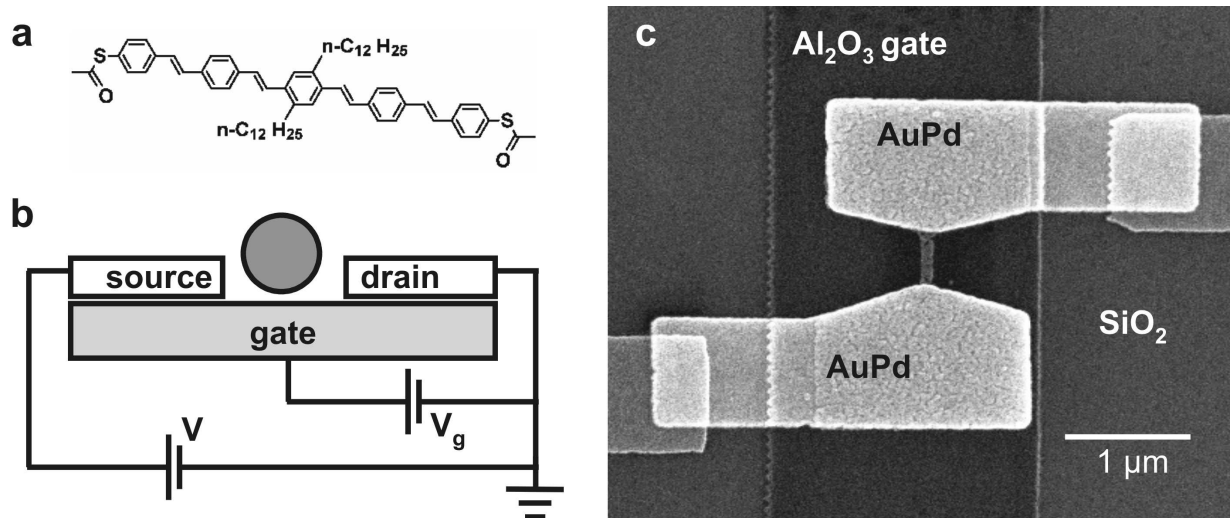


Figure 3.1: **a**, Molecular structure of OPV-5. **b**, Schematic device lay-out. **c**, Fabricated device prior to breaking the small gold wire in the middle by electromigration.

the sample remains in the liquid for three hours; hereafter the sample space is evacuated and the cooling down procedure to 1.7 K is started. In the third method the wires are first broken and then put in the solution with the molecules to allow for self-assembly for 4-12 hours. Subsequently the samples are washed in the pure solvent, dried and mounted in one of the cryostats. We did not find substantial differences in device performance when comparing samples made with these three routes.

3.3 Characterization and statistics

To characterize the gold nanogaps after molecule deposition, we measure at cryogenic temperatures the current at a particular bias voltage (typically in the range of 10-100 mV) as a function of gate voltage in the range from -3 to 3 V. In total 415 junctions with OPV-5 have been measured. The gate traces can be categorized in four different ways and a typical example of each is shown in figure 3.2. The trace in **a** does not show a current within measuring accuracy (< 10 pA for $V = 50$ mV) indicating that the gap distance is a few nanometer or larger. Most junctions (65%) fall in this category. Ninety nine junctions (24 %) show a very weak, linear dependence on gate (figure 3.2b) with less than a few percent change in gate voltage whose origin is not understood. Thirty-one samples exhibit a non-linear, monotonic increase/decrease of the current (figure 3.2c) and 17 junctions show one or more peaks (figure 3.2d).

Eleven percent of all samples fell into the last two categories and may be due to trans-molecular conduction. Stability diagrams, in which the differential conductance (dI/dV) is plotted as a function of bias and gate voltage, have been recorded for all these devices. The derivative is either directly measured with a lock-in technique or obtained from numerical

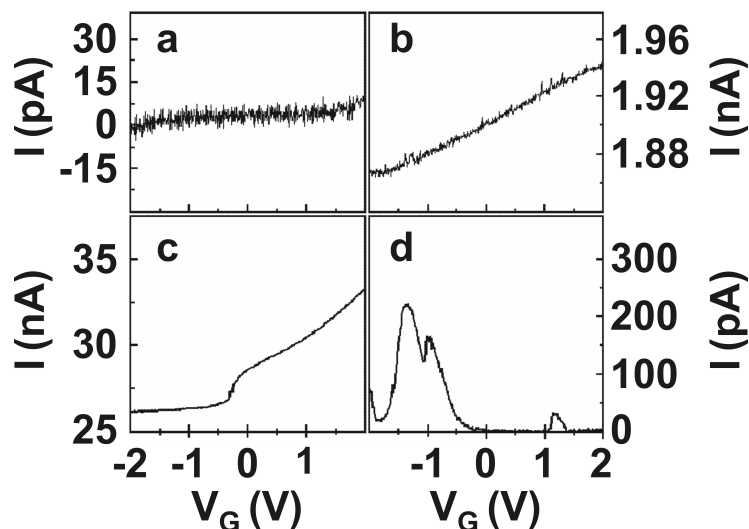


Figure 3.2: Current as a function of gate voltage in the range from -2 to 2 V measured at a bias voltage of 50 mV. **a**, The current is zero within measuring accuracy; the gap is too large for direct tunneling and no molecule is trapped in the gap. **b**, The current shows a weak, linear dependence on the gate voltage; its origin is unknown. **c**, Nonlinear, monotonous change of the current with gate voltage. **d**, The gate trace shows a peak structure with large oscillations of the current.

derivation of the current-voltage characteristics (see figure 3.3 for an example). Measurements of the stability diagram of the samples with the non-linear monotonic traces show that most of them are consistent with the presence of one partial Coulomb diamond with a weak gate coupling (gate coupling parameter < 0.05). It is difficult to make conclusive statements about these junctions. They may contain a molecule that is well shielded from the gate by the leads or a gold grain that is well coupled to one of the electrodes.

The presence of peaks in the gate traces indicates Coulomb blockade with the access of different charge states. In 3 out of 415 cases, five or more charge states have been observed. These junctions most likely contain a gold grain that dominates transport. By calculating the slopes of the diamond-like structures the gate coupling can be determined. For samples with this behavior we consistently find [17] that they exhibit a relatively large gate coupling of 0.23 - 0.27 . In nine cases one to three degeneracy points (crossing points of diamond-like structures; figure 3.3 shows two of such crossing points) are present with a gate coupling of 0.1 - 0.15 or less; transport through these junctions is attributed to transport through single OPV-5 molecules. Finally, in four cases the stability diagram did not exhibit clear signatures of diamond-like structures and we are not able to draw conclusions about the transport mechanism.

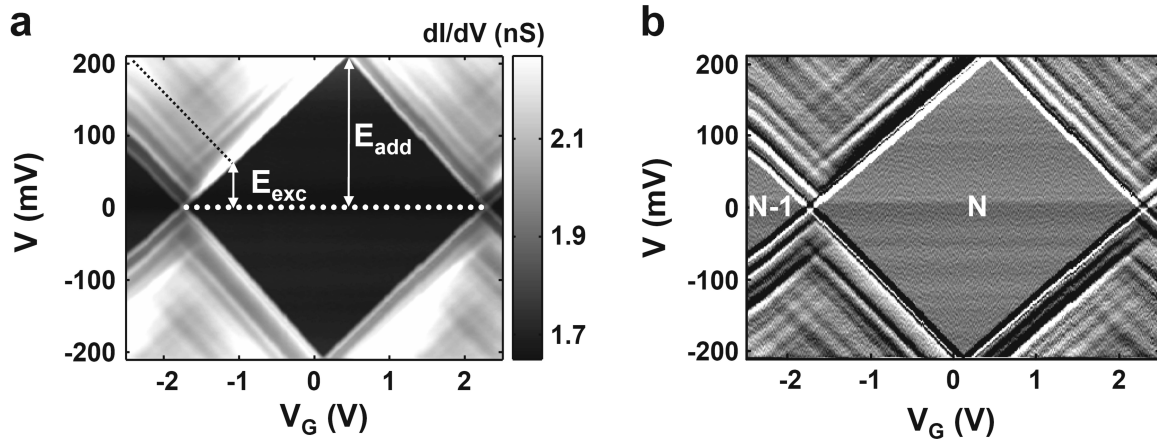


Figure 3.3: Stability diagrams of a three-terminal junction with OPV-5 measured at 1.6 K. Plotted in **a** is dI/dV as measured with a lock-in technique (modulation amplitude 0.4 mV) and in **b** the numerically calculated second derivative, which serves to highlight the fine structure of the excitations. The current levels are the same near both degeneracy points, which is a strong indication that they belong to the same molecule. Three different charge states are probed. The $N+1$ state is not indicated; for low bias voltages it starts at gate voltages larger than 2.2 V. The data yields an addition energy of 210 meV and a gate coupling of 0.05.

3.4 Addition energies and vibrational modes

From the stability diagram the addition energy, $E_{add} = E_{N+1} + E_{N-1} - 2E_N$ where N is the integer number of electrons on the molecule, can be determined. It equals the vertical distance in energy from zero to the highest point of the closed diamond-like structure. For the sample in figure 3.3, the addition energy is 210 meV. In the nine junctions in which the transport is attributed to an OPV-5 molecule, E_{add} could be determined in eight cases; the values are 90 meV, 100 meV, 210 meV (figure 3.3), 120 meV [15], 220 meV, 70 meV, 150 meV, 65 meV and 115 meV. The last two values are from the same junction.

Next to the addition energies, a stability diagram also forms a spectroscopic tool for the determination of excitations that appear as lines running parallel to the Coulomb diamond edges [18]. At such a line, a new state (electronic or vibrational) enters the bias window creating an additional transport channel. The result is a step-wise increase of the current and a corresponding peak in the dI/dV . The energy of an excitation can be determined by reading off the intersection point between the excitation line and the Coulomb diamond edge on the bias axis; the excitations correspond to the charge state of the Coulomb diamond they end up in as illustrated in figure 3.3. From the measurements N cannot be determined, but it is likely to be zero or a small integer value because the deposited molecule was neutral.

The diagram in figure 3.3 clearly shows the presence of sets of excitation lines for all three charge states accessible in the experiment [19]. Further inspection reveals that the

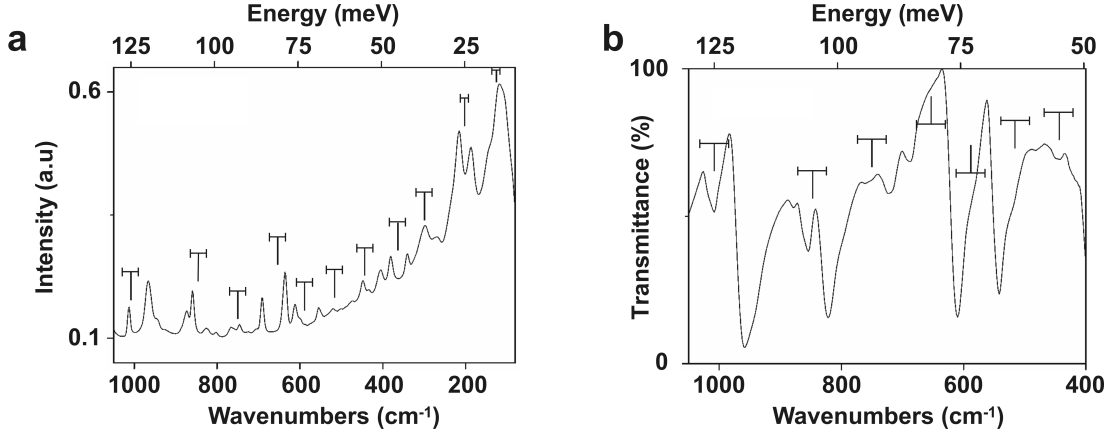


Figure 3.4: Left and right plots are the Raman and IR spectra respectively for the OPV-5 compound of figure 3.1a. Vertical bars indicate the experimental values as determined from the electronic transport data in figure 3.3. The horizontal bars on top show the uncertainty in these values.

point of intersection between the lines and the diamond edge are symmetric with respect to the bias polarity and that their position is almost independent on the charge state. Their appearance may depend on the charge state, i.e., an excitation may not be visible for all three charge states. The energies of the excitations have been determined as described above and are listed in Table I. At most only a very weak variation ($< \text{few meV}$) of the excitation energy with the charge state may be present and this observation makes it unlikely that the excitations are due to electronic states, since these are expected to depend strongly on the charging of the molecule. Moreover, the 17 excitations present in the experimental data are unlikely to reflect precisely 17 available electronic states differing only by 5-10 meV in energy, particularly for a small molecule that can only contain a limited number of electrons/holes. We therefore attribute the excitations to the vibrational modes of the single OPV-5 molecule trapped between the electrodes. We have also observed excitations at the same energies in other samples, although not all of them at the same time. The sample of which the data are shown in figure 3.3 is special in the sense that the molecule-lead coupling is the lowest for this junction; other samples have a larger electronic coupling, leading to a larger life-time broadening.

Raman spectroscopy on polycrystalline samples and infrared spectroscopy on standard KBr-pellets of OPV-5 have been performed. Raman modes with energies higher than 10 meV and IR-modes higher than 50 meV can be detected. In Table I we have listed the energies of vibrational modes that are closest to the experimental values. A very good match is found between the optically determined energies and the ones measured by electron scattering in our three-terminal configuration. It is important to note that not all optical vibrational transitions are visible in our experiment (see figure 3.4). In the absence of general selection rules, it is a priori unclear which modes should be visible. In the Coulomb regime, Frank-Condon coefficients determine the appearance of an excitation connected to vibrational modes [18, 19]. The strength of the electron-phonon coupling and

Table 3.1: Comparison between vibrational modes probed with transport in the sequential tunnel regime (energies extracted from figure 3.3 and figure 3.5) and vibrational modes probed with light in Raman and Infrared (IR; marked by * in the table) spectroscopy. The closest match is given. The read-off error in the experimental values is determined by the broadening of the excitation lines and of the diamond edges.

Transport energy (meV)	Raman/IR energy (meV)
1.4 ± 0.5	
2.3 ± 0.5	
3.5 ± 0.5	
5.0 ± 0.5	
6.7 ± 0.5	
12 ± 0.5	
15.6 ± 1	14.8
25 ± 1	23.4
37 ± 3	37.2
45 ± 3	42.6
55 ± 3	54.2, 53.8*
64 ± 3	65.0, 65.5*
73 ± 3	73.5, 73.6*
81 ± 3	79.5, 78.7*
93 ± 3	92.5, 90.4*
105 ± 3	107.4, 104.4*
125 ± 3	125.6, 126*

the damping of the modes determine these coefficients. These two parameters are affected by the charge state and external factors such as the electric field. This influence is a subject of further study.

At low energy the data show excitations that are not detectable with Raman/IR spectroscopy. Figure 3.5 shows a zoom in on the crossing point from $N-1$ to N . For charge state N , excitations are present at 2.2, 3.5, 5.0 and 6.7 meV (the last one is difficult to see with the contrast of figure 3.5); for charge state $N-1$ they appear at 2.4 and 3.7 meV. Again the values are symmetric with respect to the bias polarity. The energies do not form a harmonic spectrum and they may therefore be attributed to different vibrational modes. Within the error margins, however, the 6.7 meV excitation may be the second harmonic of the one at 3.5 meV, but no definite conclusion can be drawn from the measurements. Quantum chemistry calculations with Amsterdam Density Functional [20] indicate that there are a number of excitations in this energy range that are connected to motion of the whole molecule connected to gold atoms on either side [21].

When comparing our data with the ones from Ref. [6] an interesting difference is the gate coupling parameter. In our case it is 0.12 or smaller whereas their values are consistently larger (about 0.2) despite the fact that both methods use the same fabrication method for the gate electrode and oxide. This difference may be a result of the way

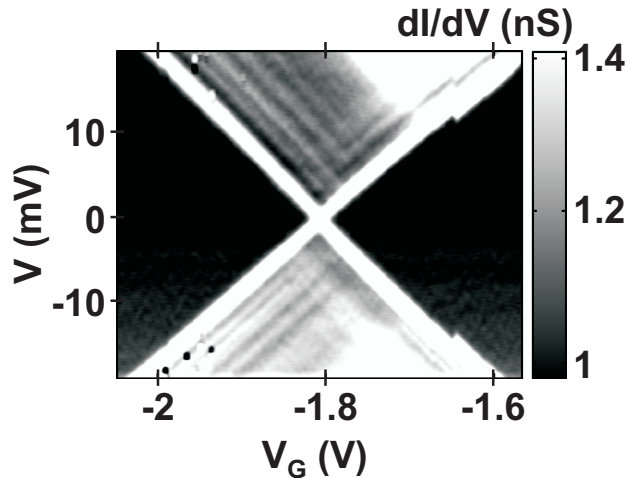


Figure 3.5: Zoom in of the stability diagram shown in figure 3.3 near the degeneracy point separating the $N-1$ from the N state (separate measurement; numerical derivative). Low-lying excitations are visible that are connected to deformations of the whole molecule bonded to gold electrodes on either side.

molecules are introduced in the gap. In the experiment of Ref. [6] gaps are made by e-beam evaporation of metallic leads followed by in-situ deposition of the molecules at low temperatures. Molecules that directly fall on the gold electrodes are most likely immobile due to the large overlap between the π -conjugated p-orbitals and the gold wave functions and hence not probed in the experiment. Molecules that fall on the aluminum oxide are expected to be more mobile and may be the ones that are trapped in the junction. This explains the high gate coupling as molecules are situated directly on the gate oxide. The lower value for junctions made with the electromigration method may indicate that the contacted molecules are elevated from the gate oxide thereby reducing the efficiency of the gate field. In both cases, however, the presence of Coulomb blockade indicates that the electronic coupling to the electrodes is weak but further details about the molecule-lead bonding cannot be established by the experiment.

3.5 Conclusion

In conclusion, we have measured the addition energies and vibrational spectra of molecular junctions containing a single oligophenylenevinylene molecule (OPV-5). Our results are in agreement with previous measurements on the same molecule, which are fabricated with a completely different method. This correspondence between results obtained with two different methods is an important step in establishing the transport characteristics of single molecules, which can be used as input for theoretical modeling and quantum chemistry calculations. For example, it would be important to determine the exact role of image charges in lowering the addition energies as has been put forward in Ref [6, 22].

References

- [1] A. Nitzan and M. A. Ratner, “Electron Transport in Molecular Wire Junctions,” *Science*, vol. 300, no. 5624, pp. 1384–1389, 2003.
- [2] J. R. Heath and M. A. Ratner, “Molecular electronics,” *Phys. Today.*, vol. 56, p. 43, 2003.
- [3] H. Park, J. Park, A. K. L. Lim, E. H. Anderson, A. P. Alivisatos, and P. L. McEuen, “Nanomechanical oscillations in a single-C₆₀ transistor,” *Nature*, vol. 407, no. 6800, pp. 57–60, 2000.
- [4] J. Park, A. N. Pasupathy, J. I. Goldsmith, C. Chang, Y. Yaish, J. R. Petta, M. Rinkoski, J. P. Sethna, H. D. Abruna, P. L. McEuen, and D. C. Ralph, “Coulomb blockade and the Kondo effect in single-atom transistors,” *Nature*, vol. 417, no. 6890, pp. 722–725, 2002.
- [5] W. Liang, M. P. Shores, M. Bockrath, J. R. Long, and H. Park, “Kondo resonance in a single-molecule transistor,” *Nature*, vol. 417, no. 6890, pp. 725–729, 2002.
- [6] S. Kubatkin, A. Danilov, M. Hjort, J. Cornil, J. L. Bredas, N. Stuhr-Hansen, P. Hedegård, and T. Bjørnholm, “Single-electron transistor of a single organic molecule with access to several redox states,” *Nature*, vol. 425, no. 6959, pp. 698–701, 2003.
- [7] L. H. Yu, Z. K. Keane, J. W. Ciszek, L. Cheng, M. P. Stewart, J. M. Tour, and D. Natelson, “Inelastic electron tunneling via molecular vibrations in single-molecule transistors,” *Phys. Rev. Lett.*, vol. 93, no. 26, p. 266802, 2004.
- [8] L. H. Yu and D. Natelson, “The Kondo effect in C₆₀ single-molecule transistors,” *Nano Lett.*, vol. 4, no. 1, pp. 79–83, 2004.
- [9] A. R. Champagne, A. N. Pasupathy, and D. C. Ralph, “Mechanically adjustable and electrically gated single-molecule transistors,” *Nano Lett.*, vol. 5, no. 2, pp. 305–308, 2005.
- [10] Y. V. Kervennic, J. M. Thijssen, D. Vanmaekelbergh, R. Dabirian, L. W. Jenneskens, C. A. van Walree, and H. S. J. van der Zant, “Charge transport in three-terminal molecular junctions incorporating sulfur-end-functionalized tercyclohexylidene spacers,” *Angew. Chem. Int. Ed.*, vol. 45, no. 16, pp. 2540–2542, 2006.
- [11] D. H. Chae, J. F. Berry, S. Jung, F. A. Cotton, C. A. Murillo, and Z. Yao, “Vibrational excitations in single trimetal-molecule transistors,” *Nano Lett.*, vol. 6, no. 2, pp. 165–168, 2006.
- [12] M. Poot, E. Osorio, K. O’Neill, J. M. Thijssen, D. Vanmaekelbergh, C. A. van Walree, L. W. Jenneskens, and H. S. J. van der Zant, “Temperature dependence

- of three-terminal molecular junctions with sulfur end-functionalized teracyclohexylenes,” *Nano Lett.*, vol. 6, no. 5, pp. 1031–1035, 2006.
- [13] H. Park, A. K. L. Lim, A. P. Alivisatos, J. Park, and P. L. McEuen, “Fabrication of metallic electrodes with nanometer separation by electromigration,” *Appl. Phys. Lett.*, vol. 75, no. 2, pp. 301–303, 1999.
- [14] D. R. Strachan, D. E. Smith, D. E. Johnston, T.-H. Park, M. J. Therien, D. A. Bonnell, and A. T. Johnson, “Controlled fabrication of nanogaps in ambient environment for molecular electronics,” *Appl. Phys. Lett.*, vol. 86, no. 4, p. 043109, 2005.
- [15] N. Stuhr-Hansen, J. Christensen, N. Harrit, and T. Bjørnholm, “Novel synthesis of protected thiol end-capped stilbenes and oligo(phenylenevinylene)s (OPVs),” *J. Org. Chem.*, vol. 68, no. 4, pp. 1275–1282, 2003.
- [16] K. Moth-Poulsen, L. Patrone, N. Stuhr-Hansen, J. Christensen, J.-P. Bourgoin, and T. Bjørnholm, “Probing the effects of conjugation path on the electronic transmission through single molecules using scanning tunneling microscopy,” *Nano Lett.*, vol. 5, no. 4, pp. 783–785, 2005.
- [17] H. S. J. van der Zant, E. A. Osorio, M. Poot, and K. O’Neill, “Electromigrated molecular junctions,” *Phys. stat. sol. (b)*, vol. 243, no. 13, pp. 3408–3412, 2006.
- [18] L. P. Kouwenhoven, D. G. Austing, and S. Tarucha, “Few-electron quantum dots,” *Rep. Prog. Phys.*, vol. 64, no. 6, pp. 701–736, 2001.
- [19] “Excitations are not visible in the measurements presented in ref.[1]. It may be that the molecule-lead coupling is important in this respect. In ref. [1] the molecules are coupled to the leads by van der Waals forces; in our case the thiol end groups provide a more robust bonding thereby improving the stability of the junctions.”
- [20] G. te Velde, F. M. Bickelhaupt, E. J. Baerends, C. F. Guerra, S. J. A. van Gisbergen, J. G. Snijders, and T. J. Ziegler, “Chemistry with ADF,” *Comput. Chem.*, vol. 22, no. 9, pp. 931–967, 2001.
- [21] J. S. Seldenthuis, H. S. J. van der Zant, M. A. Ratner, and J. M. Thijssen, “Vibrational excitations in weakly coupled single-molecule junctions: A computational analysis,” *ACS Nano*, vol. 2, no. 7, pp. 1445–1451, 2008.
- [22] P. Hedegård and T. Bjørnholm, “Charge transport through image charged stabilized states in a single molecule single electron transistor device,” *Chem. Phys.*, vol. 319, no. 1-3, pp. 350–359, 2005.

Chapter 4

Electronic excitations of a single OPV-5 molecule

E. A. Osorio, K. O'Neill, M. Wegewijs, N. Stuhr-Hansen, J. Paaske, T. Bjørnholm, and
H. S. J. van der Zant

Low-temperature three-terminal transport measurements through a thiol end-capped π -conjugated molecule have been carried out. Electronic excitations, including zero and finite-bias Kondo-effects have been observed and studied as a function of magnetic field. Using a simplified two-orbital model we have accounted for the spin and the electronic configuration of the first four hole states of the molecule. The charge-dependent couplings to gate, source and drain electrodes suggest a scenario in which charges and spins are localized at the ends of the molecule, close to the electrodes.

4.1 Introduction

Molecules offer a high chemical versatility at the nanometer length scale and a key challenge is to exploit this in single-molecule electronic devices [1–3]. Transistor effects [4–13] and memory operation [14] have been demonstrated, but the properties of single organic molecules coupled to metallic electrodes are still far from understood. In short the energetics of electron transfer to and from a molecule is determined by the intrinsic electronic spectrum of the molecule, and the electronic coupling of the molecule to the environment. The latter is defined both by classical Coulomb charging effects, which strongly depend on the polarizability of the surroundings, as well as by the direct electronic tunnel coupling to the electrodes. For small isolated molecules in the gas phase or in solution the coupling to the environment is well understood. However, the presence of two metal electrodes near the molecule renormalizes its properties and single molecules trapped between metal contacts remain poorly understood and are hence under intense investigation. So far a consistent picture has emerged for two-terminal transport through alkane chains [15] and a family of biphenyl molecules with amine linker groups [16] – both examples of electron transfer by direct tunnelling from source to drain via an off-resonance transport mechanism involving only virtual charge states of the molecule.

In three-terminal devices the gate electrode can bring molecular levels into and out of resonance with the Fermi energy of the electrodes so that different charge states (redox states) [4–13] can be accessed. Contrary to the direct off-resonance tunnelling process mentioned above, Coulomb charging effects play a significant role because the molecules accept one unit charges in the two step process that takes charges from the source to the molecule and subsequently from the molecule to the drain. For a weak electronic molecule-electrode coupling, this sequential tunnelling process is the most dominant transport mechanism. If the molecule is intermediately coupled to the source, and drain-electrodes, higher-order tunnelling processes also become important and one enters a new regime of correlated transport, exhibiting many-body effects such as the Kondo-effect and vibron-assisted inelastic cotunnelling. Metallic nanotube quantum dots displaying Kondo physics have become archetypal examples of such effects [17–19].

4.2 Experiment details

To elucidate the electronic properties of single-molecule junctions we have studied transport in electromigrated junctions [21] containing a thiol end-capped oligophenylenevinylene molecule in which five benzene rings are connected through four double bonds (OPV-5). In addition to a delocalised π -electron system this derivative has n -C₁₂H₂₅ side arms to make it soluble and acetyl protected thiol end-groups to ensure bonding with the gold electrodes [22] (see figure 4.1c). Electromigration was performed on a 10 nm thick gold wire with a width of 100 nm and a length of 500 nm (see also figure 4.1b) using a recently developed self-breaking method [23]. Molecule deposition was done from solution as described in Ref. [24].

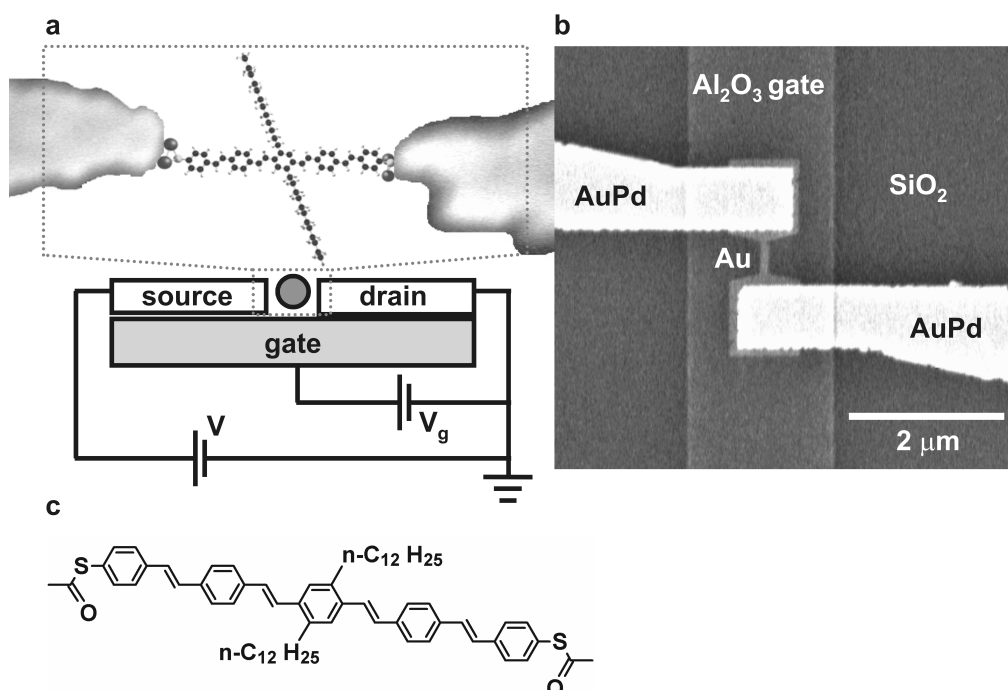


Figure 4.1: **a**, Schematic device lay-out with an OPV-5 molecule bonded to two gold electrodes. **b**, Fabricated device prior to breaking the small gold wire in the middle by electromigration. The junction is fabricated on top of an aluminium gate electrode, which is oxidized in air to form a 2 to 4 nm thick Al_2O_3 layer. At low temperatures, substantial leakage currents are typically observed for voltage above ± 4 V. Bridges are electromigrated at room temperature by ramping a voltage until a decrease in the conductance is observed, upon which the applied voltage is returned to zero [20]; the cycle is repeated until a target resistance is reached. **c**, Molecular structure of OPV-5.

Electromigration is a statistical process and in total 415 junctions with OPV-5 have been made. In chapter 3 we have described the characteristic transport features of seven OPV-5 junctions, which all display an order of magnitude reduction of the addition energy relative to the optical (charge neutral) HOMO-LUMO gap [8], and vibrational mode spectroscopy in accordance with the Raman-vibrational fingerprint of the OPV-5 molecule. We also found that different junctions have different electronic coupling between molecule and electrodes, indicating that we can not control the exact molecule coupling. Here, we discuss in detail the measurements on one particular sample out of these seven. It exhibits intermediate coupling to source and drain electrodes so that Kondo resonances and inelastic cotunneling become visible. These features allow us to assign the spin and orbital filling to four subsequent charge states.

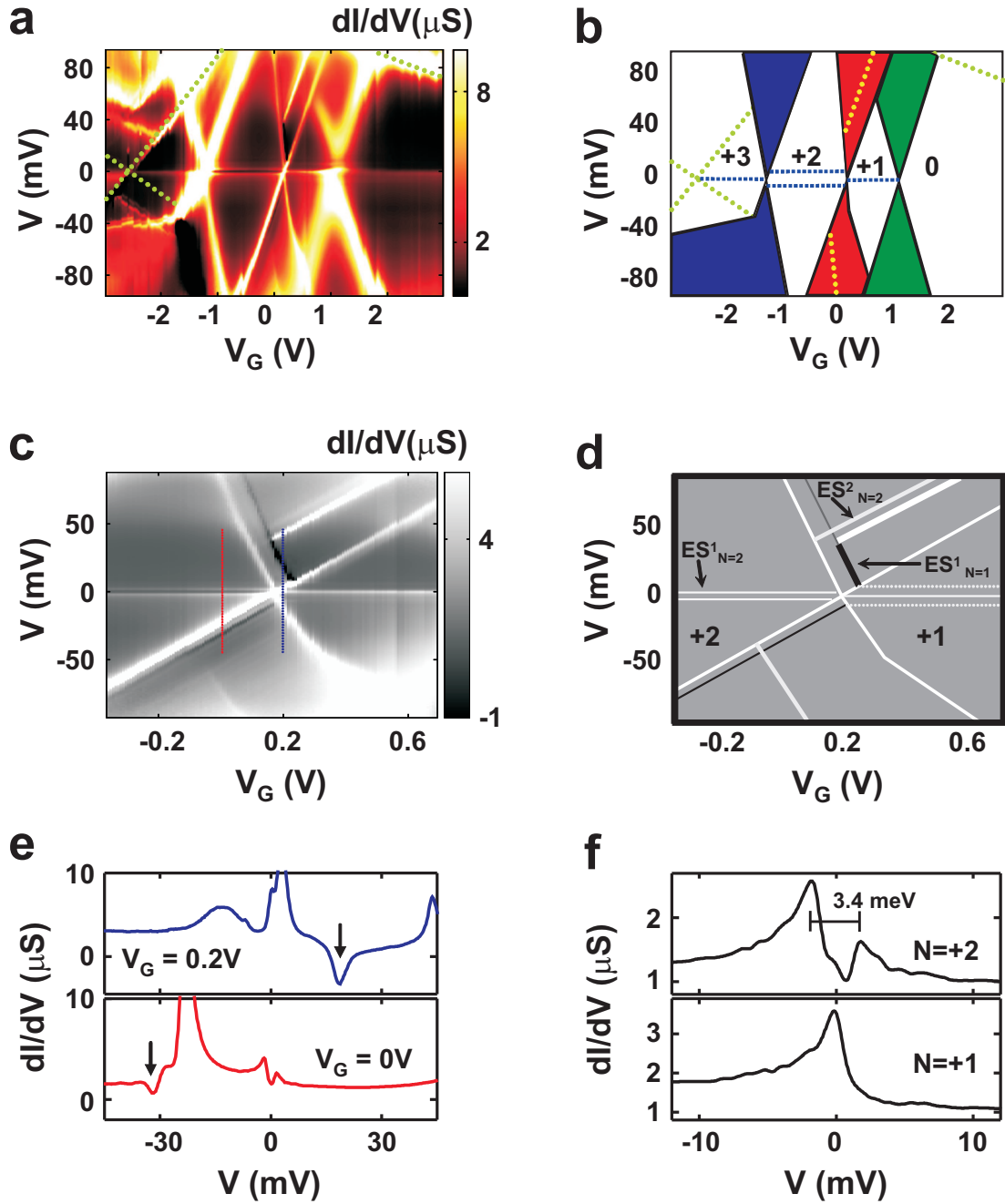


Figure 4.2: **a**, Two dimensional colour plot of the differential conductance, dI/dV , versus V and V_G at $T = 1.7$ K measured with a lock-in technique (modulation amplitude 0.4 mV). Minimum and maximum conductances are $-5 \mu\text{S}$ and $25 \mu\text{S}$ respectively. Dotted green lines indicate the diamond edges of a second molecule connected in parallel. When transferring the probe into another dewar, this structure moved to a less negative gate voltage whereas the other three degeneracy points remained at the same location (see appendix, section A.4). **b**, Schematic drawing of the important information contained in **a** with the charge filling sequence as discussed in the text. **c**, Zoom-in between charge states +2 and +1 exhibiting respectively finite-bias and zero-bias Kondo effects. **d**, Schematic drawing of **c** highlighting its important features. Dashed lines are not visible in the contrast of **c** but do appear when adjusting the contrast. It is important to note that other strong excitations do not appear, indicating that the other electronic levels are far away or are not involved in transport. At low energy we do see lines in the second derivative, which we identify as vibrational modes. **e**, Two dI/dV traces taken at different gate voltages; their position is indicated in **c** by thin vertical lines. The blue curve shows a negative differential resistance (NDR) effect at positive bias voltage. **f**, Measured dI/dV traces taken in the middle of the Coulomb diamonds of the charge states $N = +2$ and $N = +1$.

4.3 Results

The transport-measurements are represented in figure 4.2a as a plot of the differential conductance as a function of applied bias, and gate-voltage. Similar to the well established bias/gate-spectroscopy of semiconducting and nanotube quantum dots, we observe crossing bright lines separating regions of high conductance (single-electron tunnelling (SET) regime) from enclosed diamond-shaped black regions with very low conductance. Horizontal, slightly dimmer, lines within these regions are due to higher-order tunnelling processes.

The overall structure of the bright slanted lines reveals three crossing points, separating four different charge states of the molecule. Numbers in figure 4.2b indicate the charge states (see discussion below). Zero-bias Kondo resonances are visible in the $N = +1$ and $N = +3$ charge states; the $N = +2$ state reveals two finite-bias resonances located symmetrically around zero bias. The sequence: single peak, split peak, single peak is highlighted in figure 4.2b and shows a striking resemblance to data on carbon nanotube quantum dots [17–19]. Another characteristic feature of the Coulomb diamonds is an addition energy of 65 ± 5 meV for $N = +1$ and of 115 ± 5 meV for $N = +2$, similar to earlier reports on the same molecule [8, 24].

The crossing between $N = +1$ and $N = +2$ is of particular interest and figure 4.2c shows a high-resolution dI/dV map of this region. On the right hand-side the zero-bias Kondo peak is clearly visible; on the left-hand-side there are two peaks at a bias voltage of ± 1.7 mV. Examples of differential conductance traces for both cases are plotted in figure 4.2f. The very small peaks superimposed on the main peaks are believed to be vibrational side bands at energies comparable to those measured in other samples. They are also faintly present in the SET regime.

Inspection of the data in figure 4.2c also shows an excitation running parallel to the $N = +2$ diamond edge which exhibits negative differential resistance (NDR as illustrated in figure 4.2e, upper trace). In figure 4.2c the energy of this excitation can be read off as the distance from the zero-bias axis to the crossing point with the diamond edge; it equals 6 ± 1 meV. At the negative side this excitation is also present at the same energy as a zero-bias conductance plateau. For the $N = +2$ state, excitations are present at 30 ± 1 meV and $\pm 37 \pm 1$ meV.

We have studied the low-bias features of figure 4.2c as a function of temperature and magnetic field. The temperature dependence of the maximum conductance of the peaks at $N = +1, +3$ is consistent with the regular $S = 1/2$ Kondo effect as shown in figure 4.3b by the red lines which are fits to the expected behaviour:

$$G_K = G_c + G_a [1 + (2^{1/s} - 1) T^2/T_K^2]^{-s} \quad (4.1)$$

where $s = 0.22$ and where G_c, G_a are fitting parameters. The fits yield Kondo temperatures of 37 and 30 K for $N = +1$ and $+3$ respectively, roughly consistent with the full width at half maximum of the zero-bias peaks which are 32 K for $N = +1$ and 24 K for $N = +3$. For $N = +2$, the zero-bias conductance first increases as temperature is raised. At 35 K

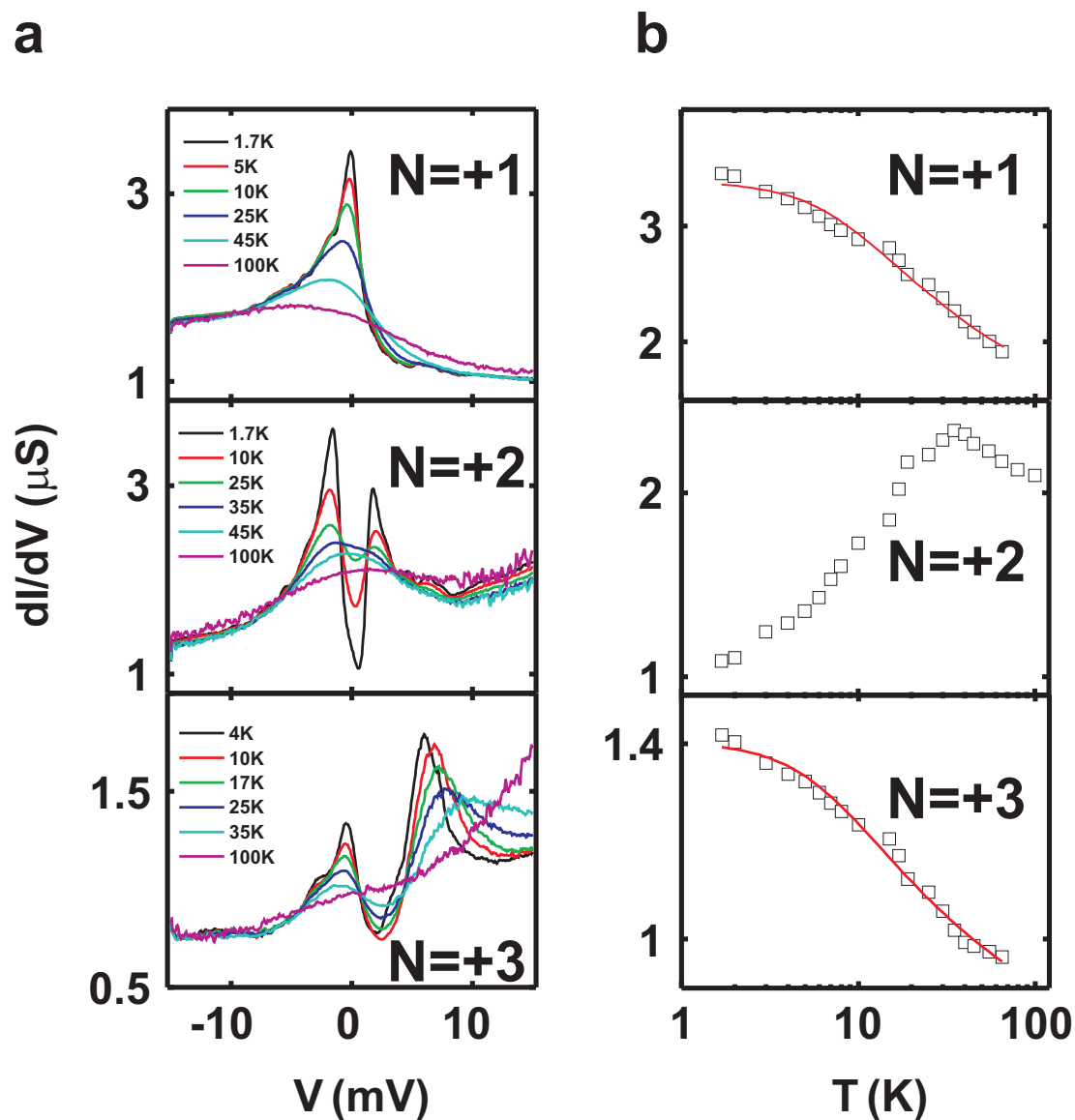


Figure 4.3: **a** dI/dV versus V at fixed gate voltage for various temperatures with $V_G=0.56$ V, -0.72 V and -2 V for charge states $+1$, $+2$ and $+3$ respectively. For the charge state $+3$ the second peak around 7 mV corresponds to the diamond edge. **b**, Zero-bias conductance as a function of temperature. Lines are fits to Eq. 4.1 with $s=0.22$: the fitting parameters are $T_K = 37$ K, $G_c = 1.0$ S, $G_a = 2.3$ μS and $T_K = 30$ K, $G_c = 0.7$ μS , $G_a = 0.7$ μS for $N=+1$ and $N=+3$ respectively. For $N=+2$, the zero-bias conductance first increases with increasing temperature followed by a decrease for $T > 35$ K (~ 3 meV).

it reaches a maximum and for higher temperatures the conductance decreases again. The value of 35 K corresponds to an energy of 3 meV, which is close to the distance between the split low-bias peaks in this charge state (see figure 4.2f).

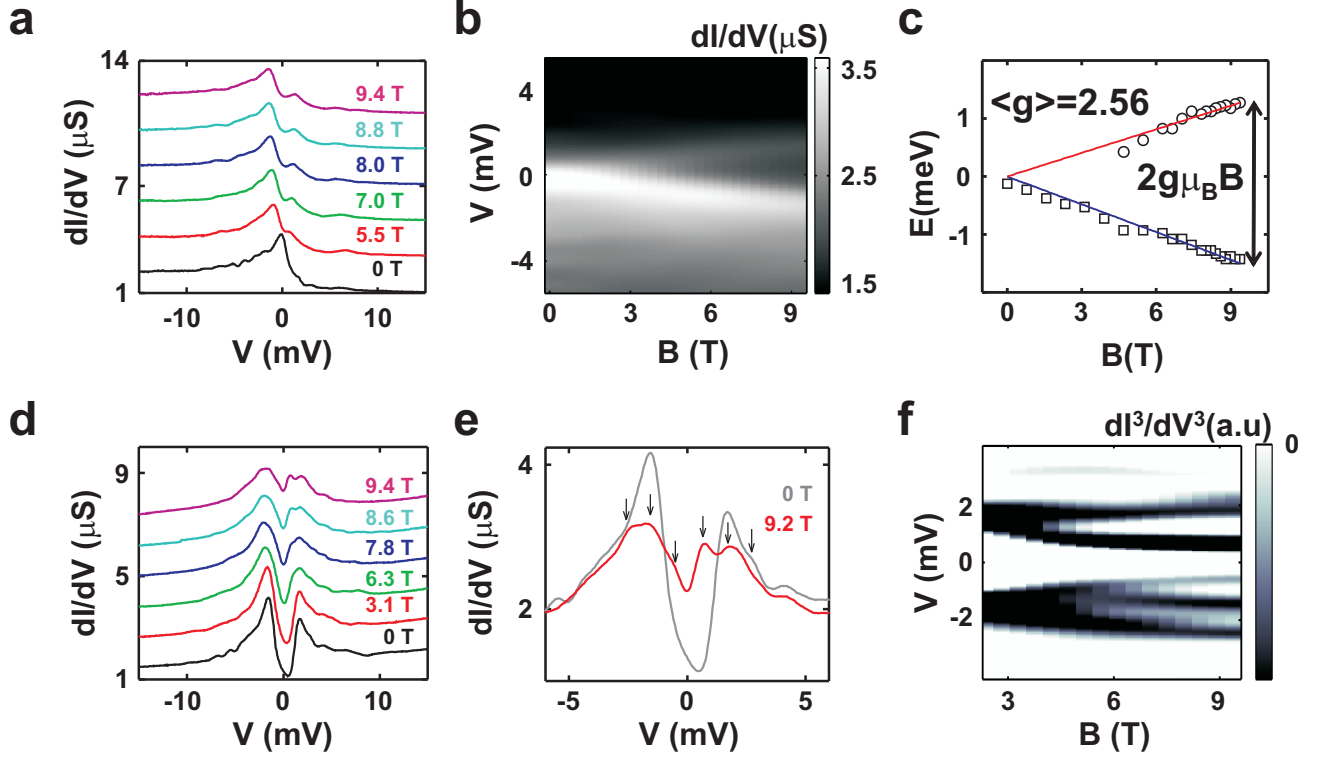


Figure 4.4: **a**, dI/dV trace at $V_G = 0.56$ V (charge state $N = +1$) recorded for different magnetic fields as measured with a lock-in technique (modulation amplitude 0.04 mV). Traces are offset by $2 \mu\text{S}$ for clarity. **b**, Grey-scale plot of dI/dV versus V and B at $V_G = +0.56$ V. **c**, Peak positions as a function of magnetic field taken from the data in **b** indicating a g value of 2.56. **d**, Same as **a**, but at $V_G = -0.72$ V (charge state $N = +2$). Subsequent traces are offset by $1.2 \mu\text{S}$. **e**, dI/dV traces at $V_G = -0.72$ V measured in a magnetic field of $B = 0$ T (grey) and $B = 9.2$ T (red). Arrows indicate the predicted positions of peaks at $B = 9.2$ T assuming the triplet splits according to $g\mu_B m_S B$ with $g = 2$ and $m_S = -1, 0, 1$. **f**, Grey-scale plot of dI^3/dV^3 versus V obtained by numerical differentiation of the measured dI/dV at $V_G = -0.72$ V. The third derivative underlines the presence of three (two) peaks for negative (positive) bias voltage (peaks in the first derivative correspond to dips in the third derivative).

Figure 4.4, panels a and d, show the conductance traces at gate voltages 0.56 V ($N = +1$) and -0.72 V ($N = +2$) respectively for various magnetic fields. For $N = +1$ the magnetic field splits the peak in two and the magnetic field dependent data are again consistent with $S = 1/2$ Kondo physics. Measurements on the finite-bias peaks inside the $N = +2$ diamond show that a magnetic field splits each peak into two clear peaks. At negative bias, the third derivative (figure 4.4f) shows the presence of three peaks. This evolution in a magnetic field, B , is consistent with inelastic cotunnelling from a singlet ground state to an excited triplet (cf. appendix, section A.3). The splitting in each peak

should be $g\mu_B m_S B$ with $m_S = \pm 1$. With a g -factor of 2 the splitting in figure 4.4e,f yields an m_S -value of 0.87 at negative bias and 1.0 at positive bias, consistent with the identification of the triplet state as the excited state.

From the magnetic field measurements, we conclude that the Coulomb diamond with the split peaks in zero-magnetic field has a ground state with an even occupancy. We assign $N = +2$ to this state and starting from this, the electronic and spin spectrum can be identified using a model that involves two weakly interacting states with an antiferromagnetic exchange energy J . From standard Coulomb blockade theory we employ the following effective Hamiltonian for the molecule (cf. Refs [25, 26]):

$$H_{mol} = E_C \left(\sum_{\substack{i=A,B \\ \sigma=\uparrow,\downarrow}} n_{i\sigma} - N_0 - N_G \right)^2 + \delta n_B + dU \sum_{\substack{i=A,B \\ \sigma'=\uparrow,\sigma=\downarrow}} n_{i,\sigma'} n_{i,\sigma} + J \vec{S}_A \cdot \vec{S}_B \quad (4.2)$$

where $\{n_{A\uparrow}, n_{A\downarrow}, n_{B\uparrow}, n_{B\downarrow}\}$ denote the occupation operators for two distinct orbitals A and B with corresponding spin-1/2 operators \vec{S}_i . The parameters represent an orbital splitting δ , an electrostatic charging energy $E_C = e^2/2C$ defined in terms of a total capacitance C , a gate-induced charge $N_G = C_G V_G/e$, an additional *intra*-orbital Coulomb repulsion dU and an *inter*-orbital antiferromagnetic exchange-coupling $J > 0$.

From the Hamiltonian in Eq. 4.2 the addition and excitation energies can be calculated assuming that charging the molecule is merely a matter of filling up two distinct “frozen” orbitals. Figure 4.5a summarizes the results for the $N = +1$ and $N = +2$ charge states. We now compare the predictions of this model with the data and check for consistency. For $N = +2$ the data reveal a singlet ground state together with inelastic cotunnelling lines at ± 1.7 meV ($ES_{N=+2}^1$), which are connected to a triplet state. Thus, the exchange coupling, J , is anti-ferromagnetic and equals 1.7 meV. The data at $N = +1$ show a strong excitation at 6 ± 1 meV, which we identify as the level mismatch δ ($ES_{N=+1}^1$). For the $N = +2$ state another excitation ($ES_{N=+2}^2$) is visible at ± 37 meV. At the positive side there is also an additional excitation at 30 meV connected to a transition between the second $N = +2$ excited state and the first $N = +1$ excited state ($ES_{N=+2}^2 - ES_{N=+1}^1$). The difference between these excitations at 30 and 37 meV should be the level mismatch δ , which is indeed the case. The value of 37 meV for the second excitation for the doubly-charged state indicates that $dU = 42 \pm 2$ meV. The experimental values for the addition-energies are $E_{add,N=+1} = 65 \pm 5$ meV and $E_{add,N=+2} = 115 \pm 5$ meV. From the first number we deduce a charging energy $E_C = 30 \pm 3$ meV, whereas the reading for $E_{add,N=+2}$ implies that $E_C = 38 \pm 4$ meV. The fact that these two numbers are close serves as a positive consistency check of our two-orbital model.

We emphasize that the analysis presented above accounts for all the electronic and magnetic excitations of the OPV-5 junction throughout four consecutive charge states. The remaining question is how the two weakly interacting and spatially separated states A and B relate to the molecule in the junction. Here we note that the presence of two

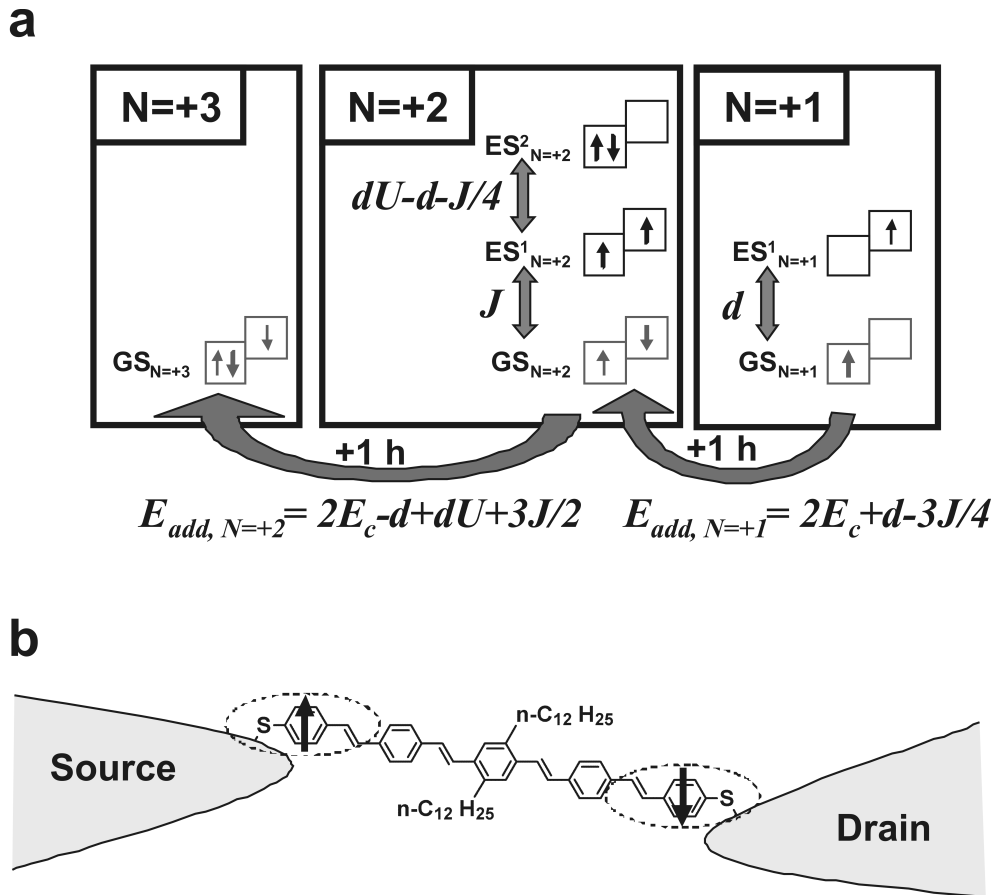


Figure 4.5: **a**, Two orbitals, A and B , (depicted by the two boxes) are separated in energy by δ . $GS_{N=i}$ and $ES_{N=i}$ denote ground and excited states respectively for charge state $i = +1, +2$ and $+3$ (excited states for $N = +3$ are not shown). J is the inter-orbital, anti-ferromagnetic exchange energy, $E_C = e^2/2C$ is the electrostatic charging energy and dU is the intra-orbital Coulomb repulsion. At the bottom, $E_{add, N=i}$ denote the addition energies for charge state $i = +1, +2$. **b**, Schematic impression of the two-site orbital model for an OPV-5 molecule connected to gold electrodes on either side. The black dashed ovals represent the orbitals A and B .

nearly degenerate antiferromagnetically coupled states corroborates a picture invoked in previous papers involving image charges in the metal electrodes in which charges and spins localize at either end of the molecule as schematically illustrated in figure 4.5b [8, 27]. In the remainder of this letter we highlight another feature of these states which hints at their molecular origin.

The line width defining the diamond-like structures in figure 4.2a is proportional to the electronic coupling, Γ , and as this figure shows, appears to be dependent on the charge state: The diamond edges are sharper for the $N = +2$ state compared to $N = +1$ and $N = +3$. For the region where electron tunnelling involves $0 \rightarrow +1 \rightarrow 0$ transitions, a Lorentzian fit through the dI/dV vs. V line shape yields $\Gamma \sim 35$ meV; for the $+1 \rightarrow +2 \rightarrow +1$ and $+2 \rightarrow +3 \rightarrow +2$ transitions, Γ is 6 and 22 meV respectively. A related observation is that the gate coupling for the three different charge states is not the same. For charge state +1, +2 and +3 the gate coupling equals 0.06, 0.1, and 0.07 respectively. Thus, the $N = +2$ charge distribution on the molecule is more susceptible to the gate field. Apparently, the wave functions are located more to the middle of the junction in agreement with the lower electronic coupling for this charge state.

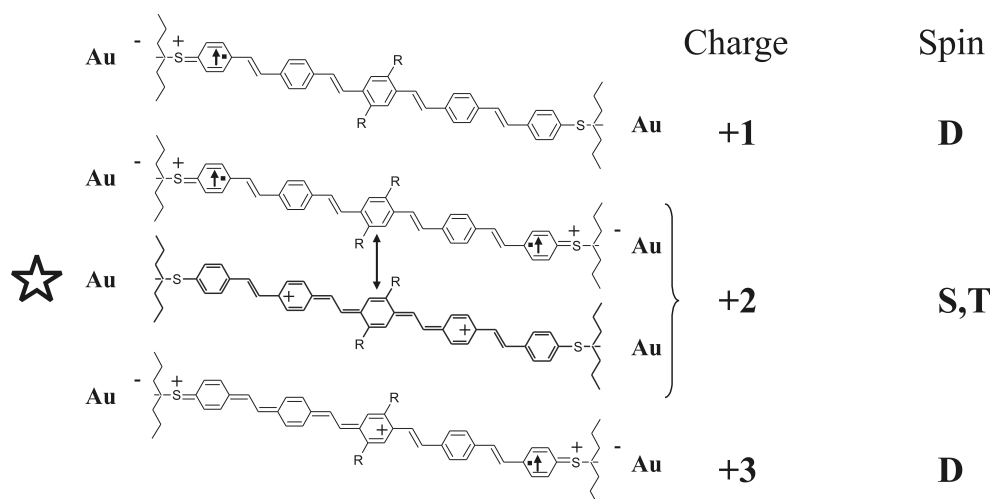


Figure 4.6: Plausible valence bond representations of the first three positively charged states. The likely spin multiplicity is indicated in the right column. The classical valence bond description of the doubly charged OPV-5 molecule involves a spinless bi-polaron structure (marked by a star) in which a quinone structural motif separates the two positive charges defining a distance between the positive charges which reflects the equilibrium between the attractive structural relaxation of the molecular backbone (the quinoid structure) and the repulsion between the positive charges. The double arrow connects “resonance” structures in organic chemical terminology.

By considering the plausible valence bond structures of OPV-5, we have been able to link the observed change with charge state in couplings to electrodes and gate to its molecular structure. For the first three positively charged states, these bond structures are depicted in figure 4.6. The singly charged state (top) is a spin doublet with a strongly localized charge at one terminal. The spin remains localized to the same terminal benzene

ring to preserve aromaticity (undisturbed benzene rings which are particularly stable) in the remaining four rings. Charge transport could occur by charges tunnelling directly to and from this terminal state that hence defines the values of Γ and the gate coupling.

The likely representation of the doubly charged state is shown in the middle of the figure where the ground state is represented by two states similar to the singly charged molecule, but with the possibility to mix the quinone state (structure marked by a star in figure 4.6) into the ground state (in organic chemistry terms one would say that the state is represented by two valence bond structures in “resonance” with most weight to the black one). The admixing of the quinone state into the ground state results in a slight movement of the charges away from the electrodes resulting in a smaller Γ and a stronger gate coupling. The triply charged state can be described as a sum of the singly and doubly charged systems and transport could again occur via a state that is very similar to the singly charged molecule (now at the left electrode), giving rise to values of Γ and the gate coupling that are very similar to the singly charged state, as observed in the experiment.

4.4 Conclusion

We conclude with a few remarks on the generality and consistency of the results described in this letter. We have performed preliminary quantum chemistry calculations to account for the image charge effects and in particular the electrostatic energy a charge carrier on the molecule gains when approaching the metal electrodes. We find that this energy gain crucially depends on the exact contact geometry which involves the Au-S bond angle and the distance to the image charge. In the experiment, we therefore expect a spread in the measured addition energies and charging energies in agreement with the observations [8, 27]. On the other hand, the exchange energy in this scenario is expected to be not very dependent on the exact contact geometry, since the distance between the two spins remains approximately the same. Measurements on the only other OPV-5 junction that displays higher-order processes are consistent with these observations. It also shows inelastic cotunnelling peaks at an energy of ± 1.5 meV, close to the value reported here. This sample, however, exhibits higher addition energies and as a consequence only one degeneracy point could be resolved so that a further comparison with the model involving multiple charge states could not be performed. Further experimental and theoretical work would be helpful for a quantitative understanding of the charge-spin distribution in molecular junctions.

Appendix

A.1 Addition energies and excitations

From Eq. 4.2 we deduce the following energies for different N :

$$\begin{aligned}
E(0) &= E_C(N_0 + N_G)^2 \\
E(1) &= E_C(1 - N_0 - N_G)^2 \\
E'(1) &= E_C(1 - N_0 - N_G)^2 + \delta \\
E(2) &= E_C(2 - N_0 - N_G)^2 + \delta - 3J/4 \\
E'(2) &= E_C(2 - N_0 - N_G)^2 + \delta + J/4 \\
E''(2) &= E_C(2 - N_0 - N_G)^2 + dU \\
E'''(2) &= E_C(2 - N_0 - N_G)^2 + 2\delta + dU \\
E(3) &= E_C(3 - N_0 - N_G)^2 + \delta + dU \\
E'(3) &= E_C(3 - N_0 - N_G)^2 + 2\delta + dU \\
E(4) &= E_C(4 - N_0 - N_G)^2 + 2\delta + 2dU
\end{aligned}$$

with primed energies giving the excited configurations. Notice that for $N=+1, +3$ all states are spin-doublets, whereas the lowest $N=+2$ state is a singlet and the first excited state is a triplet. The highest excited states for $N=+2$ are *intra*-orbital singlets. The electro-chemical potentials are found as $\mu(N) = E(N) - E(N - 1)$:

$$\begin{aligned}
\mu(1) &= E_C(1 - 2N_0 - 2N_G) \\
\mu(2) &= E_C(3 - 2N_0 - 2N_G) + \delta - 3J/4 \\
\mu(3) &= E_C(5 - 2N_0 - 2N_G) + dU + 3J/4 \\
\mu(4) &= E_C(7 - 2N_0 - 2N_G) + \delta + dU
\end{aligned}$$

and the observable addition energies as $E_{add,N=+i} = \mu(i + 1) - \mu(i)$:

$$\begin{aligned}
E_{add,N=+1} &= 2E_C + \delta - 3J/4 \\
E_{add,N=+2} &= 2E_C - \delta + dU + 3J/2 \\
E_{add,N=+3} &= 2E_C + \delta - 3J/4.
\end{aligned}$$

Finally, the excitation energies for the different charge states are given by:

$$\begin{aligned}
ES_{N=+1}^1 &= \delta \\
ES_{N=+2}^1 &= J \\
ES_{N=+2}^2 &= dU - \delta + 3J/4 \\
ES_{N=+2}^3 &= dU + \delta + 3J/4 \\
ES_{N=+3}^1 &= \delta.
\end{aligned}$$

A.2 Negative Differential Resistance effect.

Maarten Wegewijs.

The excitation exhibiting a sharp negative differential conductance is of special interest as it is drastically modified when another competing excitation becomes accessible at higher bias voltages at which point the NDR vanishes. This is a fingerprint of strong wave function-dependent tunnel processes (unrelated to spin or junction asymmetry), which

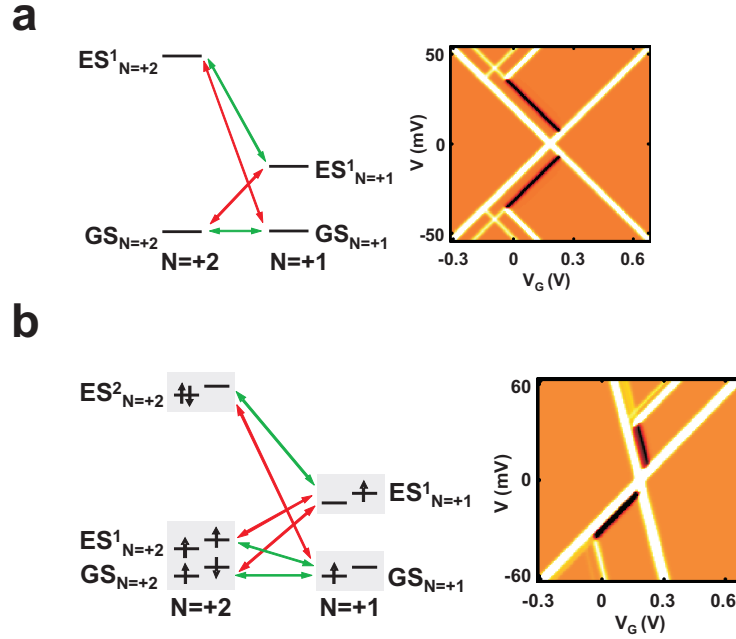


Figure A.1: **a**, Schematic drawing of tunnelling transitions in a four-state model with symmetric gate coupling ($\alpha_+ = \alpha_-$ with $\alpha_+ = C_G/(C_G + C_D)$ and $\alpha_- = -C_G/C_S$) and **b**, in the full model from the main text (parameters are taken from the orbital filling model in section A.1 and the gate couplings from the experimental calculated values), each with the corresponding dI/dV map. In **a** it is essential that all transitions indicated in red are slower by a factor 100 relative to the green transitions. The green E-E' transition is taken somewhat faster (1.5 times) than the G-G' one: this ensures that the NDR turns into a positive dI/dV at negative V_G for bias voltages >30 mV. In **b** the same relations hold between rates as in **a** for corresponding groups of states in the sketch. In addition, we incorporated a moderate reduction factor of 0.65 for transitions where an empty or doubly occupied orbital on the side of the electrode blocks the incoming hole / electron from that electrode. This causes the 30 meV excitation to appear only at $V>0$.

are a marked feature of molecular three-terminal devices as demonstrated in this work. It is important to note that the NDR feature preserves its form for temperatures up to 11 K (stability diagrams for $T > 11$ K were not recorded), where temperature effects become important for the broadening of the resonances. At this temperature, a sequential tunnelling picture starts to become applicable ($\Gamma \sim k_B T$). Furthermore, the picture of competing transport channels presented below is very robust and does not depend critically on the strength of the tunnel coupling Γ relative to T . The central point of this section is that the occurrence of NDR and the observation of transitions between two excited states (at 30 meV) indicate that relaxation processes are slower than any of the transport induced transitions.

The qualitative features of the data are readily reproduced in a simple sequential tunnelling model, presented in figure A.1a, which we discuss first. The experimental transport fingerprint appears in such a model only when *i*) a minimum of four states is accounted for, a ground- (G,G') and excited (E,E') state in each of the two adjacent molecular charge

states, and *ii*) the rate constants for transitions between excited and ground (G-E', G'-E) are much smaller than those for ground-ground (G-G') and excited-excited (E-E') transitions as sketched in figure A.1a.

The NDR effect is most easily understood in a time-averaged picture: the fast G-G' and E-E' transitions or “channels” are responsible for transport and there are rare transitions in which the system switches from one channel to the other. If initially only the G-G' channel is open, NDR occurs if the slow transition G→E' is switched on with increasing bias, while the E→E' transition is not yet energetically possible. This occurs for gate voltages close to the degeneracy point in figure A.1a. The system spends a significant fraction of the transport cycle in the “closed channel” leading to a significant reduction of the current. In contrast, if the E→E' channel is already open with the E→G' transition switched on, the current only changes slightly; the dark line changes into a white line as illustrated in the left upper and lower corners of the stability diagrams in figure A.1a.

This simplified picture applies to the more complicated electronic spectrum inferred from the experimental data, if groups of relatively closely-spaced states take over the role of G, G', E, E' states. In figure A.1b we incorporated all the electronic excitation energies as determined in the previous section and we fixed the relative magnitudes of the rate-constants analogous to the simple four state model. The gate coupling factors were taken from the experimental data. The model then reproduces nearly all the qualitative features of the data. When comparing, one should note that in the experiment a superposed background conductance (see section A.3) causes the NDR effect for $V < 0$ to appear as a narrow dI/dV plateau instead of a dip.

The microscopic origin of the strong state dependence of the tunnel rates cannot be inferred from the data. However, all transitions are spin-allowed ($\Delta S = 1/2$) and the experimental data show no evidence of a very strong asymmetry between the tunnel rates associated with the left and right electrodes. *The NDR effect therefore indicates that the spatial structure of the many-particle ground and excited states are very dissimilar and that this difference is preserved upon charging the molecule.* Vibrationally assisted tunnelling may modify the sequential tunnelling rates and may contribute to the asymmetry pointed out here. A quantitative description of this lies beyond the scope and accuracy of the present work. Given the simplicity of the model, it is surprising that the particular choice of values for the rates in figure A.1b leads to a good agreement with the experimental features, indicating that the model captures the basic underlying physics of the transport mechanism.

A.3 Effective model for $N = 2$: Finite-bias singlet-triplet Kondo effect.

Jens Paaske.

As demonstrated in chapter 4, the observed sequential tunnelling spectroscopy, including the NDR, is consistent with a simple model with two low-energy orbitals, A and

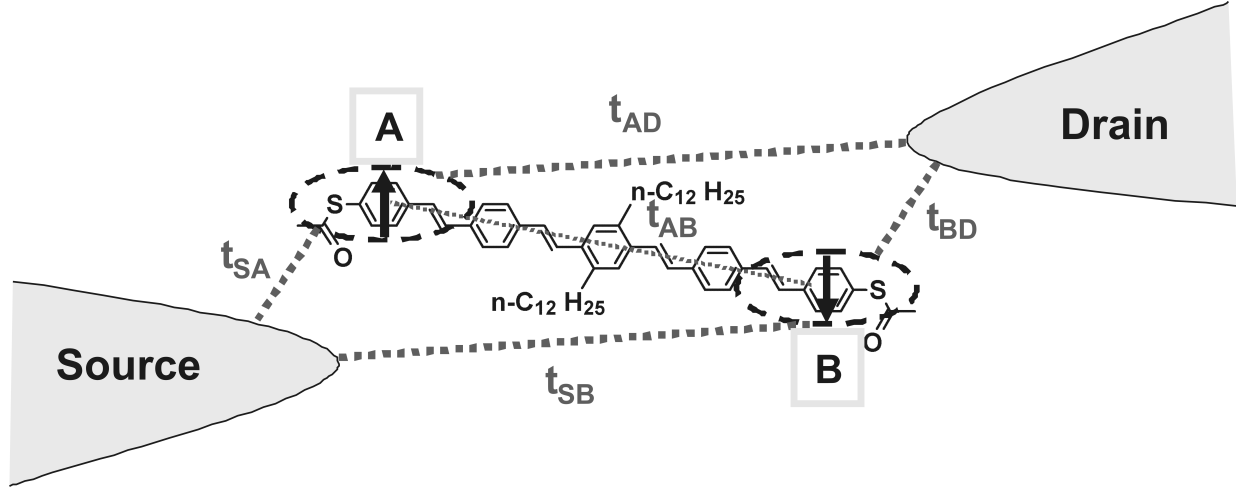


Figure A.2: Schematic drawing of the possible tunnel-couplings between the molecule and the source, drain electrodes. The black dashed ovals represent the orbitals A and B.

B. If the charged molecule was stabilized by image-charge potentials due to the metallic electrodes, one would expect these orbitals to be localized near the two leads. Nevertheless, as argued in the main text, the reduced life-time broadening and the strong sensitivity to the back-gate potential for the $N=+2$ charge state seems to indicate that the doubly charged molecule has the excess-charge localized more towards the middle of the molecule. Thus, the exact meaning of orbitals A and B cannot be the same in the different charge states $N=+1, +2$; if singly charged, the orbital A seems to be localized close to one of the leads. In the main text we argued that this observation is in fact consistent with well-known chemistry of an isolated OPV-5 molecule.

The most general situation in the $N=+2$ charge state is sketched in figure A.2, depicting an effective two-orbital Anderson model in which the proximity to the leads is modelled by four different tunnelling-amplitudes. Transport will be feasible via either orbital A ($t_{SA}t_{AD}$) or B ($t_{SB}t_{BD}$), or via AB ($t_{SA}t_{AB}t_{BD}$ or $t_{SB}t_{BA}t_{AD}$), involving a weak *inter-orbital* tunnel coupling. The corresponding two-orbital Anderson model incorporating all five tunnel-couplings is tremendously rich (cf. e.g. Refs.[19, 28–30]) but we shall restrict ourselves by drawing a few basic conclusions from perturbation theory.

The lowest lying states are well protected by a gap of roughly 35 meV up to the next excitation, comprised by many-body states with an entirely different charge-density profile. This is a remarkable separation of energy scales which is never found in traditional quantum dots, where the excitation energies are always much smaller. In our simplified model we can therefore safely leave out these high-lying states corresponding to two electrons in the same effective orbital when we want to describe merely the inelastic co-tunnelling below 2 meV. From the magnetic field dependence, the $N=+2$ ground state was argued to be an inter-orbital spin-singlet and the excited state observed at ± 1.7 meV to be a spin-triplet. In the middle of the $N=+2$ diamond charge-fluctuations are strongly suppressed and virtual

charge-fluctuations lead to an effective exchange coupling between the two spin-occupying the A,B-orbitals and the spins of the conduction electrons in the leads. Since our analysis of the addition energies shows that $dU = 42$ meV we include only the dominant virtual fluctuations in the $N=+1$ state, and omit fluctuations to the $N=+3$ state altogether. Performing this projection (*Schrieffer-Wolff* transformation) one arrives at the following effective *Kondo*-model:

$$H = \sum_{\substack{\vec{k},\sigma \\ \alpha=S,D}} (\varepsilon_{\vec{k}} - \mu_{\alpha}) c_{\alpha\vec{k}\sigma}^{\dagger} c_{\alpha\vec{k}\sigma} + J \vec{S}_A \cdot \vec{S}_B + H_{int}$$

with the antiferromagnetic exchange-coupling $J = 1.7$ meV and the exchange-tunnelling terms

$$H_{int} = \sum_{\substack{\vec{k},\vec{k}';\sigma,\sigma' \\ \alpha,\alpha'=S,D \\ i=A,B}} J_{\alpha'\alpha}^i \vec{S}_i \cdot c_{\alpha'\vec{k}'\sigma'}^{\dagger} \vec{\tau}_{\sigma'\sigma} c_{\alpha\vec{k}\sigma},$$

where $\vec{\tau}$ is the vector of Pauli matrices and where the couplings are given by $J_{\alpha'\alpha}^i = t_{i\alpha'}^* t_{i\alpha} / E_C$, assuming for now that $t_{AB} = 0$. The current carried by this exchange tunnelling is an odd function of the applied bias-voltage and in the special case where all $t_{i\alpha}$ are equal the current will in fact vanish. This is seen by writing $\sum_{i=A,B} J_{\alpha'\alpha}^i \vec{S}_i = \sum_{i=+,-} J_{\alpha'\alpha}^i \vec{S}_i$ with $J_{\alpha'\alpha}^{\pm} = (J_{\alpha'\alpha}^A \pm J_{\alpha'\alpha}^B) / 2$ and $\vec{S}_{\pm} = \vec{S}_A \pm \vec{S}_B$ and using the singlet-triplet representation $\vec{S}_+ = \vec{S}$ and $\vec{S}_- = \vec{T}$ with:

$$\begin{aligned} S^z &= |1\rangle\langle 1| - |-1\rangle\langle -1| & T^z &= |0\rangle\langle s| + |s\rangle\langle 0| \\ S^+ &= (S^-)^{\dagger} = \sqrt{2} (|1\rangle\langle 0| + |0\rangle\langle -1|) & T^+ &= (T^-)^{\dagger} = \sqrt{2} (-|1\rangle\langle s| + |s\rangle\langle -1|). \end{aligned}$$

Since only \vec{T} couples the singlet and the triplet-states there are no exchange tunnelling terms involving the singlet and therefore no current in the case of equal couplings. So, a finite current demands asymmetric couplings (the generic case) or an additional potential scattering term.

The antiferromagnetic exchange coupling J we ascribe to a super-exchange mechanism, which involves consecutive hops along the molecule. Including an *inter*-orbital tunnel coupling in our simple two-orbital model would of course alter the energy analysis in the main text slightly due to a weak mixing with (anti-)bonding states, but the dominant energy scales dU and E_C would hardly be influenced. A finite *inter*-orbital tunnelling also leads to new exchange-tunnelling terms in the effective low-energy *Kondo*-model and therefore opens an extra channel for transport. Instead of introducing bonding/anti-bonding states, we include the leading order corrections to the transport merely by going one order higher in the *Schrieffer-Wolf* transformation. This generates the additional term:

$$\begin{aligned}
H_{int}^{AB} = \sum_{\substack{\vec{k}, \vec{k}'; \sigma, \sigma' \\ \alpha, \alpha' = S, D}} J_{\alpha'\alpha}^{BA} \left\{ \left[\vec{S}_A \cdot \vec{S}_B + 1/4 \right] \tau_{\sigma'\sigma}^0 + \left[\vec{S}_A + \vec{S}_B - 2i(\vec{S}_A \times \vec{S}_B) \right] \cdot \vec{\tau}_{\sigma'\sigma} \right\} c_{\alpha'\vec{k}'\sigma'}^\dagger c_{\alpha\vec{k}\sigma} \\
+ (A \leftrightarrow B)
\end{aligned}$$

and renormalizes the exchange-interaction to $J - 2 \sum_{\alpha} (J_{\alpha\alpha}^{AB} + J_{\alpha\alpha}^{BA})$, with third order couplings $J_{\alpha'\alpha}^{ij} = t_{\alpha'i}^* t_{ij} t_{\alpha j} / E_C^2$, where $i, j \in \{A, B\}$ and $i \neq j$. In the singlet-triplet representation, the vector-product spin-operator, $-2i(\vec{S}_A \times \vec{S}_B) = \vec{T}$, contains the following matrix elements:

$$\tilde{T}^z = -|0\rangle\langle s| + |s\rangle\langle 0| \quad \tilde{T}^+ = (-\tilde{T}^-)^\dagger = \sqrt{2}(|1\rangle\langle s| + |s\rangle\langle -1|).$$

Since the vector-product is anti-symmetric in the orbital indices A and B , this term drops out when all $t_{i\alpha}$ are equal and again there will be no transitions to the triplet state. In this case only the potential scattering term gives rise to a finite (constant) conductance. Nevertheless, in the generic case with different $t_{i\alpha}$ the triplet-states will become populated at sufficiently large bias-voltage and an inelastic co-tunnelling-channel opens up at $eV = J$.

We note that the present problem is different from that of a carbon-nanotube quantum-dot at an even charging-state, which also exhibits a finite-bias singlet-triplet conductance peak (cf. Ref.[19]). In contrast to the OPV5-molecule, the electrons in a nanotube are delocalised, the exchange coupling is very small and ferromagnetic (Hund's rule), the ground-state is an *intra*-orbital (sub-band) spin-singlet and the lowest excitations comprise an *inter*-orbital spin-triplet, thus giving rise to a conductance peak at voltage equal to the orbital splitting. In the generic case of different $t_{i\alpha}$ the differential conductance of the nanotube-system is asymmetric in the bias voltage V , consistent with the experiment analysed in Ref.[19]. In the present problem, however, the inter-orbital nature of the singlet ground state implies a conductance which is symmetric in bias-voltage, unless t_{AB} is different from zero. Thus the assumption of a *weak* inter-orbital tunnelling strength is consistent with the relatively weak asymmetry of the differential conductance measured in the $N=+2$ charge state (cf. figure A.3).

The zero-bias peak observed in the middle of the $N=+1$ Coulomb-blockade diamond (cf. figure 4.3a in chapter 4) exhibits an unusual skewed line-shape at variance with the expectation for the Kondo-resonance of a singly occupied orbital. A similar skewness is observed in the $N=+2$ data (cf. figure A.3), and while it is difficult to ascertain the exact physical origin of this asymmetry the data do in fact exhibit an extra feature which points to a second molecule in parallel playing a role. That is, defining a background conductance by what must be subtracted to make the $N=+1$ peak in figure 4.3a of chapter 4 symmetric, we note that a subtraction of that same background in the $N=+2$ diamond makes those data nearly symmetric as well. In figure A.3 we show a set of dI/dV curves for different gate-voltages in the $N=+2$ diamond before and after subtraction. Clearly the

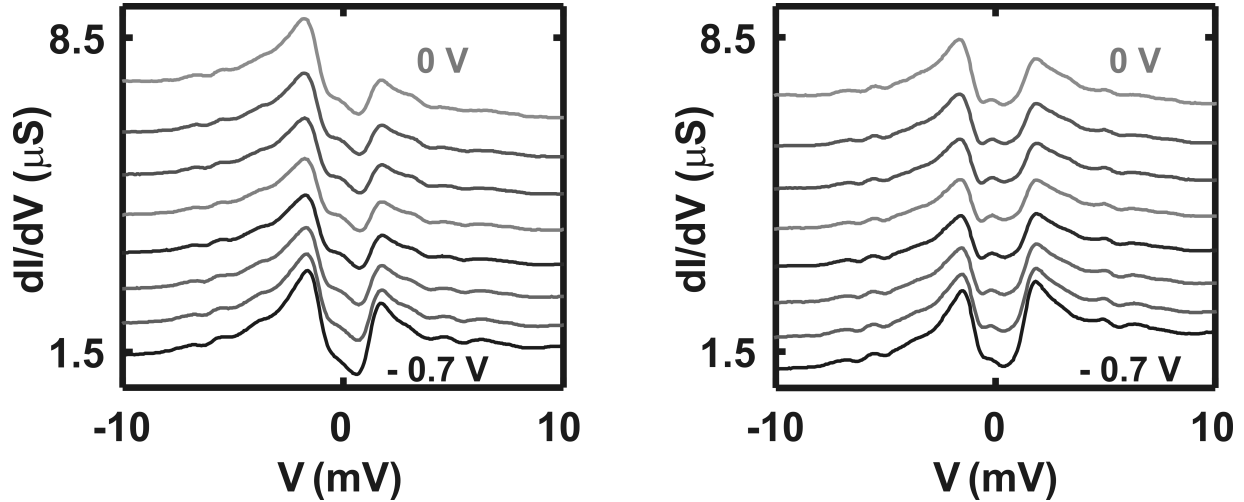


Figure A.3: Traces of the differential conductance, dI/dV , for different gate-voltages in the $N=+2$ Coulomb-blockade diamond, before (left) and after (right panel) subtracting an asymmetric background deduced from symmetrising the zero-bias peak observed in the middle of the $N=+1$ diamond. Curves were offset for clarity and taken at gate voltages from -0.7 to 0 V in steps of 0.1 V.

middle curve in the right panel, corresponding to gate-voltage in the middle of the $N=+2$ diamond, is almost perfectly symmetric. How exactly a molecule in parallel leads to an asymmetric background is not clear to us at this point, but one possible explanation could be an effective *band-filtering* (cf. figure 4f in Ref.[31]).

Interestingly, this background subtraction also emphasizes another feature of the data: a weak but clearly visible zero-bias anomaly. There is no source of zero-bias anomalies in our effective double-dot Hamiltonian, but a possible explanation could involve one of the low-lying vibrational modes. In the co-tunnelling regime we observe a number of vibrational modes at frequencies, which depend slightly on the charge state of the molecule. In the $N=+1$ data we observe a mode very close to 1.7 meV and assuming that this mode is also present in the $N=+2$ state, this could restore a zero-bias conductance anomaly involving the simultaneous transition from singlet to triplet and the absorption of a vibrational quantum, - a novel transport mechanism put forth in a recent paper by Kikoin *et al.* [32].

The $N=+2$ data could in principle be fitted in the same manner as was done for the carbon nanotube in Ref.[19], to quantify the relative strength of the Kondo-correlations and non-equilibrium effects involved in the conductance peaks near $V = \pm J$. The Hamiltonian is slightly different, but the renormalization group equations look similar and the rest of the calculation proceeds exactly as described there. However, since we cannot fully determine the influence from the background we choose not to present any quantitative fit to these data. *Qualitatively*, we observe well-developed peaks of width comparable to J and a rounded “valley” for voltages smaller than J , which indicates a marked influence of both Kondo-correlations and non-equilibrium effects (cf. Ref.[19]).

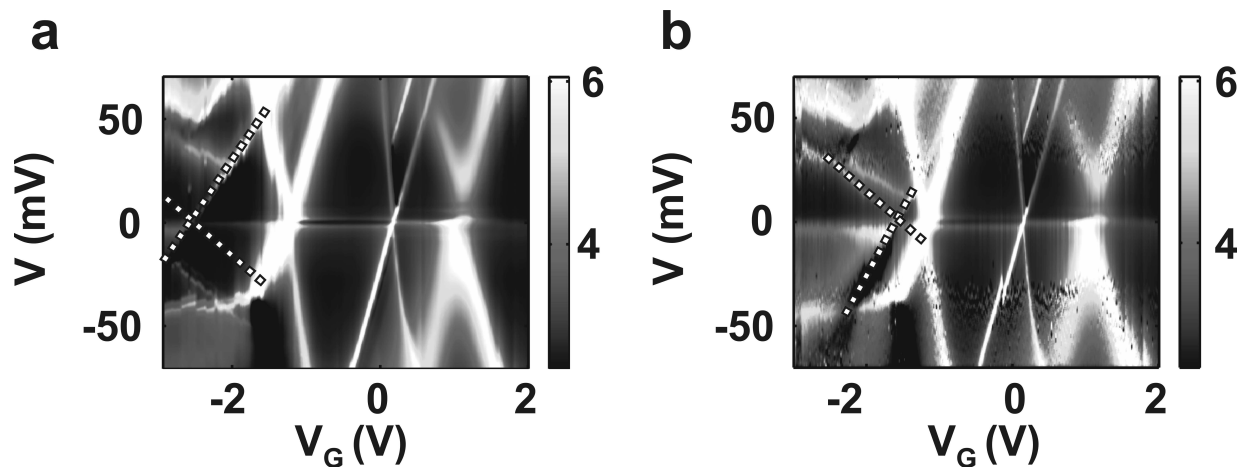


Figure A.4: Two-dimensional colour plot of the differential conductance, dI/dV , versus V and V_G at $T = 1.7$ K. **a**, Before the sample was transferred. **b**, After transfer into a different dewar in which magnetic field measurements could be performed. Dashed lines indicate the diamond edges of the second molecule in both plots.

A.4 Stability diagram after transferring the probe to another dewar

To perform measurements in a magnetic field, the ^4He insert had to be transferred from one dewar to another. After transfer, we have measured the dI/dV map once again using the same parameters as before. The result is shown in figure A.4b. The striking observation is that the degeneracy point on the far left has moved to a more positive gate voltage whereas all other features remained the same. This observation indicates that the degeneracy point on the left belongs to a different molecule in parallel. The shift in gate voltage can be explained by a change in its electrostatic environment, probably because the molecule has moved. In contrast, the molecule of which the features are discussed in the main paper has not moved; all details including the singlet-triplet co-tunnelling, the addition energies and the excitations are unaltered.

Note that the temperature dependent measurements presented in figure 4.2 in chapter 4 were performed before the sample was transferred into the dewar with the magnet.

References

- [1] A. Nitzan and M. A. Ratner, “Electron Transport in Molecular Wire Junctions,” *Science*, vol. 300, no. 5624, pp. 1384–1389, 2003.
- [2] C. Joachim, J. K. Gimzewski, and A. Aviram, “Electronics using hybrid-molecular and mono-molecular devices,” *Nature*, vol. 408, no. 6812, pp. 541–548, 2000.

- [3] J. R. Heath and M. A. Ratner, "Molecular electronics," *Phys. Today.*, vol. 56, p. 43, 2003.
- [4] H. Park, J. Park, A. K. L. Lim, E. H. Anderson, A. P. Alivisatos, and P. L. McEuen, "Nanomechanical oscillations in a single-C₆₀ transistor," *Nature*, vol. 407, no. 6800, pp. 57–60, 2000.
- [5] J. Park, A. N. Pasupathy, J. I. Goldsmith, C. Chang, Y. Yaish, J. R. Petta, M. Rinkoski, J. P. Sethna, H. D. Abruna, P. L. McEuen, and D. C. Ralph, "Coulomb blockade and the Kondo effect in single-atom transistors," *Nature*, vol. 417, no. 6890, pp. 722–725, 2002.
- [6] W. Liang, M. P. Shores, M. Bockrath, J. R. Long, and H. Park, "Kondo resonance in a single-molecule transistor," *Nature*, vol. 417, no. 6890, pp. 725–729, 2002.
- [7] A. V. Danilov, S. E. Kubatkin, S. G. Kafanov, K. Flensberg, and T. Bjørnholm, "Electron transfer dynamics of bistable single-molecule junctions," *Nano Lett.*, vol. 6, no. 10, pp. 2184–2190, 2006.
- [8] S. Kubatkin, A. Danilov, M. Hjort, J. Cornil, J. L. Bredas, N. Stuhr-Hansen, P. Hedegård, and T. Bjørnholm, "Single-electron transistor of a single organic molecule with access to several redox states," *Nature*, vol. 425, no. 6959, pp. 698–701, 2003.
- [9] L. H. Yu, Z. K. Keane, J. W. Cizek, L. Cheng, J. M. Tour, T. Baruah, M. R. Pederson, and D. Natelson, "Kondo resonances and anomalous gate dependence in the electrical conductivity of single-molecule transistors," *Phys. Rev. Lett.*, vol. 95, no. 25, p. 256803, 2005.
- [10] A. R. Champagne, A. N. Pasupathy, and D. C. Ralph, "Mechanically adjustable and electrically gated single-molecule transistors," *Nano Lett.*, vol. 5, no. 2, pp. 305–308, 2005.
- [11] Y. V. Kervennic, J. M. Thijssen, D. Vanmaekelbergh, R. Dabirian, L. W. Jenneskens, C. A. van Walree, and H. S. J. van der Zant, "Charge transport in three-terminal molecular junctions incorporating sulfur-end-functionalized tercyclohexylidene spacers," *Angew. Chem. Int. Ed.*, vol. 45, no. 16, pp. 2540–2542, 2006.
- [12] D. H. Chae, J. F. Berry, S. Jung, F. A. Cotton, C. A. Murillo, and Z. Yao, "Vibrational excitations in single trimetal-molecule transistors," *Nano Lett.*, vol. 6, no. 2, pp. 165–168, 2006.
- [13] M. Poot, E. Osorio, K. O'Neill, J. M. Thijssen, D. Vanmaekelbergh, C. A. van Walree, L. W. Jenneskens, and H. S. J. van der Zant, "Temperature dependence of three-terminal molecular junctions with sulfur end-functionalized tercyclohexylidenes," *Nano Lett.*, vol. 6, no. 5, pp. 1031–1035, 2006.

-
- [14] E. Lortscher, J. Ciszek, J. Tour, and H. Riel, “Reversible and controllable switching of a single-molecule junction,” *Small*, vol. 2, no. 8-9, pp. 973–977, 2006.
- [15] W. Wang, T. Lee, and M. A. Reed, “Mechanism of electron conduction in self-assembled alkanethiol monolayer devices,” *Phys. Rev. B.*, vol. 68, no. 3, p. 035416, 2003.
- [16] L. Venkataraman, J. E. Klare, C. Nuckolls, M. S. Hybertsen, and M. L. Steigerwald, “Dependence of single-molecule junction conductance on molecular conformation,” *Nature*, vol. 442, no. 7105, pp. 904–907, 2006.
- [17] J. Nygård, D. H. Cobden, and P. E. Lindelof, “Kondo physics in carbon nanotubes,” *Nature*, vol. 408, no. 6810, pp. 342–346, 2000.
- [18] B. Babić, T. Kontos, and C. Schönenberger, “Kondo effect in carbon nanotubes at half filling,” *Phys. Rev. B.*, vol. 70, no. 23, p. 235419, 2004.
- [19] J. Paaske, A. Rosch, P. Wolffe, N. Mason, C. M. Marcus, and J. Nygård, “Non-equilibrium singlet-triplet Kondo effect in carbon nanotubes,” *Nat. Phys.*, vol. 2, no. 7, pp. 460–464, 2006.
- [20] D. R. Strachan, D. E. Smith, D. E. Johnston, T.-H. Park, M. J. Therien, D. A. Bonnell, and A. T. Johnson, “Controlled fabrication of nanogaps in ambient environment for molecular electronics,” *Appl. Phys. Lett.*, vol. 86, no. 4, p. 043109, 2005.
- [21] H. Park, A. K. L. Lim, A. P. Alivisatos, J. Park, and P. L. McEuen, “Fabrication of metallic electrodes with nanometer separation by electromigration,” *Appl. Phys. Lett.*, vol. 75, no. 2, pp. 301–303, 1999.
- [22] N. Stuhr-Hansen, J. Christensen, N. Harrit, and T. Bjørnholm, “Novel synthesis of protected thiol end-capped stilbenes and oligo(phenylenevinylene)s (OPVs),” *J. Org. Chem.*, vol. 68, no. 4, pp. 1275–1282, 2003.
- [23] K. O’Neill, E. A. Osorio, and H. S. J. van der Zant, “Self-breaking in planar few-atom Au constrictions for nanometer-spaced electrodes,” *Appl. Phys. Lett.*, vol. 90, no. 13, p. 133109, 2007.
- [24] E. A. Osorio, K. O’Neill, N. Stuhr-Hansen, O. F. Nielsen, T. Bjørnholm, and H. S. J. van der Zant, “Addition energies and vibrational fine structure measured in electromigrated single-molecule junctions based on an oligophenylenevinylene derivative,” *Adv. Mater.*, vol. 19, no. 2, pp. 281–285, 2007.
- [25] L. P. Kouwenhoven, D. G. Austing, and S. Tarucha, “Few-electron quantum dots,” *Rep. Prog. Phys.*, vol. 64, no. 6, pp. 701–736, 2001.
- [26] Y. Oreg, K. Byczuk, and B. I. Halperin, “Spin configurations of a carbon nanotube in a nonuniform external potential,” *Phys. Rev. Lett.*, vol. 85, no. 2, pp. 365–368, 2000.

- [27] P. Hedegård and T. Bjørnholm, “Charge transport through image charged stabilized states in a single molecule single electron transistor device,” *Chem. Phys.*, vol. 319, no. 1-3, pp. 350–359, 2005.
- [28] V. Meden and F. Marquardt, “Correlation-induced resonances in transport through coupled quantum dots,” *Phys. Rev. Lett.*, vol. 96, no. 14, p. 146801, 2006.
- [29] V. Kashcheyevs, A. Schiller, A. Aharony, and O. Entin-Wohlman, “Unified description of phase lapses, population inversion, and correlation-induced resonances in double quantum dots,” *Phys. Rev. B.*, vol. 75, no. 11, p. 115313, 2007.
- [30] G. Zaránd, C. H. Chung, P. Simon, and M. Vojta, “Quantum criticality in a double-quantum-dot system,” *Phys. Rev. Lett.*, vol. 97, no. 16, p. 166802, 2006.
- [31] L. G. G. V. D. da Silva, N. P. Sandler, K. Ingersent, and S. E. Ulloa, “Zero-field Kondo splitting and quantum-critical transition in double quantum dots,” *Phys. Rev. Lett.*, vol. 97, no. 9, p. 096603, 2006.
- [32] K. Kikoin, M. N. Kiselev, and M. R. Wegewijs, “Vibration-induced Kondo tunneling through metal-organic complexes with even electron occupation number,” *Phys. Rev. Lett.*, vol. 96, no. 17, p. 176801, 2006.

Chapter 5

Electrical manipulation of spin states in a single gated transition-metal complex

E. A. Osorio, K. Moth-Poulsen, H. S. J. van der Zant, J. Paaske, P. Hedegård, K. Flensberg, J. Bendix and T. Bjørnholm

5.1 Introduction

The ultimate limit for downscaling nano-electronics devices is the single-molecule transistor. For most electronics, as well as spintronics applications, the vision is to tailor the electrical and magnetic properties of a device already in the chemical synthesis of the molecule. This holds the promise of unprecedented functionalization of the device, in terms of built-in mechanical, conformational, optical and magnetic properties of the isolated molecule. Since, however, a molecule bridging two electrodes does not preserve all the well-characterized properties of the isolated molecule, it is of paramount importance to uncover the salient influence of the nearby electrodes [1–4]. In this letter, we demonstrate a purely electrically controlled high-spin ($S=5/2$) to low-spin ($S=1/2$) transition within a single-molecule device containing a Mn^{2+} ion coordinated by two terpyridine ligands. Adjusting the gate-voltage we are able to reduce the terpyridine moiety and thereby strengthen the ligand-field on the Mn -atom. Adding a single electron thus stabilizes the low-spin configuration and the corresponding sequential tunneling current is seen to be suppressed by spin-blockade [5]. From low-temperature inelastic cotunneling spectroscopy, we infer the magnetic excitation spectrum of the molecule and uncover also a strongly gate-dependent singlet-triplet splitting on the low-spin side. The measured bias-spectroscopy is shown to be consistent with an exact diagonalization of the Mn -complex, and an interpretation of the data is given in terms of a simplified effective model. Leaving aside their vast importance in bioinorganic chemistry, transition metal complexes [6–8] are particularly interesting for molecular spintronics devices [9–12]. With the present findings, we have demonstrated direct electrical control of the spin-ground state of a single metal complex, utilizing the gate-dependence of the ligand-field strength. Harnessing the ligand-electrode couplings thus opens an exciting window towards electronic functionalization of this class of single-molecule junctions.

5.2 Experimental details and results

Devices are made by electromigration [13] of a gold wire in a solution of the molecules, using a feedback mechanism [14] combined with self-breaking [15] (see figures 5.1a and 5.1b for a likely structure of the device). Details of our fabrication and junction preparation are described in Ref. [16] and the molecule synthesis and characterization is described in section A.1 of the appendix. We focus on a particular Mn^{2+} junction with intermediate coupling to source and/or drain electrodes, and concomitant Kondo effects [17–19] as well as pronounced inelastic cotunneling lines [20, 21]. The transport measurements are represented in figure 5.2, in which we plot the differential conductance as a function of the applied bias, and gate voltage, showing the typical ‘diamond’ signatures of Coulomb blockade (CB). As we shall argue (cf. also section A.2 of the appendix), these data reflect two molecules in parallel: one (molecule B) giving rise to the two sharp white crosses separating regions (I-III) and another (molecule A) leading to the much broader cross separating regions (1) and (2). In this letter, we focus on the more strongly coupled

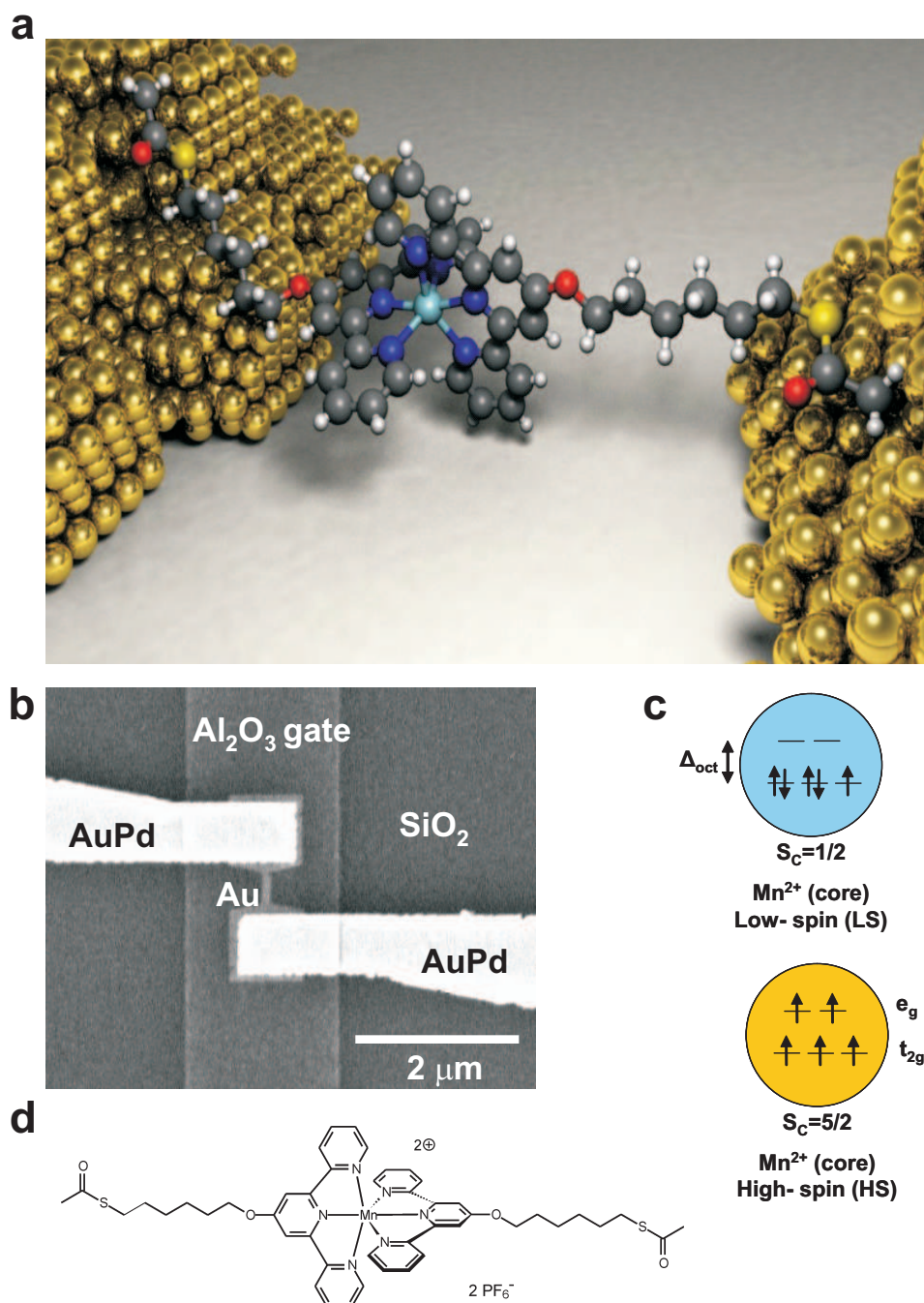


Figure 5.1: **a**, Artistic impression of a $([\text{Mn}(\text{terpy-O}-(\text{CH}_2)_6\text{-SAC})_2]^{2+})$ molecule bonded to two gold electrodes and lying on top of an aluminium gate. **b**, Fabricated device prior to breaking the small gold wire in the middle by electromigration. The junction is fabricated on top of an aluminium gate electrode, which is oxidized in air to form a 2 to 4 nm thick Al_2O_3 layer and at low temperatures, substantial leakage currents are typically observed for voltage above ± 4 V. Bridges are electromigrated in the molecule solution at room temperature by ramping a voltage until a decrease in the conductance is observed, upon which the applied voltage is returned to 100 mV; the cycle is repeated until a target resistance of 5 k Ω has been reached. The electromigrated bridges are then left in the molecule solution for about 1 hour to allow for molecular self-assembly and “self-breaking” of the constricted gold wire. Last, the sample space is evacuated and the cooling procedure to 1.7 K starts. **c**, Two different d^5 electronic configurations of the Mn^{2+} core with respectively low, and high spin are given. The d -orbitals on the Mn atom are split by the nearly octahedral ligand field of the organic terpyridine cage into three (lower) t_{2g} orbitals and two (upper) e_g orbitals. **d**, Molecular structure of $([\text{Mn}(\text{terpy-O}-(\text{CH}_2)_6\text{-SAC})_2]^{2+})$. The derivative has CH_6 alkane chains attached to the ligands and acetyl protected thiol end groups to ensure bonding with the gold electrodes.

molecule (A), which exhibits pronounced spin-blockade prohibiting low-bias transport at the observed charge-degeneracy point. This molecule (A) also gives rise to sharp inelastic cotunneling lines pervading all of region (2) and revealing a marked gate dependence of the spin-excitations on this molecule.

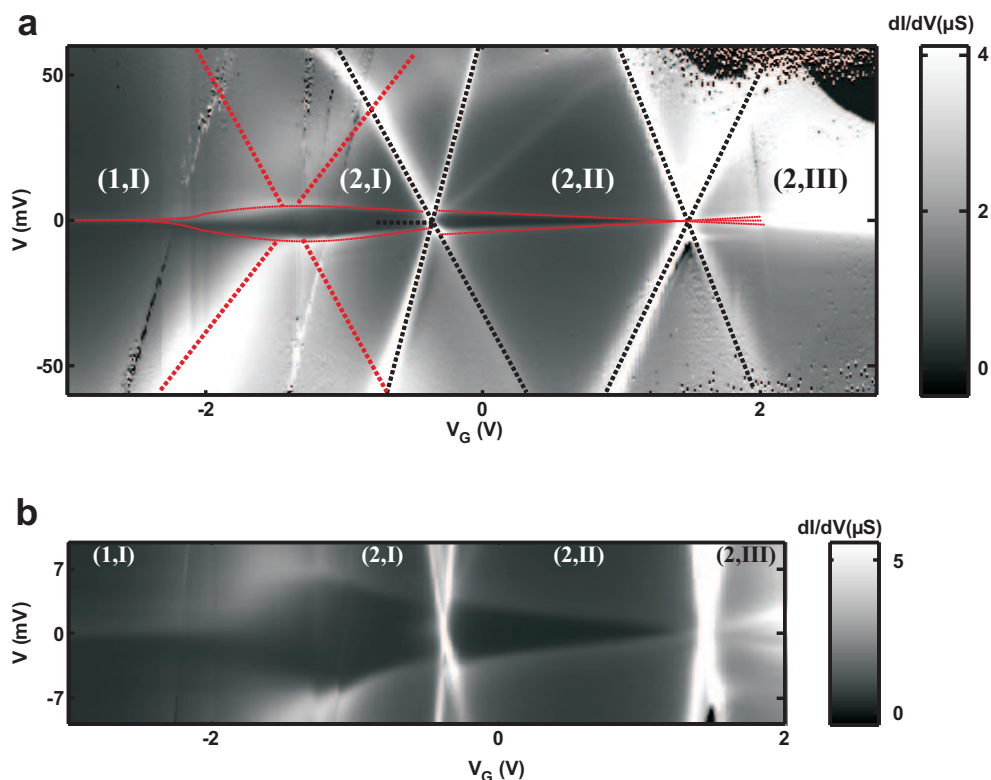


Figure 5.2: **a**, Two dimensional density plot of the differential conductance, dI/dV , versus V and V_G at $T = 1.7$ K. The different charge states of respectively the main molecule and the molecule in parallel are indicated by (i,j) with $i=1,2$ and $j=I, II, III$. The molecule in parallel gives rise to two very similar white crosses of high conductance due to sequential tunnelling (black dotted lines). The main molecule displays only a single cross (red dotted lines) corresponding to sequential tunnelling, which is strongly perturbed due to its very strong coupling to one, but not the other electrode, and due to the spin-blockade hindering ground state to ground state transport at low-bias. **b**, Low bias zoom-in of the different crossings and charge states without any guides to the eye.

To resolve the spin-configurations in the two charge-states (1-2) of molecule A, we have measured magnetic field dependence of the inelastic cotunneling lines (figure 5.3). In a field of 10 Tesla, the inelastic cotunneling lines in region (2) are observed to cross at zero bias voltage for a gate voltage V_C denoted by an orange dot in figure 5.3b. On the left hand side of this crossing, three equally spaced lines are observed (red, blue, and green lines). On the right hand side, blue, and green excitations become gate independent. This behaviour with magnetic field points at an interesting interplay between a singlet (S), and a triplet (T) state [22, 23] with a gate-dependent antiferromagnetic exchange coupling, $J(V_G)$, as illustrated in figure 5.3c (bottom panel).

From the Zeeman splitting of the triplet states (figure 5.3d: bottom panel), the excitation pattern observed in charge state (2) indicates that the crossing point at zero bias voltage marks a transition from a singlet ground state (left) to a triplet ground state (right). On the left hand side of V_C the excitations from the singlet ground state to the three components of the triplet give rise to three equally spaced resonances [21, 23] separated by $g\mu_B B$. The splittings in figure 5.3b yield a g -factor of $g \approx 1.8$. On the right hand side, the T_{-1} component of the triplet is the ground state, and the observed resonances are consistent with inelastic cotunneling from the T_{-1} state to the singlet S , T_0 and T_{+1} states [21, 23]. Again, the energy diagram in figure 5.3d predicts the $T_{-1} \rightarrow S$ transition to be gate dependent (red line), whereas for the $T_{-1} \rightarrow T_0$ and the $T_{-1} \rightarrow T_{+1}$ transitions (blue and green lines) no gate dependence is expected. The fact that V_C moves towards smaller gate voltages for increasing magnetic field is also consistent with the energy diagram presented in figure 5.3d. Further details on the assignment of spin-states is provided in the appendix, section A.3.

In the left-most section of (1) and right-most section of (2), we observe zero-bias Kondo-peaks indicating spin-degenerate ground states. As shown in figure 5.3f, these undergo a simple Zeeman splitting in a magnetic field with corresponding g -factors of 2.1 ± 0.3 , and 1.9 ± 0.3 , respectively (cf. appendix, section A.5). As shown below, this detailed magnetic field dependence of the bias-spectroscopy allows us to build up a consistent model for the electronic configurations of molecule A in the measured gate-range.

From our bulk SQUID susceptibility measurements (cf. appendix, section A.1) we find that the metal complex in its crystalline form has a high-spin (HS) ground state with $S=5/2$. This is as expected from ligand-field theory since exchange interactions at the metal core are large enough [24, 25] to overcome the nearly octahedral energy splitting Δ_{oct} [26]. Thus it would be natural to assign the high-spin ground state with $N=5$ d -electrons on the Mn -atom to region (1), which makes region (2) a 6-particle state, with an extra electron fluctuating between the Mn d -orbitals and a ligand state. From the magnetic field dependence of the bias-spectroscopy we know that regions (2,I-II) have a singlet ground-state and therefore the Mn -centre must have changed into a low-spin (LS) configuration, which can be paired with the single spin 1/2 of an added electron to produce the observed singlet. Several factors could contribute to stabilizing the unusual [27] low-spin state of the manganese(II) centre including loss of solvation and counter ion interactions, but the likely cause is the increase in ligand-field strength of the terpyridine ligand system upon reduction. It should be noted that reduction of terpyridine ligands coordinated to divalent metal centers is known, even for systems in solution [28]. Thus, charging the ligands by increasing the gate-voltage can indeed be expected to inflict a transition from HS to LS in the Mn -centre. This in turn explains the spin-blockade [5], restricting sequential tunnelling near the $N=5,6$ charge degeneracy point to excited states available only above a finite bias corresponding roughly to the nearby inelastic cotunneling threshold. The spin-blockade is lifted when bias-voltage is large enough to populate the excited states, i.e. states with $N=5$, $S=1/2$ in (1) and $N=6$, $S=1$ in (2). Unlike the respective ground-states, these low-lying excited states do couple via one-electron fluctuations. Transport thus takes place by means of cotunneling assisted sequential tunnelling, known from experiments on quantum

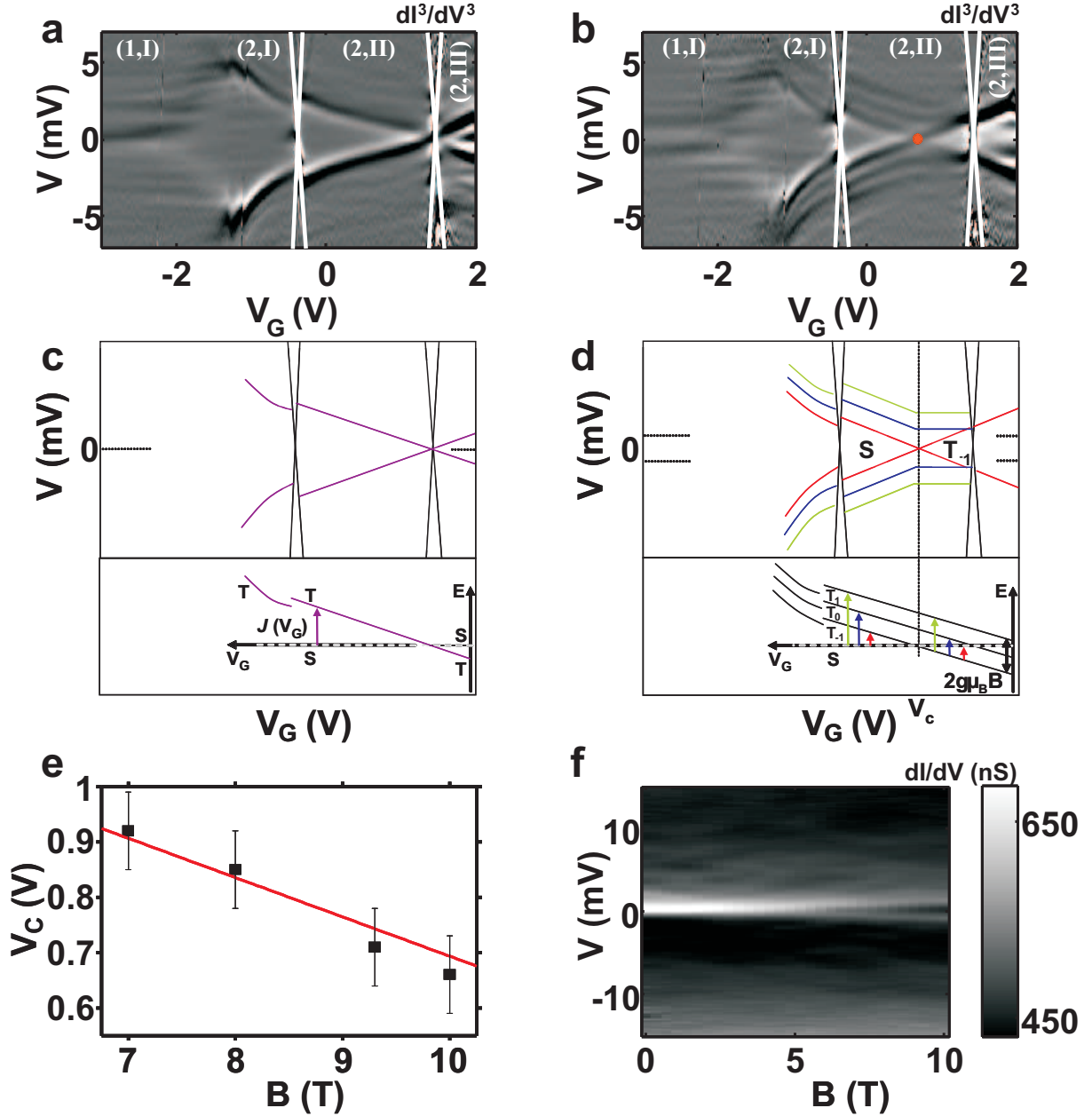


Figure 5.3: **a**, Gray scale plot of dI^3/dV^3 as a function of V and V_G at $T=1.7$ K and zero magnetic field obtained by numerical differentiation of the dI/dV which was measured with a lock-in technique. We have plotted the third derivative in order to enhance the contrast of the low-bias features; resonances in the first derivative appear as dips (dark lines) in the third derivative. Almost vertical thick white lines were superimposed on the plot at the diamond edge locations as a guide to the eye. **b**, Same as **a** but at $B=10$ T. **c**, Top: schematic drawing of the important low-bias features observed in **a**. Bottom: energy diagram of the gate-dependent singlet (S) to triplet (T) transition observed in charge state (2). The energy splitting between S and T is given by the gate-dependent exchange coupling $J(V_G)$. **d**, Top: schematic drawing of **b**. Bottom: energy diagram with Zeeman splitting of the triplet states. Arrows indicate all observed transitions in charge state (2,I-III). The vertical dashed line locates the $S-T_{-1}$ crossing; as indicated on the top part, the singlet (triplet) is the ground state at the left (right) side of this line. **e**, Squares: gate voltage value of the $S-T_{-1}$ crossing, V_C , for four different magnetic fields. Red line gives the predicted gate voltages of the $S-T_{-1}$ crossing, using the energy diagram presented in **d**, as a function of magnetic field. **f**, Gray scale plot of dI/dV vs. B -field showing a Zeeman splitting of the Kondo resonance at $V_G=-2.8$ V. From the splitting at $B=10$ T we estimate a g -factor of $g = 1.9 \pm 0.3$.

dots [29]. Finally, we note that the observation of zero-bias Kondo peaks in left part of region (1) and right part of region (2) is again consistent with the Mn -centre having $S=5/2$ in (1) and $S=1$ in right part of (2).

To gain further insight about the electronic configurations for the two charge-states of molecule A, we have diagonalized the fully interacting 5 and 6-electron problems for an isolated Mn -complex. We include the three t_{2g} , and two e_g d -orbitals on the Mn -atom, split by an energy Δ due to the nearly octahedral ligand-field, together with two ligand states made out of p_z -orbitals on the N-atoms. We include electrostatic Coulomb repulsion, U , and ferromagnetic exchange, K , among the d -electrons. Furthermore, electrons on either of the ligand orbitals are allowed to tunnel onto a corresponding t_{2g} d -orbital with matching symmetry. Interestingly, we find that for a large range of realistic parameters the calculations reproduce the main features of the data: Singlet, and triplet states with a gate-dependent exchange energy in the meV range, a singlet ground state in regions (2,I-II) with the triplet as the first excited state and a high spin $5/2$ ground state in region (1,I) with a low lying excited state of spin $1/2$.

The gate dependence of the singlet-triplet splitting observed throughout region (2, I-III) can readily be explained by a difference in gate-coupling for the two terpyridine moieties, arising naturally in the asymmetric device configuration envisioned in figure 5.1a. This must be considered the generic geometry insofar as a more source-drain symmetric arrangement would impose strict conditions on the size and topology of the gap. Such geometrical desymmetrization of the system is also consistent with the broad, yet relatively low sequential tunnelling conductance ridge separating regions (1) and (2) in figure 5.2a, which is to be expected with a large difference in tunnel-couplings to source, and drain electrodes. In section A.4 of the appendix we report also the observation of a faint, nearly vertical, line pinned to the singlet-triplet transition point. Our calculations of the nonequilibrium cotunneling conductance show that this line is only to be expected with a substantial source-drain asymmetry in the tunnel couplings. In this asymmetric geometry, electrons on the terpyridine closer to an electrode or on the Mn -atom are screened by the nearby metallic electrode. These electrons will therefore be much weaker coupled to the back-gate potential than electrons on the central terpyridine moiety. Figure 5.4 illustrates the results of our exact diagonalization in terms of the few many-body states which turn out to dominate the exact result. From these states it becomes apparent that the triplet state gains an extra ferromagnetic exchange energy compared to the singlet state when an electron is shifted more toward the central (gate sensitive) ligand orbital by further increasing V_G and moving right in region (2,I-III). We will present more details on these calculations on a forthcoming publication.

5.3 Conclusion

In conclusion we have demonstrated that the gate electrode in these experiments can be conceived as a tunable external ligand, which allows control over the spin states of devices built from transition metal centers. With this added functionality, metal centers

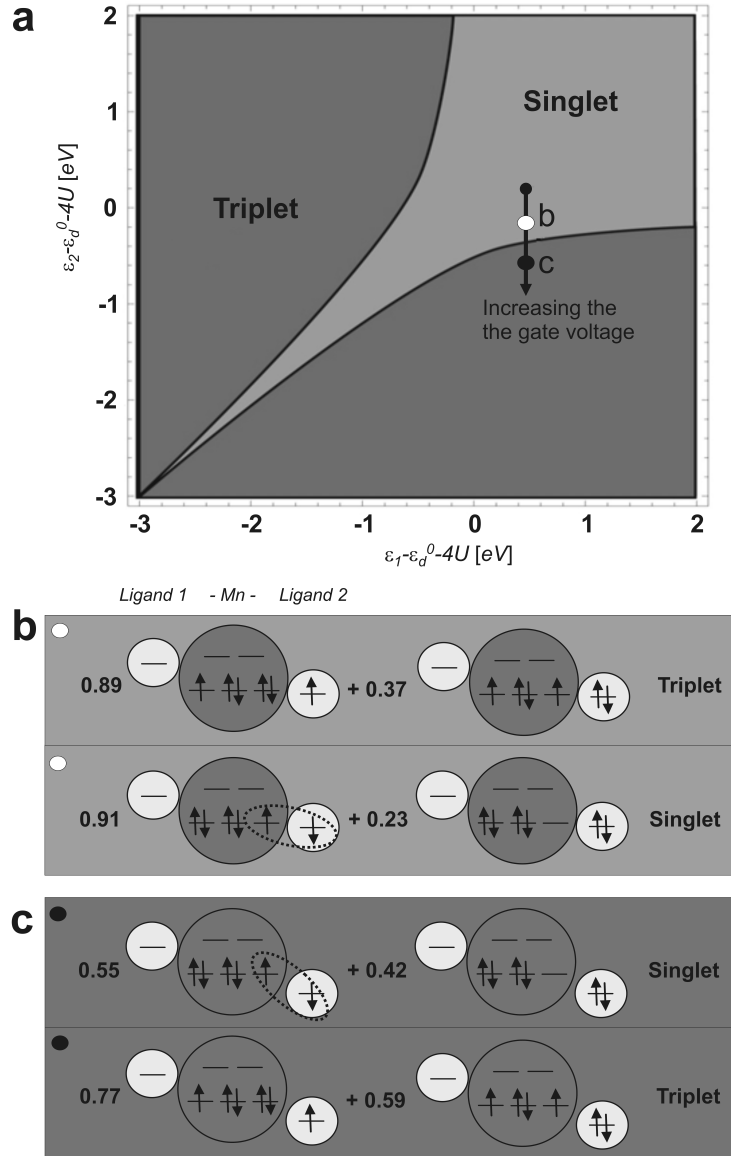


Figure 5.4: **a**, Phase diagram demarcating the regions for which the ground state of the $N=6$ electron system is respectively a spin singlet (light grey) or a spin triplet (dark grey). The control parameters on the axes represent the energy-levels of the relevant ligand states which hybridize with the Mn d -electrons. Due to the strongly asymmetric device geometry, the terpyridine moiety lying away from the leads will be screened by the nearby metallic lead and therefore only the ligand level of this central terpyridine (ligand 2) feels the gate potential. Increasing V_G lowers the energy of ligand 2 (ϵ_2 following the black arrow) and the ground state eventually changes from singlet to triplet as observed in figure 5.3(a-b). **b**, The phase diagram in **a** is calculated from an exact diagonalization which reveals a simple understanding in terms of the 6-particle states shown here. Lower (upper) state is a spin singlet (triplet) and the singlet is the ground state at the point in parameter space corresponding to the white dot in panel **a**. **c**, Same as **b**, except that ϵ_2 has now been moved down to the location of the yellow dot in panel **a** and the triplet has become the ground state. As indicated by their numerical coefficients, these states dominate the exact eigenstates and they allow for a simple interpretation of the cause of the gate-dependent singlet-triplet splitting: basically the triplet is stabilized by charge fluctuations between the d , and the ligand orbitals since it gains more from the Hund's rule coupling on the Mn -core. Increasing the gate-voltage lowers ϵ_2 and, as reflected in the different numerical coefficients, more weight is put on the component with a doubly charged ligand 2, i.e., the component where the triplet is lowered more in energy from Hund's rule coupling. Parameters for this plot were chosen to be $U=5.0$, $\epsilon_d^0 + 4U=0$, $\epsilon_1=0.6$, $\epsilon_2=-0.3$, $K=0.8$, $\Delta=2.0$, $t=0.26$, $t'=0.1$; all in units of eV .

with multiple accessible spin states provide an extra possibility for designing and controlling the transport of charge and spin through single molecule devices.

Appendix

A.1 Molecule synthesis and characterization. *University of Copenhagen*

Below we describe the synthesis method and characterization of the molecule used in this work: **Bis-4'-(6-acetylthiohexyloxy)-2,2';6',2''-terpyridine manganese(II) hexafluorophosphate.**

4'-(6-Acetylthiohexyloxy)-2,2';6',2''-terpyridine [6] (204 mg, 0.5 mmol) was dissolved in acetone (20 mL) and heated to 50°C. A solution of Manganese(II)acetate tetrahydrate (61 mg, 0.025 mmol) in milliQ water (5 mL) was added, and the reaction mixture stirred for 1 hour. The solution was allowed to cool to room temperature and poured into 0.2 M aqueous potassiumhexafluorophosphate solution (100 mL). The resulting slurry was filtered through filter aid (Celite) and washed with water (200 mL) and ether (200 mL). Finally the celite was washed with acetone, to transfer the product. Evaporation of the acetone in vacuo afforded 160 mg of bis-4'-(6-acetylthiohexyloxy)-2,2';6',2''-terpyridine manganese(II) hexafluorophosphate 12 as a white powder, corresponding to 55% yield.

Mp: 83.3-85.2°C. Anal. Calcd. for $C_{46}H_{52}N_6O_5F_{12}P_2S_2Mn$ (M+H₂O): C, 46.87; H, 4.45; N, 7.13; Found: C, 46.98; H, 4.20; N, 6.99; MS (ESP⁺ (acetonitrile) shows a peak at $m/z = 434.5$ (100), 435.0 (80), 435.5 (50), 436.1 (60), 436.6 (20), 437.1 (20) corresponding to $M^{2+} - 2PF_6$.

The NMR spectra showed strong line broadening due to manganese(II). ¹H NMR (400 MHz, acetone-d₆): δ 1.38 (12H), 1.74 (4H), 2.58 (6H), 2.82 (4H), 4.19 (4H), 7.45 (4H), 7.93 (8H), 8.67 (8H). It was not possible to obtain a C¹³ spectrum due to the presence of the magnetic Mn²⁺. Crystals for single crystal X-ray diffraction were obtained by slow diffusion of water into an acetonitrile solution of the complex [30].

Magnetic response was recorded on a powdered crystalline sample (6.28 mg) in a gelatine cup (see figure A.1). Data were corrected for diamagnetism of the container and for diamagnetism of the compound by use of tabulated values of Pascals constants. Measurements were performed on a Quantum Design MPMS5 system calibrated on a palladium sample and on CoHg(NCS)₄. The temperature independent magnetic moment with a value of close to 6 Bohr magnetons (theoretical spin-only value: 5.92 B.M.) is indicative of only weakly interacting high-spin manganese(II) centers.

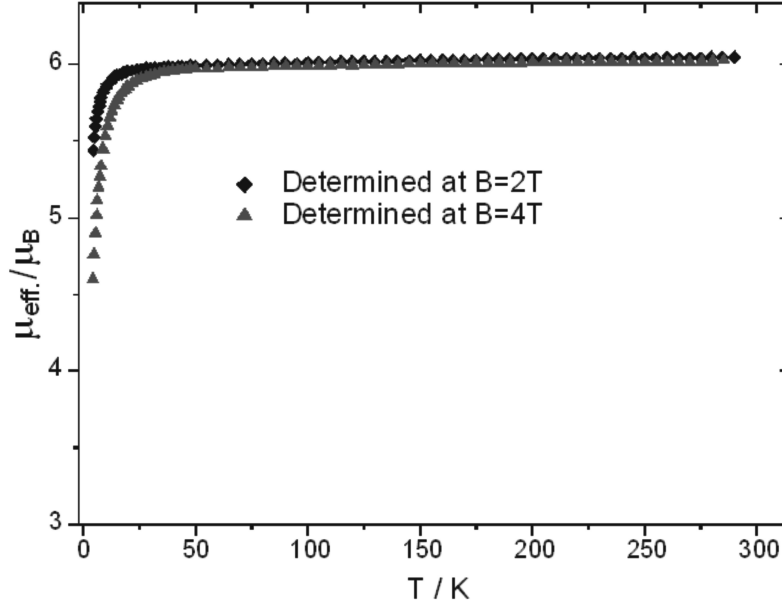


Figure A.1: Magnetic susceptibility of the bulk sample.

A.2 Assignment of the low-bias features: two molecules in parallel.

Figure A.2 shows the same stability diagram as shown in figure 5.2a of the main text. Below, we shall argue why these data reflect electron transport carried by two molecules in parallel, and how the various low-bias conductance features can be consistently assigned to these two different molecules.

As indicated in figure A.2 by dashed black lines, the transport measurements exhibit two crossing points with equally sharp diamond boundaries having roughly the same slope. This is a strong indication that these two crossings separating regions (2-4) correspond to transport through the same molecule (Molecule B). Moreover the sharpness of these lines tell us that this is a relatively weakly coupled dot, with a coupling Γ to the leads of the order of a few meV, as compared to the charging energy which is of the order of $0.1 eV$.

Between regions (1) and (2), we observe a much broader and lower ridge of high conductance which bears little resemblance to the two sharp crosses. Although it is difficult to draw diamond boundaries due to the large broadening, a slightly curved version of the sketched cross drawn with solid black lines is clearly present. We interpret this as sequential tunneling through a different molecule (Molecule A) which is stronger coupled (broader ridge) and quite asymmetrically (lower peak-heights) coupled to source, and drain. In (4), we observe a similar region of high conductance and large broadening which is likely to be connected to single-electron tunneling transport through molecule A.

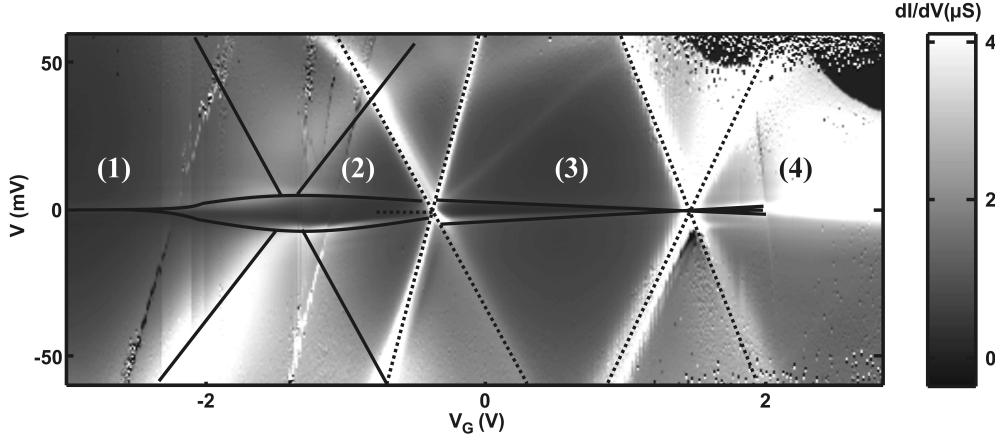


Figure A.2: Same density plot as shown in figure 5.2a of the main text. Distinct regions defined by ridges of high sequential tunneling conductance are numbered (1- 4).

Zooming in on the low-bias features near the (2-3) cross (figure A.3), we observe that the gate-dependent cotunneling lines in (3) continue through the single-electron tunneling (SET) region into region (2) with hardly any change in their slopes. Figure 5.3b in the main text also shows that at high magnetic fields these lines display an identical splitting in three branches in regions (2) and (3). These observations again indicate that the two signals are merely superimposed, i.e., derived from two different molecules. When crossing into region (2), the cotunneling lines are shifted a bit downwards (cf. figure 5.3a of the main text). The transition from (3) to (2) corresponds to the withdrawal of one electron from molecule B, and therefore this shift seems to indicate a capacitive coupling between the two molecules since this transition implies a change in the electrostatic environment of molecule A. From figure A.3, we also observe a zero-bias Kondo resonance in (2). The intensity of this Kondo resonance vanishes rapidly towards more negative voltages, indicating that it is connected to the charge degeneracy point of molecule B.

Following the cotunneling lines further left from region (2) into region (1), they change dramatically upon crossing the diamond boundaries (schematically shown by solid black lines) of molecule A. The lines bend towards the zero-bias axis and a Kondo resonance appears at the far left (cf. section A.5). As described in the main text, this can be understood in terms of a transition from low, to high-spin giving rise to spin-blockade which suppresses the low-bias part of the SET cross. This entire spin-blockade scenario again makes it very natural to associate the two dominant gate-dependent cotunneling lines with molecule A.

Going (right) towards larger gate-voltages, the two gate-dependent cotunneling lines in (3) extend into region (4) without any change in their slopes. Incidentally, the two lines cross zero practically at the point of transition from (3) to (4). As discussed already in the main text, the presence of a zero-bias Kondo resonance in region (4) at $B=0$ T is consistent with a triplet ground state. From figure A.4 we observe that the intensity of this Kondo

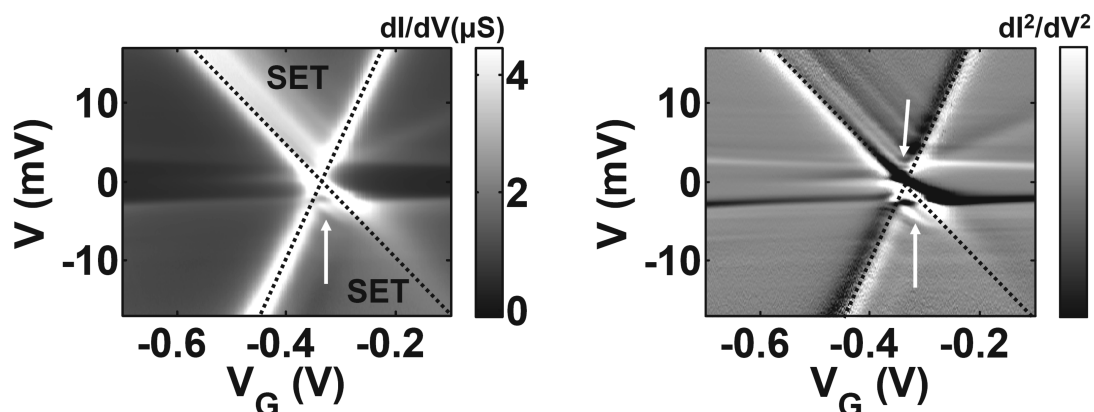


Figure A.3: Zoom-in of the low-bias region of the cross separating regions (2) and (3). Showing both first (left panel), and second (right panel) derivatives of the current.

resonance increases when going (right) further into region (4), indicating again that it is connected to the high conductance region on the far right, which we have attributed to molecule A.

Altogether, this interpretation of the whole set of transport data provides a consistent interpretation of regions (1-4) as the signal from two molecules in parallel. As we have argued, the two molecules are coupled very differently and we presume that this is the reason why only one of the two molecules shows the high-spin low-spin transition with the concomitant spin-blockade.

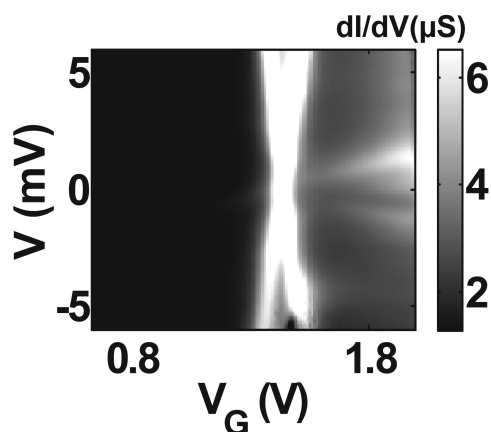


Figure A.4: Zoom-in on the low-bias region of the crossing from region (3) to region (4). A zero-bias Kondo-peak with a gate-dependent Triplet-Singlet excitation grows stronger further inside region (4).

Notice that a total of 206 samples incorporating the $([\text{Mn}(\text{terpy-O}-(\text{CH}_2)_6\text{-SAC})_2])^{2+}$ molecule have been measured. For all samples, electromigration was carried out using

a self-breaking method which has proven to significantly reduce the chances of creating small gold nano-particles during this process [15]. In nine of these 206 junctions transport could be attributed to transmolecular conduction; our reported yield is comparable with the work by other groups, i.e. a few percent [31]. In figure A.5, we show low-temperature measurements taken on a different sample in which only two charge states were accessible. The observed sharp spectroscopic lines in the SET region and the absence of cotunneling features indicate weak electronic coupling. Given the energy spacing of the excitations (a few meV) and their appearance at more or less the same energies for two subsequent charge states, we argue that the observed excitations originate from vibrational modes. Only the sample shown in the main paper had enough information in the stability plot for us to unambiguously identify the charge and spin states.

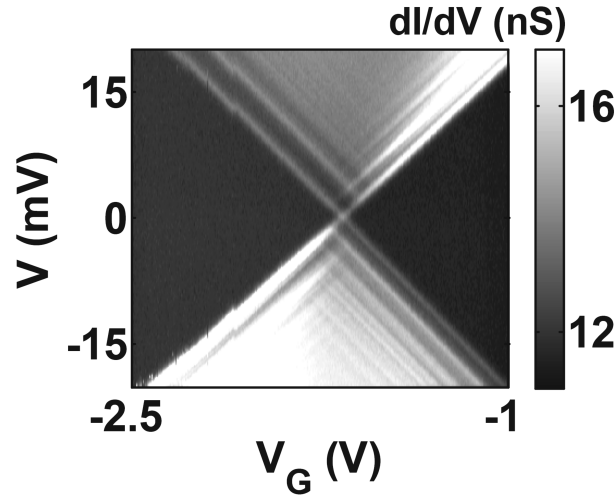


Figure A.5: Stability diagram measured on a different three-terminal junction with $([\text{Mn}(\text{terpy-O}-(\text{CH}_2)_6\text{-SAC}_2)]^{2+})$, at $T = 1.6$ K.

A.3 Details on the assignment of spin states.

In this section we provide additional details to support the assignment of the different spin states as discussed in the main text. First, the transition $|S\rangle \rightarrow |T_0\rangle$ in regions (2) and (3), should be magnetic field independent as the difference in angular momentum between these states is zero. In figure A.6 we present the same plots as in figure 5.3 of the main text (same bias and gate range is used). For the measurement at zero magnetic field (figure A.6a) we have drawn the gate-dependent cotunneling lines in (2) and (3): dotted and dashed lines respectively. We have then copied these lines on the measurement at high magnetic fields at the same locations in figure A.6b. We see that the dashed lines match the $|S\rangle \rightarrow |T_0\rangle$ excitation (middle resonance on the left hand side of the $S\text{-}T_{-1}$ crossing). A similar agreement is found for the dotted lines.

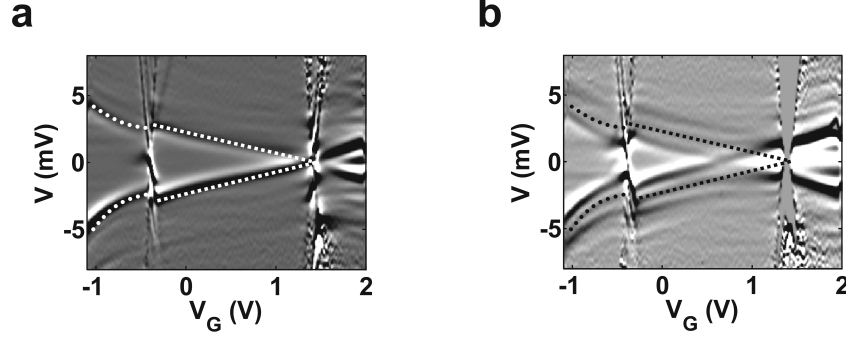


Figure A.6: a, b, Plots similar to figures 5.3a and 5.3b of the main text. In **a**, dotted lines are drawn along the gate dependent cotunneling lines in regions (2) and (3). In **b**, the lines drawn in **a** were copied to the same locations, overlapping the $|S\rangle \rightarrow |T_0\rangle$.

A.4 Enhanced cotunneling near the singlet-triplet degeneracy.

J. Paaske and K. Flensberg.

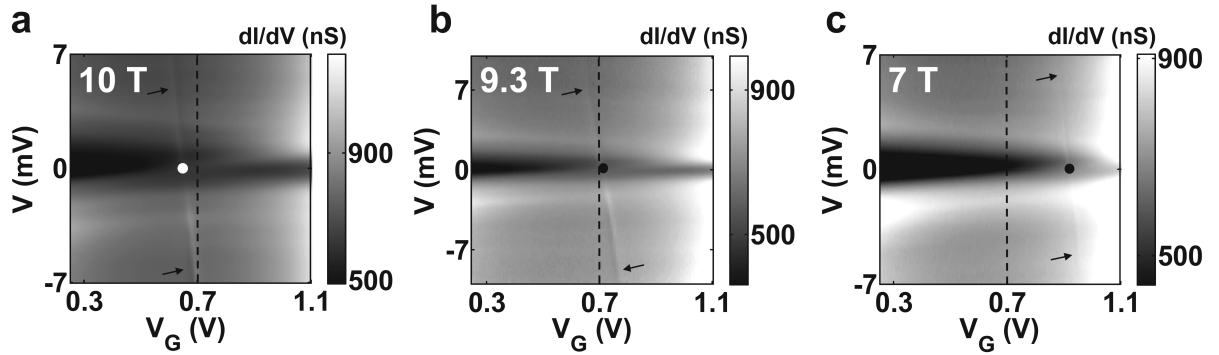


Figure A.7: **a,b,c**, Differential conductance map inside (3), at $T = 1.7$ K and for three different magnetic fields. The black(white) dot indicates the position of the $S-T_{-1}$ crossing for each panel. Black dashed line at $V_G = 0.7$ V is used as a guide to the eye. Arrows point at a resonance line that crosses the $S-T_{-1}$ degeneracy point.

We have measured the dI/dV map inside charge state (3) for three different magnetic fields, 10T, 9.3T, and 7T (see figure A.7). We observe that the $S-T_{-1}$ crossing, indicated by a black(white) dot, moves towards smaller gate voltages as we increase the magnetic field. One particular feature for all three measurements at high magnetic fields, but mainly clearly visible in figure A.7a, is the appearance of a sharp, almost vertical, line going through the $S-T_{-1}$ crossing. To our knowledge, this line has not been observed

before and as we shall argue below, it appears to have a relatively simple explanation.

Basically, this line reflects a difference in elastic cotunneling on the two different sides of the S- T_{-1} crossing which is brought out when the molecule is coupled sufficiently asymmetrically to source, and drain electrodes. This can be seen from the plots in figure A.8 produced within 2^{nd} order perturbation theory in the effective cotunneling amplitudes. To be more specific, a unitary (Schrieffer-Wolff) transformation effectively projects out all real charge-fluctuations and one is left with an effective low-energy (Kondo, or cotunneling-) Hamiltonian. For the specific problem of a spin-singlet separated from a spin-triplet by an exchange-coupling, the effective Hamiltonian and the 2^{nd} order current in the resulting amplitudes has been calculated in Ref. [32] and figure A.8 is produced from those formulas simply by assuming the singlet-triplet splitting to depend on gate-voltage (and very weakly on the bias-voltage, in order to simulate the slope of this nearly vertical feature). For a sufficiently large asymmetry in couplings to source and drain, the impurity is practically kept in its ground state: Singlet on the left, and triplet (T_{-1}) on the right side. In this case, the line arises from the fact that the elastic cotunneling matrix element for the triplet state is a factor of two larger than that for the singlet. With a slight bias-dependence on the singlet-triplet splitting a vertical step in the elastic cotunneling background finally turns into a peak ($V > 0$) or a dip ($V < 0$), respectively.

Notice that no such line was observed at the singlet-triplet crossing point investigated in Ref. [23]. According to the mechanism outlined above, this implies that the present device is much more asymmetrically coupled than the device studied in Ref. [23]. Since more than one orbital is involved in both of these systems it is not straight forward to deduce the asymmetry of the devices, but judging from the zero-bias Kondo peak heights in the neighboring odd charge-states, the device in Ref. [23] shows a saturation at 0.4 ($2e^2/h$), whereas the peak observed in charge state (1) of the present device reaches a mere 0.02 ($2e^2/h$). This, admittedly crude estimate would indeed suggest a more symmetrically coupled device in Ref. [23].

Comparing to the nearly vertical experimentally observed line, a few discrepancies still remain to be resolved. First of all, a closer investigation of the data shows that as bias voltage increases the line-shape as a function of gate-voltage has more structure to it than simply a peak or a dip. At this stage, we merely speculate that this is related to a cotunneling induced mixing of the various spin-states at higher bias-voltages. More importantly, perhaps, is the fact that the experimental line is observed to have a width of roughly 3 mV (estimated with a gate-coupling of 0.1), which is comparable to the maximum singlet-triplet splitting at zero-field. In our calculation, the extra line is only smeared by temperature, i.e., roughly 0.2 mV (1.7 K) and hence an order of magnitude too narrow.

In calculating the right panel of figure A.8 we have also included a spin-anisotropy term, $DS_z^2 + E(S_x^2 - S_y^2)$, for the spin-1 state. This term breaks the rotational invariance and angular momentum needs no longer be conserved. In our calculation this shows up as an extra $\Delta m = 2$ line reflecting a transition between T_{-1} and T_{+1} . As pointed out earlier, this extra (nominally forbidden) line is also observed in the experiment. Such anisotropies could well arise from spin-orbit coupling on the *Mn*-atom in the presence of a nearly octahedral ligand-field.

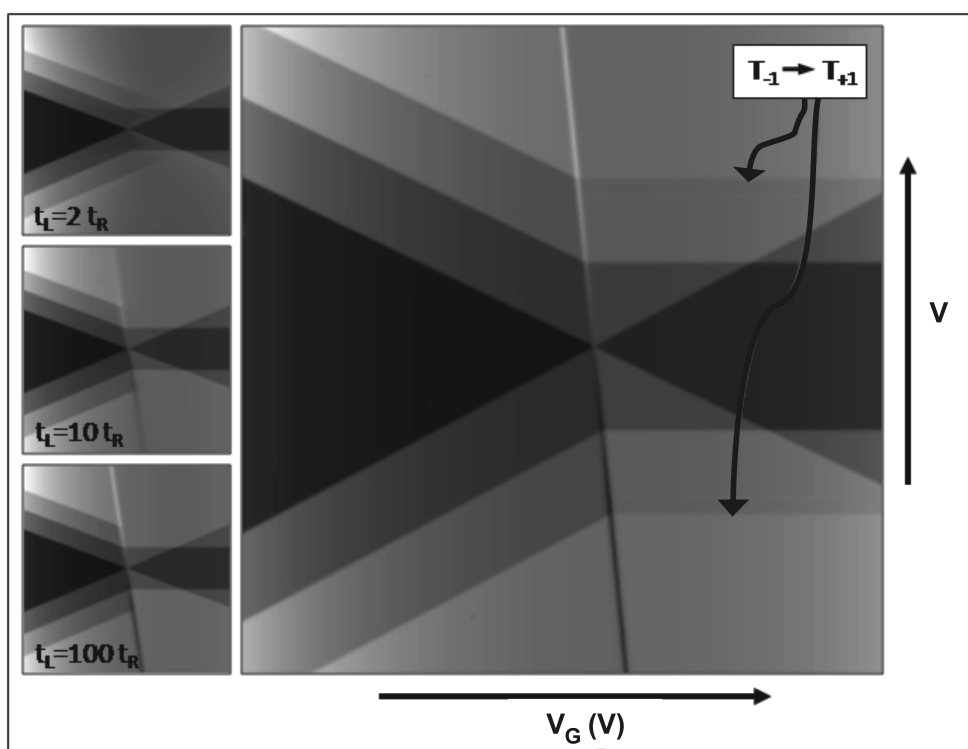


Figure A.8: Differential conductance maps calculated inside charge state (3). The three left panels show a series of calculations incorporating the full effects of nonequilibrium (V -dependent) occupation numbers for the molecule-spin states. Top to bottom panels illustrate the effects of increasing source-drain asymmetry in the tunnel-couplings between molecule and electrodes. Right panel shows a similar calculation leaving out the effects of nonequilibrium occupation numbers but including an anisotropy term which mixes the T_{-1} and the T_{+1} components of the triplet. Parameters are chosen to match experimental conditions.

A.5 Kondo effects: Magnetic field and temperature dependence.

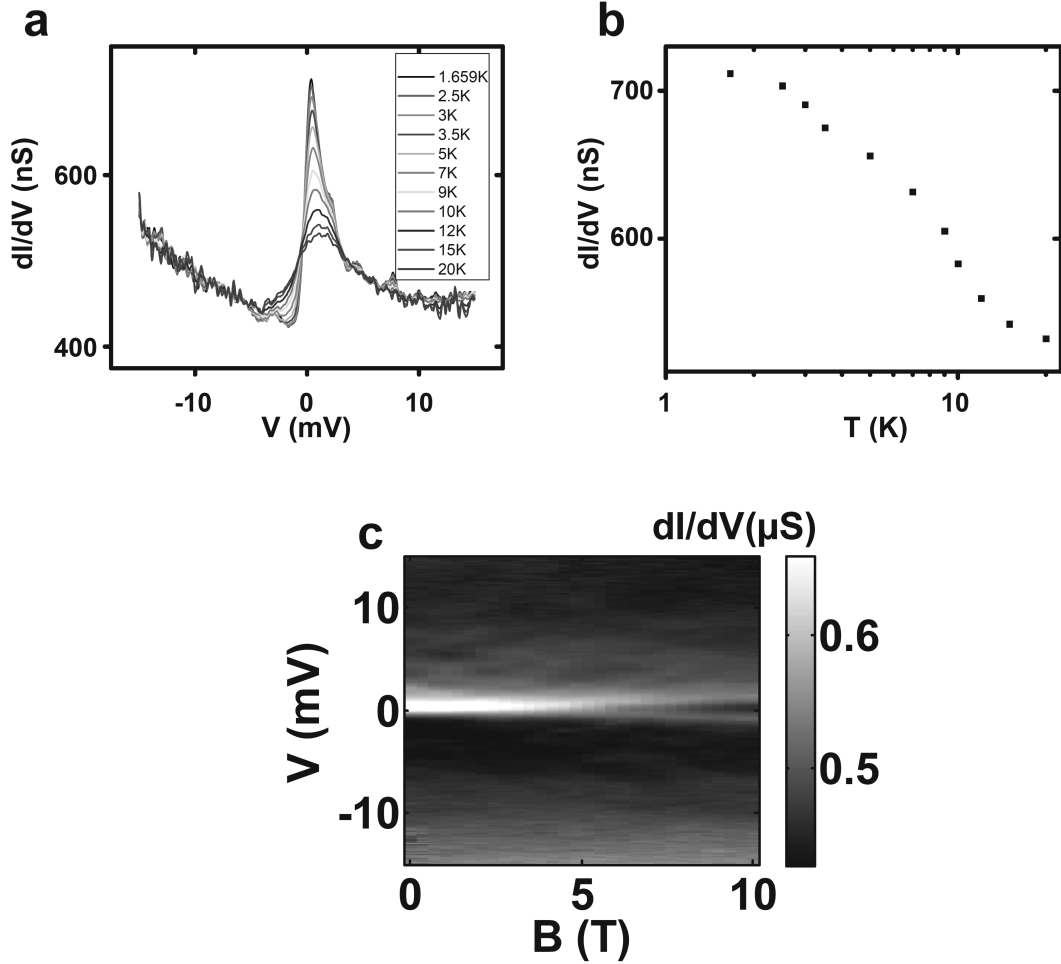


Figure A.9: **a**, dI/dV versus V at fixed gate voltage, inside charge state (1), for various temperatures with $V_G = -2.8$ V. **b**, Zero-bias conductance as a function of temperature. **c**, Grey-scale plot of dI/dV versus V and B at $V_G = -2.8$ V.

In this section we present a detailed study of the zero-bias Kondo resonance observed in charge state (1). We also give clear evidence of the magnetic field splitting of the Kondo resonance in charge state (4). Figures A.9a and A.9b show the temperature dependence of the Kondo resonance observed at the far left of region (1). As expected for an underscreened spin $5/2$ [33, 34], we find a logarithmic increase upon lowering the temperature. In a magnetic field, this Kondo resonance splits in two peaks, as shown in figure A.9c. From the splitting of the Kondo resonance at $B = 10$ T we estimated a g -factor of $g = 1.9 \pm 0.3$.

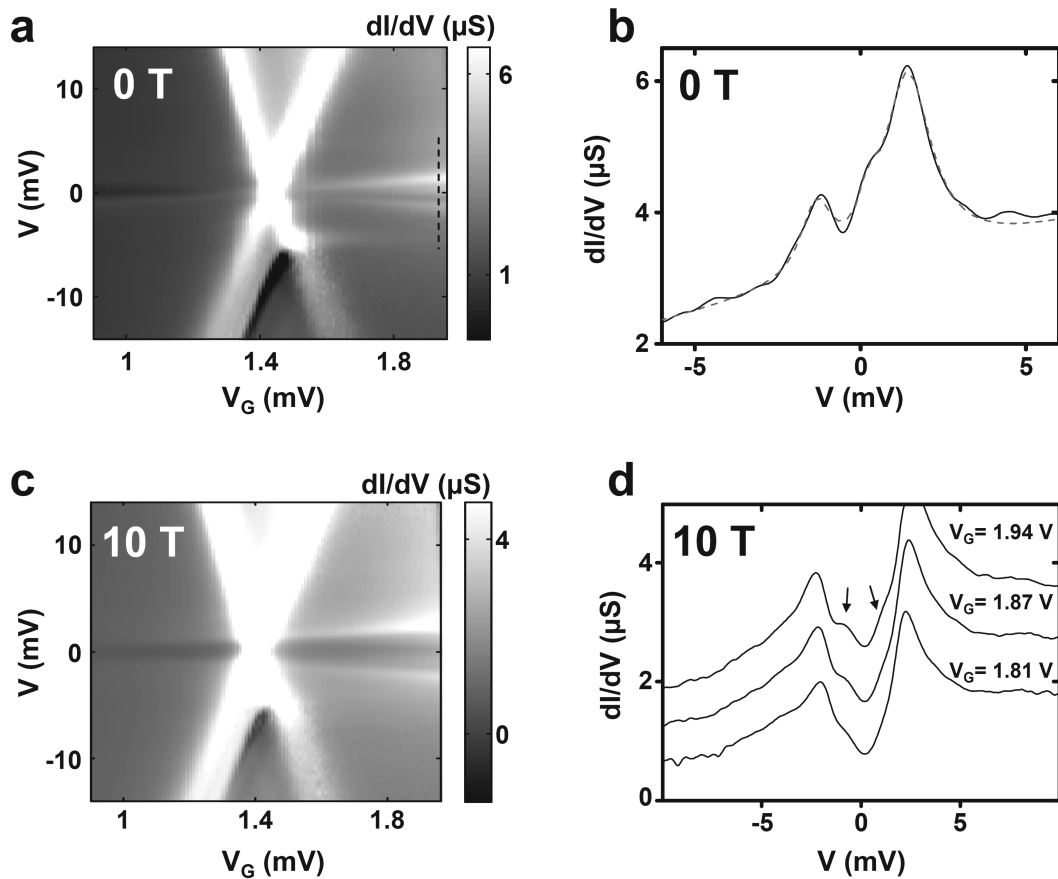


Figure A.10: **a**, Differential conductance map of the crossing between regions (3) and (4), at $T = 1.7$ K and $B = 0$ T. **b**, dI/dV trace taken at the position indicated in **a** by a thin dashed line. Grey dashed line is a fit using three Lorentzian peaks: one was found to be centered around zero bias after convergence of the fitting procedure. **c**, Same as in **a** but at $B = 10$ T. **d**, dI/dV versus V at three different gate voltages inside charge state (4). Arrows indicate the positions of the split zero-bias Kondo resonance for the trace at highest gate voltage.

Due to the close proximity of the gate-dependent cotunneling lines at finite bias, similar plots could not be made to characterize the zero-bias Kondo-resonance in region (4). Nevertheless, it is clear from figures A.10a and A.10b that at zero magnetic field we do observe a zero-bias resonance. The grey dashed line in figure A.10b is a fit to a dI/dV trace taken inside charge state (4); it includes two lorentzians centered at finite bias and a third one which after convergence of the fitting procedure is found to be centered around zero bias. Figure A.10c shows the same stability diagram as in figure A.10a but at high magnetic fields ($B = 10$ T). Three dI/dV traces taken from the former measurement at different gate voltages inside region (4) clearly demonstrate the splitting of the zero-bias Kondo resonance as shown in figure A.10d.

References

- [1] S. Kubatkin, A. Danilov, M. Hjort, J. Cornil, J. L. Bredas, N. Stuhr-Hansen, P. Hedegård, and T. Bjørnholm, “Single-electron transistor of a single organic molecule with access to several redox states,” *Nature*, vol. 425, no. 6959, pp. 698–701, 2003.
- [2] J. B. Neaton, M. S. Hybertsen, and S. G. Louie, “Renormalization of molecular electronic levels at metal-molecule interfaces,” *Phys. Rev. Lett.*, vol. 97, no. 21, p. 216405, 2006.
- [3] S. Yeganeh, M. Galperin, and M. Ratner, “Switching in molecular transport junctions: Polarization response,” *J. Am. Chem. Soc.*, vol. 129, no. 43, pp. 13313–13320, 2007.
- [4] K. Kaasbjerg and K. Flensberg, “Strong polarization-induced reduction of addition energies in single-molecule nanojunctions,” *Nano Lett.*, vol. 8, no. 11, pp. 3809–3814, 2008.
- [5] D. Weinmann, W. Hausler, and B. Kramer, “Spin blockades in linear and nonlinear transport through quantum dots,” *Phys. Rev. Lett.*, vol. 74, no. 6, pp. 984–987, 1995.
- [6] T. Albrecht, K. Moth-Poulsen, J. Christensen, A. Guckian, T. Bjornholm, J. Vos, and J. Ulstrup, “In situ scanning tunnelling spectroscopy of inorganic transition metal complexes,” *Faraday discuss*, vol. 131, pp. 265–279, 2006.
- [7] T. Albrecht, A. Guckian, J. Ulstrup, and J. G. Vos, “Transistor-like behavior of transition metal complexes,” *Nano Lett.*, vol. 5, no. 7, pp. 1451–1455, 2005.
- [8] C. Rajadurai, F. Schramm, S. Brink, O. Fuhr, M. Ghafari, R. Kruk, and M. Ruben, “Spin transition in a chainlike supramolecular iron(II) complex,” *Inorg. Chem.*, vol. 45, no. 25, pp. 10019–10021, 2006.
- [9] L. Bogani and W. Wernsdorfer, “Molecular spintronics using single-molecule magnets,” *Nature Mater.*, vol. 7, no. 3, pp. 179–186, 2008.

- [10] S. Sanvito, “Molecular-spintronics: The art of driving spin through molecules,” *J. Comput. Theor. Nanosci.*, vol. 3, pp. 624–642(19), 2006.
- [11] J. Park, A. N. Pasupathy, J. I. Goldsmith, C. Chang, Y. Yaish, J. R. Petta, M. Rinkoski, J. P. Sethna, H. D. Abruna, P. L. McEuen, and D. C. Ralph, “Coulomb blockade and the Kondo effect in single-atom transistors,” *Nature*, vol. 417, no. 6890, pp. 722–725, 2002.
- [12] M. Ruben, A. Landa, E. Loertscher, H. Riel, M. Mayor, H. Goerls, H. B. Weber, A. Arnold, and F. Evers, “Charge Transport Through a Cardan-Joint Molecule,” *Small*, vol. 4, no. 12, pp. 2229–2235, 2008.
- [13] H. Park, A. K. L. Lim, A. P. Alivisatos, J. Park, and P. L. McEuen, “Fabrication of metallic electrodes with nanometer separation by electromigration,” *Appl. Phys. Lett.*, vol. 75, no. 2, pp. 301–303, 1999.
- [14] D. R. Strachan, D. E. Smith, D. E. Johnston, T.-H. Park, M. J. Therien, D. A. Bonnell, and A. T. Johnson, “Controlled fabrication of nanogaps in ambient environment for molecular electronics,” *Appl. Phys. Lett.*, vol. 86, no. 4, p. 043109, 2005.
- [15] K. O’Neill, E. A. Osorio, and H. S. J. van der Zant, “Self-breaking in planar few-atom Au constrictions for nanometer-spaced electrodes,” *Appl. Phys. Lett.*, vol. 90, no. 13, p. 133109, 2007.
- [16] E. A. Osorio, T. Bjornholm, J.-M. Lehn, M. Ruben, and H. S. J. van der Zant, “Single-molecule transport in three-terminal devices,” *J. Phys.: Condens. Matter.*, vol. 20, no. 37, p. 374121, 2008.
- [17] D. Goldhaber-Gordon, H. Shtrikman, D. Mahalu, D. Abusch-Magder, U. Meirav, and M. A. Kastner, “Kondo effect in a single-electron transistor,” *Nature*, vol. 391, no. 6663, pp. 156–159, 1998.
- [18] S. M. Cronenwett, T. H. Oosterkamp, and L. P. Kouwenhoven, “A Tunable Kondo Effect in Quantum Dots,” *Science*, vol. 281, no. 5376, pp. 540–544, 1998.
- [19] J. Nygård, D. H. Cobden, and P. E. Lindelof, “Kondo physics in carbon nanotubes,” *Nature*, vol. 408, no. 6810, pp. 342–346, 2000.
- [20] S. De Franceschi, S. Sasaki, J. M. Elzerman, W. G. van der Wiel, S. Tarucha, and L. P. Kouwenhoven, “Electron cotunneling in a semiconductor quantum dot,” *Phys. Rev. Lett.*, vol. 86, no. 5, pp. 878–881, 2001.
- [21] J. Paaske, A. Rosch, P. Wolfle, N. Mason, C. M. Marcus, and J. Nygård, “Non-equilibrium singlet-triplet Kondo effect in carbon nanotubes,” *Nat. Phys.*, vol. 2, no. 7, pp. 460–464, 2006.

- [22] A. Kogan, G. Granger, M. A. Kastner, D. Goldhaber-Gordon, and H. Shtrikman, "Singlet-triplet transition in a single-electron transistor at zero magnetic field," *Phys. Rev. B*, vol. 67, no. 11, p. 113309, 2003.
- [23] N. Roch, S. Florens, V. Bouchiat, W. Wernsdorfer, and F. Balestro, "Quantum phase transition in a single-molecule quantum dot," *Nature*, vol. 453, no. 7195, pp. 633–637, 2008.
- [24] A. Borel and C. A. Daul, "Multiplets of free d- and f-metal ions: A systematic DFT study," *Theochem*, vol. 762, no. 1-3, pp. 93–107, 2006.
- [25] M. Brorson and C. E. Schaeffer, "Orthonormal interelectronic repulsion operators in the parametrical dq model. application of the model to gaseous ions," *Inorg. Chem.*, vol. 27, no. 14, pp. 2522–2530, 1988.
- [26] A. B. P. Lever, *Inorganic Electronic Spectroscopy*. 2. ed. Elsevier, Amsterdam, 1984.
- [27] J. Bendix, T. Weyhermuller, E. Bill, and K. Wieghardt, "The mixed-valent (μ -nitrido)dimanganese complex anion $[(\text{CN})(5)\text{Mn-V}(\mu\text{-N})\text{Mn-II}(\text{CN})(5)](6-)$," *Angew. Chem. Int. Ed.*, vol. 38, no. 18, pp. 2766–2768, 1999.
- [28] P. S. Braterman, J. I. Song, and R. D. Peacock, "Electronic absorption spectra of the iron(ii) complexes of 2,2'-bipyridine, 2,2'-bipyrimidine, 1,10-phenanthroline, and 2,2':6',2"-terpyridine and their reduction products," *Inorganic Chemistry*, vol. 31, no. 4, pp. 555–559, 1992.
- [29] R. Schleser, T. Ihn, E. Ruh, K. Ensslin, M. Tews, D. Pfannkuche, D. C. Driscoll, and A. C. Gossard, "Cotunneling-mediated transport through excited states in the Coulomb-blockade regime," *Phys. Rev. Lett.*, vol. 94, no. 20, p. 206805, 2005.
- [30] K. Moth-Poulsen, J. Bendix, P. Hammershøj, and T. Bjørnholm, "Bis[*S*-6-(2,2':6',2"-terpyridin-4'-yloxy)hexyl thioacetate]manganese(II) bis(hexafluorophosphate)," *Acta. Cryst. C.*, vol. 65, no. 1, pp. 14–16, 2009.
- [31] N. P. de Leon, W. Liang, Q. Gu, and H. Park, "Vibrational excitation in single-molecule transistors: Deviation from the simple Franck-Condon prediction," *Nano. Lett.*, vol. 8, no. 9, pp. 2963–2967, 2008.
- [32] V. Körting, *Non-equilibrium electron transport through a double quantum dot system*. Ph.D. thesis, Universität Karlsruhe, 2007.
- [33] V. A. Fateev and P. B. Wiegmann, "Thermodynamics of the $s - d$ exchange model with arbitrary impurity spin (Kondo problem)," *Phys. Rev. Lett.*, vol. 46, no. 24, pp. 1595–1598, 1981.

- [34] F. Mallet, J. Ericsson, D. Mailly, S. Ünlübayir, D. Reuter, A. Melnikov, A. D. Wieck, T. Micklitz, A. Rosch, T. A. Costi, L. Saminadayar, and C. Bäuerle, “Scaling of the low-temperature dephasing rate in Kondo systems,” *Phys. Rev. Lett.*, vol. 97, no. 22, p. 226804, 2006.

Chapter 6

Switching in molecular junctions containing a Co-based grid molecule

E. A. Osorio, M. Ruben, J. M. Lehn, and H. S. J. van der Zant

We report on three-terminal transport through electromigrated junctions containing a Co-based grid molecule. The molecule comprises a ligand-mediated arrangement of four metal Co(II)-ions positioned at the conerstones of a molecular square. Three-terminal transport measurements show Coulomb blockade and excitation lines at low energy which are attributed to vibrational modes of the molecule. When applying a bias above a threshold voltage, we find switching in the I-V characteristic; below this voltage, it is absent. Similar switching behavior occurs as a function of gate voltage. The measurements show that conformational changes are most likely not the cause of the switches. A possible mechanism may be related to the motion of counter ions in the vicinity of the molecular junction.

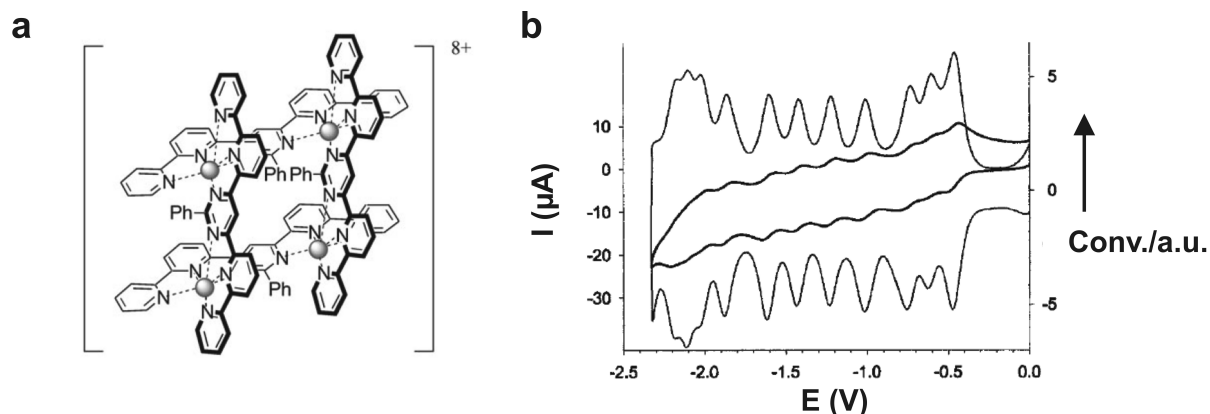


Figure 6.1: **a**, Representation of the $[\text{Co}_4^{\text{II}} \text{L}_4]^{8+}$ complex ($\text{L}=4,6\text{-bis}(2,2\text{-bipyrid-6-yl})\text{-2-phenylpyrimidine}$). Each Co^{II} center is coordinated by six N donor atoms (dotted lines). **b**, Cyclic voltammogram (bold: scan rate 0.1 V/s) and its semiderivative deconvolution (thin) of $[\text{Co}_4^{\text{II}} \text{L}_4]^{8+}$ in DMF 0.1M + Bu_4NPF_6 . Pictures **a** and **b** are taken from Ref. [18]

6.1 Introduction

Molecules are attractive building blocks for performing logical operations in high-density electronic devices. The observation of electrical switching in molecular junctions has therefore attracted a lot of attention. Very recently the operation of a 160-kilobit dynamic random access memory (DRAM) circuit based on monolayers of bistable rotaxane molecules as data storage elements has been demonstrated [1]. Reports on conductance switching in the literature, however, remain controversial with regard to the nature of the mechanism itself: conformational changes [2–6], molecule-bond fluctuations [7, 8], or reversible formation of metallic filaments through molecular layers [9] are among the proposed mechanisms. In some cases the switching appears to be voltage driven: a dc bias voltage triggers a transition to a higher conductance state [3–5, 10, 11]. Other experiments with photochromic molecules demonstrate that light-controlled switching [12–16] is possible through well-characterized photoisomerizations as shown in recent measurements carried out on large-area contacts [17].

6.2 Experiment details

In this chapter we present measurements performed on three-terminal devices incorporating the $[\text{Co}_4^{\text{II}} \text{L}_4]^{8+}$ $[2 \times 2]$ -grid complex (see figure 6.1). It is a special type of molecule giving rise to up to twelve well-resolved reduction waves in cyclic voltammetry studies, indicating that up to 12 electrons can be put onto the molecule; this represents the highest reported number of well-characterized, resolved and reversible one-electron reductions on a molecular compound [18]. For example, the fullerenes (C_{60}) exhibit only four reversible single-electron reductions for a similar voltage span as in figure 6.1b [19]. This exceptional

property of the grid molecule makes it an interesting candidate for measurements in three-terminal devices since one would expect that the number of accessible charge states would be higher with this molecule compared to the other molecules used in the work presented in this thesis. Although we did not observe such an increase in the number of charge states probed in the experiments, clear vibrational spectra were recorded as well as, more interestingly, the presence of switching behavior. Out of a total of 100 junctions that were measured, two showed both of these features (samples A and B). On a third sample, which we name C, we did not observe switching behavior but a set of excitations at comparable energies with samples A and B.

6.3 Results and discussions

6.3.1 Vibrational excitations

Transport measurements for samples A and B are represented in figure 6.2a and b respectively as a plot of the differential conductance as a function of bias and gate voltage. Regions of high conductance (white and grey) where transport takes place through sequential electron tunneling (SET) are markedly separated by slanted lines (diamond edges) from regions of zero conductance (black), which is a signature of Coulomb blockade physics. For samples A and B, only two charge states are probed in the experiment which we label N and $N+1$. We observe in both transport measurements sharp spectroscopic features, i.e., excitation lines, in the SET region indicating a weak (electronic) molecule-lead coupling. The energies of these excitations are listed in panel d (figure 6.2) for samples A and B for the two consecutive charge states; for energies above 10 meV, other sets of measurements, not shown here, were used for determining these. We have also included the energy of the excitations for sample C which also displayed only two charge states. From the table in panel d, it appears that the three samples share common excitation energies. The fact that some excitations are absent (present) for one sample and not for the other may hint in a difference of the environment for the three molecules or different molecule-lead couplings [20].

It is important to remark that given the energy spacing of the excitations (few meV) and their appearance at approximately the same energies for two subsequent charge states, we argue in the same way as for the OPV-5 (see chapter 3) that the observed excitations originate from vibrational modes. Further confirmation comes from the observation of four harmonic excitation lines indicated in figure 6.2a by arrows; in figure 6.2c we have plotted the energy of these four excitations as a function of the mode number and in 6.1e the corresponding current-voltage characteristics. Such a harmonic spectrum indicates the excitation of four vibrational quanta and suggest a value of the electron-phonon coupling of order one [21] (see section 2.1.3 in chapter 2). From the step heights in figure 6.2e, an estimate of the $e-ph$ coupling constant, λ , can be obtained. In the approximation that transitions involve at least one ground state, one finds that the ratio between the second and first step height equals λ [21, 22]. In figure 6.2e this ratio is close to one for all three

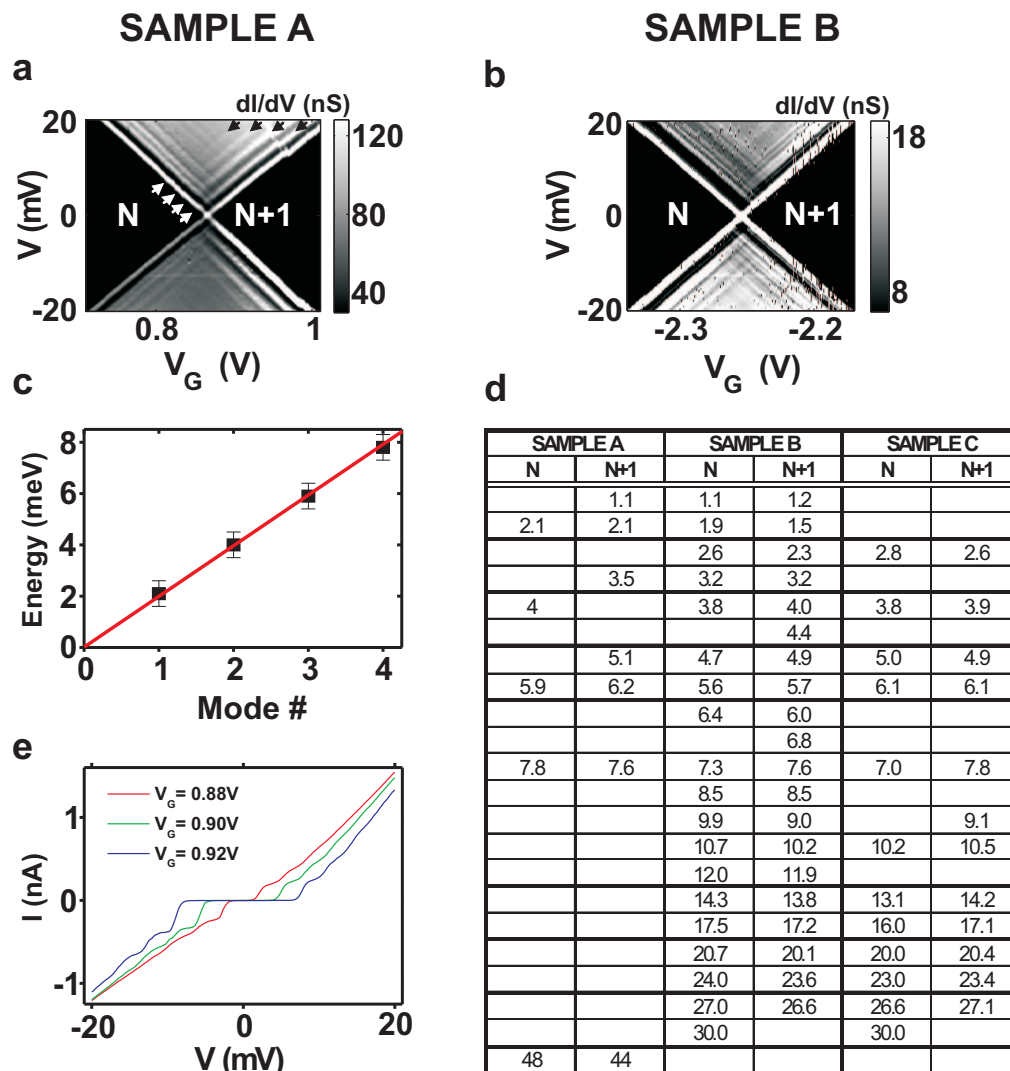


Figure 6.2: **a, b**, Conductance maps of two different junctions (samples A and B) incorporating a grid-type complex in the weak coupling limit measured at 1.6 K, and with a maximum applied bias voltage of ± 20 mV. **c**, Energy of the first four vibrational excitation in charge state N as a function of the mode number (sample A). **d**, Energy of the excitations lines listed for the two consecutive charge states probed in the experiment (for samples A, B, and C). These are read from the bias at which the excitation line meets the diamond edge; the excitation corresponds to the charge state of the Coulomb diamond they end up in. The error in the reading is about 0.5 meV. **e**, I - V characteristics at three different gate voltages from the measurement in **a** showing the step-wise increase of the current due to the excitation of the n -th vibrational mode (squares in **c**).

curves; thus the data indicates $\lambda \approx 1$. To get more insight in the nature of the vibrational modes and their appearance in an experiment, quantum chemistry calculations would be helpful. However at low energies the calculations are very sensitive to the local environment (potential landscape) and this may make it difficult to identify the exact mode that appears in the experiment.

6.3.2 Switching

We now turn to transport measurements in sample A carried out on a larger bias and V_{gate} range. In figure 6.3a we show the conductance map acquired with a maximum applied bias of ± 200 mV. A striking difference with figure 6.2a is observed: the stability diagram no longer shows a clearly defined degeneracy point at approximately $V_G=0.8$ V. Diamond edges are ill-defined as the onset of conductance appears to be stochastically distributed (switching behavior) for every gate voltage. In addition, a pronounced negative differential resistance (NDR) region (black) appears at positive bias. Figure 6.3b shows an expanded view on the central region of the stability diagram which shows the switching behavior in more detail. As a guide and for the purpose of the upcoming discussions, we have added blue and red dashed lines in figure 6.3b which represent a lower-bias bound for the onset of conductance.

In order to study in more detail this stochastic behavior we continuously measured I - V characteristics at $V_G=1$ V from -200 mV to $+200$ mV and back. We acquired 200 of these sweeps, and in figure 6.3c we have plotted three different types of I - V curves which are representative of the overall behavior during these measurements; we have labeled these with numbers. A common feature of all three types of I - V curves is the broad NDR located at positive bias. Apart from having slightly different current levels, the three type of I - V s display a different Coulomb gap size: the red (green) I - V is the one with the smallest (largest) gap in figure 6.3c. We also note that the green I - V curve has a less sharp onset of conductance as compared to the blue I - V curve: this is more clear at negative bias. It is important to note that during the 200 sweeps, stochastic switching between the different I - V curves is observed for biases higher than ± 80 mV. This is marked by vertical transitions in the I - V characteristic as the ones observed in figure 6.3c at approximately -200 mV in bias.

By decreasing the maximum applied bias in the sweeps, we find that it has a profound influence on the switching. In figure 6.3d we show two representative I - V characteristics in which the bias voltage of the sweeps was limited to ± 120 mV. Compared to the previous measurement in which the bias was limited to ± 200 mV, we did not observe in a total of 200 sweeps the green type of I - V characteristic as shown in figure 6.3c; all recorded I - V curves were similar to the ones in figure 6.3d. We also note that stochastic switching between I - V types is observed, and in figure 6.3d we see a clear transition from the red to the blue type of curve at approximately -80 mV. Below a threshold bias voltage in the sweeps, $V \approx 100$ mV, the switching between different types of I - V curves completely disappears. In figure 6.3e we show 20 out of 200 consecutive sweeps performed with a maximum applied voltage of ± 100 mV. It is clear that only the blue type of I - V characteristic remains.

SAMPLE A

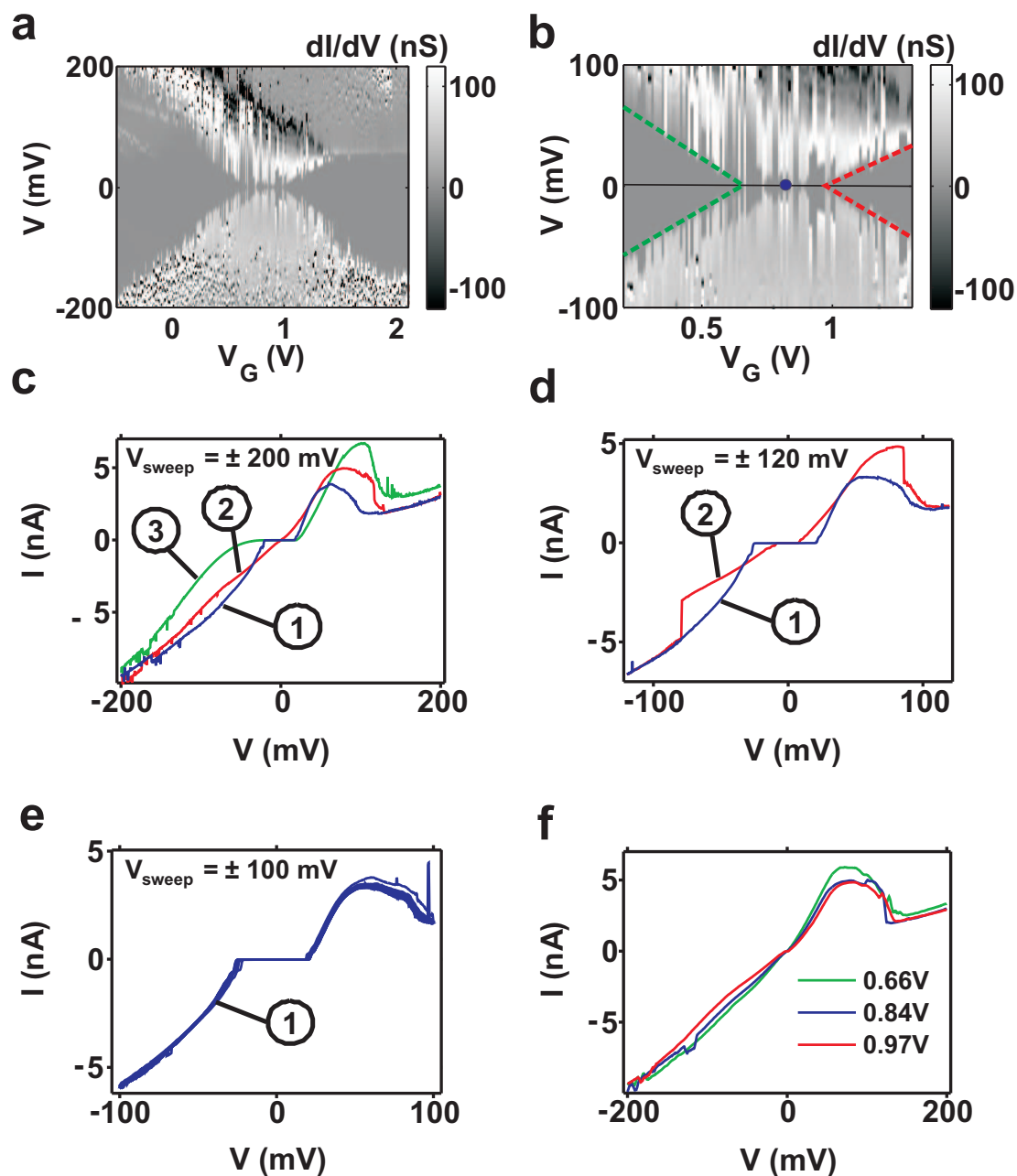


Figure 6.3: **a**, Conductance map of sample A measured at 1.6 K, and with a maximum applied bias of ± 200 mV. **b**, Zoom-in of the central region in the stability diagram shown in **a**. **c**, **d**, **e**, Recorded I - V curves taken by sweeping the bias voltage back and forth continuously between ± 200 mV, ± 120 mV, and ± 100 mV at $V_G = 1$ V. For clarity, a limited number of curves is shown in each panel; numbers label each type of characteristic I - V (see text). **f**, I - V curves taken from **a** at $V_G = 0.66$ V, 0.84 V, and 0.97 V. Note that an I - V characteristic in a conductance map is recorded at a fix gate voltage but also at a particular time; this means that I - V characteristics measured at the previous gate voltages as a function of time would have also displayed the same switching behavior as in **c**.

The stability of the I - V characteristic below this voltage explains why in figure 6.2a, where the applied bias did not exceed 20 mV, well defined diamond edges are observed. In addition, the position in gate voltage of the charge degeneracy point in figure 6.2a coincides with the position of the blue dot in figure 6.3b. Surprisingly, figure 6.3b shows that the conductance at the zero-bias axis appears enhanced (white) for different gate voltages. At the charge degeneracy point it is expected that the conductance gap in the I - V characteristic vanishes. Therefore, this finding suggest that the charge degeneracy point in the measurement presented in figure 6.3b shifts between different fixed positions at the gate axis. To illustrate this point, we present in figure 6.3f I - V characteristics at three different gate voltages: at the crossing of the green (red) dashed lines, and at the position of the blue dot in figure 6.3b. We see that all three curves are similar and share the absence of a clear conductance gap, confirming our observations.

We have observed a similar switching effect for sample B. Figure 6.4a shows the conductance map, and just like for sample A we see that well defined diamond edges are absent as the onset for conductance is no longer linear on V_G (see figure 6.4b). With dashed red and green lines we highlight in figure 6.4a two possible onsets for conductance which are connected to two different charge degeneracy points of the same state (the crossing point of the green and red dashed lines define these two points).

In the same manner as for sample A we have measured at a fixed gate voltage I - V characteristics from -200 mV to +200 mV and back. By measuring continuously 300 of these sweeps, we found that two representative types of different I - V characteristic appear, which are plotted in figure 6.4b. We note that in figure 6.4b the red type of I - V curve switches at positive and negative bias voltages (indicated by arrows) to the green type I - V curve. In figure 6.4c we have plotted 100 consecutive sweeps. We observe a frequent stochastic switching between the two different types of I - V curves. The current levels are practically the same for all sweeps and the main difference between the two types of I - V curves is the conductance gap size: it is smaller for the green type of I - V s. The size of the conductance gap for the red (green) type I - V curves is equal to the gap size one would determine from the red (green) diamond edges schematically drawn in figure 6.4a with dashed lines. As with sample A, below a certain threshold bias voltage (about 50 mV in this case), sample B stops displaying switching between different types of I - V curves. In figure 6.4d we show 20 out of 300 consecutive sweeps with a maximum applied bias voltage of 50 mV: only the green type of I - V curve is recorded. For the measurement presented in figure 6.2b the bias was kept below this threshold value. We note that the crossing defined by the green dashed lines in figure 6.4a is located at the same gate voltage as the degeneracy point in figure 6.2b.

Before we turn to possible explanations for the switching effect observed in samples A and B, we mention that a similar type of switching was observed in measurements carried out on the manganese complex discussed in chapter 5. A summary of the results displaying switching behavior in this complex can be found in the appendix attached to this chapter. Based on the observations, we can disregard certain mechanisms that may induce the switching behavior. First of all, molecule-Au bond fluctuations cannot explain the observed switching since, unlike the manganese complex, the grid molecule does not

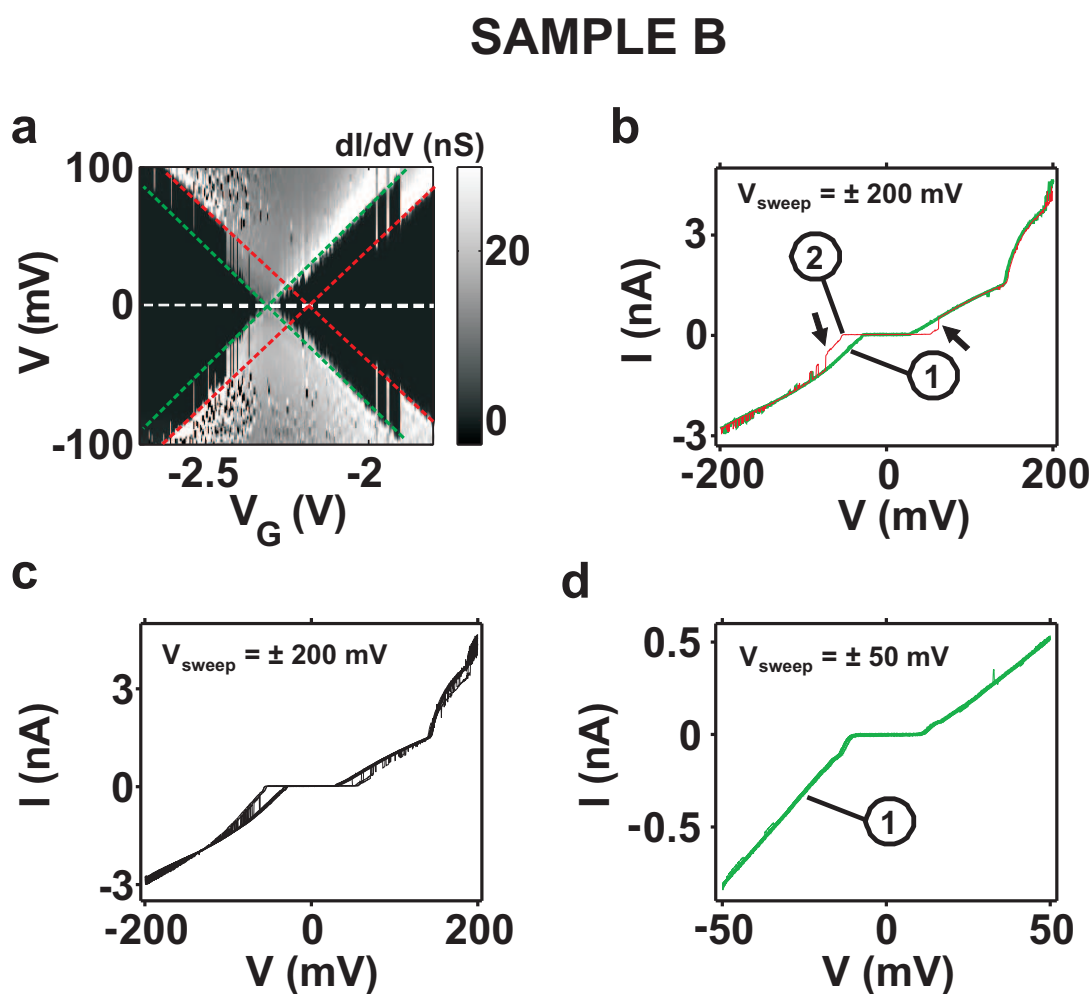


Figure 6.4: **a**, Conductance map of sample B measured at 1.6 K, and with a maximum applied bias of ± 200 mV; **b**, **c**, Recorded $I-V$ curves taken by sweeping the bias voltage back and forth continuously between ± 200 mV at $V_G = -2.4$ V. In **b** (**c**) 2 (100) $I-V$ curves are shown. Arrows in **b** point at a transition between characteristic $I-V$ s (see text). **d** Same as **c** but for a limiting bias of ± 50 mV. A total of 20 sweeps is displayed.

posses binding groups (such as S-H). Moreover, conformational changes are not the cause as they are only expected to change the I - V characteristic above a certain bias voltage and not the conductance gap. Claims of the observation of conformational changes have been reported with scanning tunneling microscopy (STM) experiments. In these experiments the zero-bias resistance and the low-bias behavior remained unchanged [4, 5].

The fact that the measurements indicate that the charge degeneracy point is stochastically shifting suggests that the switching effect is rather electrostatic in nature. Charges near the molecular junctions might be the cause. The grid complex and the manganese complex are both molecules with an intrinsic charge; plus eight and plus two respectively. Neighboring molecules which do not contribute to transport could have an electrostatic influence on the conducting molecule. Furthermore, the solutions which are used for the deposition of these molecules contain counter ions (molecular species that ensure charge neutrality of the whole compound). After deposition these counter ions may remain in the vicinity of the junction area; by moving around they mimic a change in the offset charge which leads to a shift of the degeneracy point. It is important to note that we never observed a similar switching behavior in the measurements carried out on the OPV molecules. These molecules are neutral and therefore do not require the presence of counterions. In order to fully elucidate the fundamental process underlying the switching mechanism further experimental and theoretical research is however required.

Appendix

In this appendix, we show measurements performed on three-terminal devices incorporating the Mn-based transition metal complex discussed in chapter 5 of this thesis. In 2 samples out of 206, a similar type of switching behavior as the one mentioned in this chapter for junctions incorporating a grid type complex is observed. We summarize below the main results.

A.1 Switching in a single-Mn atom molecular complex

Figures A.1a and b show the conductance maps of two different junctions. As in other measurements described in this thesis we observe regions of high conductance where transport is dominated by sequential electron tunneling (SET) and regions of low conductance where transport is blocked. In figure A.1a we observe a single charge degeneracy point and slanted lines (diamond edges) which separate the two conductance regions. On the positive gate voltage region of this plot we observe “oscillations” on the onset of conductance (switching). Similar observations have been made in a second sample; the results are shown in figure A.1b. Switches occur at the right hand side of the degeneracy point indicated by a black dot. Furthermore, we see that the lower-bias bound for the onset of conductance follows a linear gate dependence (dashed-black line in figure A.1b). This

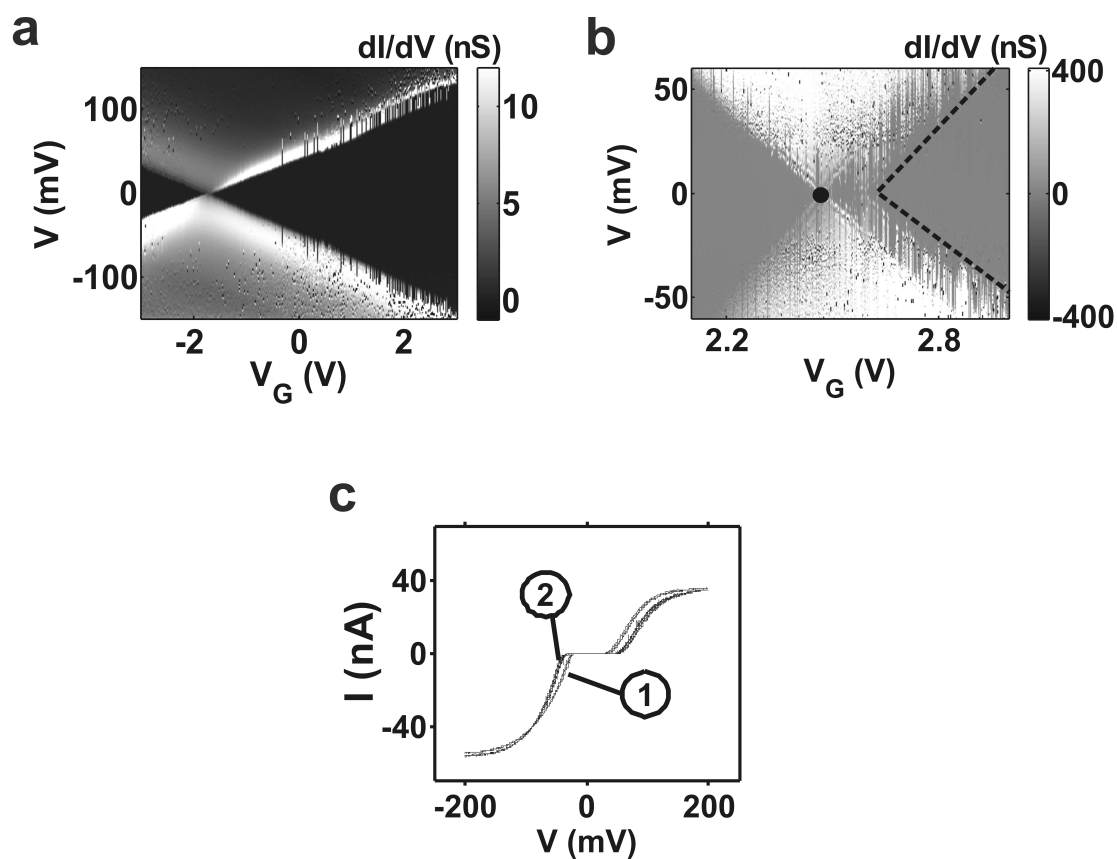


Figure A.1: **a**, **b**, Stability diagrams for two different $([\text{Mn}(\text{terpy-O}-(\text{CH}_2)_6\text{-SAc})_2]^{2+})$ molecular junctions, measured at 1.6 K. **c**, Recorded $I-V$ curves from **b** taken by sweeping the bias voltage continuously back and forth between ± 200 mV at $V_G = 2.7$ V. A total number of 30 consecutive sweeps are shown.

indicates that the diamond edge is shifting (stochastically) by a fixed amount along the gate axis, owing to the presence of a variable offset charge. In figure A.1c we show I - V characteristics that were recorded by sweeping continuously the bias voltage back and forth between $V = \pm 200$ mV at $V_G = 2.7$ V on the sample from figure A.1b. The I - V curves fall mainly into two categories: type 1 I - V 's have a smaller Coulomb blockade gap and slightly higher (smaller) current levels at positive (negative) bias than type 2 I - V 's. Qualitatively the switching behavior in these pictures resemble the one presented in the measurements discussed in chapter 6. However, we did not observe as in chapter 6 a bias dependence of the switching nor a threshold bias voltage at which this effect disappears.

References

- [1] J. E. Green, J. Wook Choi, A. Boukai, Y. Bunimovich, E. Johnston-Halperin, E. DeIonno, Y. Luo, B. A. Sheriff, K. Xu, Y. Shik Shin, H. R. Tseng, J. F. Stoddart, and J. R. Heath, "A 160-kilobit molecular electronic memory patterned at 1011 bits per square centimetre," *Nature*, vol. 445, no. 7126, pp. 414–417, 2007.
- [2] J. Gaudioso, L. J. Lauhon, and W. Ho, "Vibrationally mediated negative differential resistance in a single molecule," *Phys. Rev. Lett.*, vol. 85, no. 9, pp. 1918–1921, 2000.
- [3] E. Lortscher, J. Ciszek, J. Tour, and H. Riel, "Reversible and controllable switching of a single-molecule junction," *Small*, vol. 2, no. 8-9, pp. 973–977, 2006.
- [4] B.-Y. Choi, S.-J. Kahng, S. Kim, H. Kim, H. W. Kim, Y. J. Song, J. Ihm, and Y. Kuk, "Conformational molecular switch of the azobenzene molecule: A scanning tunneling microscopy study," *Phys. Rev. Lett.*, vol. 96, no. 15, p. 156106, 2006.
- [5] X. H. Qiu, G. V. Nazin, and W. Ho, "Mechanisms of reversible conformational transitions in a single molecule," *Phys. Rev. Lett.*, vol. 93, no. 19, p. 196806, 2004.
- [6] A. V. Danilov, P. Hedegård, D. S. Golubev, T. Bjørnholm, and S. E. Kubatkin, "Nanoelectromechanical switch operating by tunneling of an entire C_{60} molecule," *Nano Lett.*, vol. 8, no. 8, pp. 2393–2398, 2008.
- [7] G. K. Ramachandran, T. J. Hopson, A. M. Rawlett, L. A. Nagahara, A. Primak, and S. M. Lindsay, "A bond-fluctuation mechanism for stochastic switching in wired molecules," *Science*, vol. 300, no. 5624, pp. 1413–1416, 2003.
- [8] A. V. Danilov, S. E. Kubatkin, S. G. Kafanov, K. Flensberg, and T. Bjørnholm, "Electron transfer dynamics of bistable single-molecule junctions," *Nano Lett.*, vol. 6, no. 10, pp. 2184–2190, 2006.
- [9] C. N. Lau, D. R. Stewart, R. S. Williams, and M. Bockrath, "Direct observation of nanoscale switching centers in metal/molecule/metal structures," *Nano Lett.*, vol. 4, no. 4, pp. 569–572, 2004.

- [10] K. Seo, A. V. Konchenko, J. Lee, G. S. Bang, and H. Lee, "Molecular conductance switch-on of single ruthenium complex molecules," *J. Am. Chem. Soc.*, vol. 130, no. 8, pp. 2553–2559, 2008.
- [11] A. S. Blum, J. G. Kushmerick, D. P. Long, C. H. Patterson, J. C. Yang, J. C. Henderson, Y. Yao, J. M. Tour, R. Shashidhar, and B. R. Ratna, "Molecularly inherent voltage-controlled conductance switching," *Nat Mater*, vol. 4, no. 2, pp. 167–172, 2005.
- [12] A. S. Kumar, T. Ye, T. Takami, B. C. Yu, A. K. Flatt, J. M. Tour, and P. S. Weiss, "Reversible photo-switching of single azobenzene molecules in controlled nanoscale environments," *Nano Lett.*, vol. 8, no. 6, pp. 1644–1648, 2008.
- [13] J. M. Mativetsky, G. Pace, M. Elbing, M. A. Rampi, M. Mayor, and P. Samor, "Azobenzenes as light-controlled molecular electronic switches in nanoscale metal-molecule-metal junctions," *J. Am. Chem. Soc.*, vol. 130, no. 29, pp. 9192–9193, 2008.
- [14] M. J. Comstock, N. Levy, A. Kirakosian, J. Cho, F. Lauterwasser, J. H. Harvey, D. A. Strubbe, J. M. J. Frechet, D. Trauner, S. G. Louie, and M. F. Crommie, "Reversible photomechanical switching of individual engineered molecules at a metallic surface," *Phys. Rev. Lett.*, vol. 99, no. 3, p. 038301, 2007.
- [15] A. C. Whalley, M. L. Steigerwald, X. Guo, and C. Nuckolls, "Reversible switching in molecular electronic devices," *J. Am. Chem. Soc.*, vol. 129, no. 42, pp. 12590–12591, 2007.
- [16] D. Dulić, S. J. van der Molen, T. Kudernac, H. T. Jonkman, J. J. D. de Jong, T. N. Bowden, J. van Esch, B. L. Feringa, and B. J. van Wees, "One-way optoelectronic switching of photochromic molecules on gold," *Phys. Rev. Lett.*, vol. 91, no. 20, p. 207402, 2003.
- [17] A. J. Kronemeijer, H. B. Akkerman, T. Kudernac, B. J. van Wees, B. L. Feringa, P. W. M. Blom, and B. de Boer, "Reversible conductance switching in molecular devices," *Adv. Mater.*, vol. 20, no. 8, pp. 1467–1473, 2008.
- [18] M. Ruben, E. Breuning, M. Barboiu, J. P. Gisselbrecht, and J. M. Lehn, "Functional supramolecular devices: $[M_4^{II}L_4]^{+8}[2 \times 2]$ -grid type complexes as multilevel molecular electronic species," *Chem. Eur. J.*, vol. 9, no. 1, pp. 291–299, 2003.
- [19] L. Echegoyen and L. E. Echegoyen, "Electrochemistry of fullerenes and their derivatives," *Acc. Chem. Res.*, vol. 31, no. 9, pp. 593–601, 1998.
- [20] N. P. de Leon, W. Liang, Q. Gu, and H. Park, "Vibrational excitation in single-molecule transistors: Deviation from the simple Franck-Condon prediction," *Nano Lett.*, vol. 8, no. 9, pp. 2963–2967, 2008.

-
- [21] H. Park, J. Park, A. K. L. Lim, E. H. Anderson, A. P. Alivisatos, and P. L. McEuen, “Nanomechanical oscillations in a single- C_{60} transistor,” *Nature*, vol. 407, no. 6800, pp. 57–60, 2000.
- [22] S. Braig and K. Flensberg, “Vibrational sidebands and dissipative tunneling in molecular transistors,” *Phys. Rev. B*, vol. 68, no. 20, p. 205324, 2003.

Chapter 7

Three-terminal transport through two capacitively coupled dots in parallel: comparison to experiment

J. S. Seldenthuis, E. A. Osorio, J. M. Thijssen and H. S. J. van der Zant.

7.1 Introduction

One of the main questions in single-molecule electronics is to know whether a single molecule is addressed during the electrical measurements. Neighboring molecules of the same or of a different kind (e.g., contamination) can affect the transport measurements masking the transport properties of a single molecule. So far the only technique which allows the experimentalist to address a single molecule and to be able to characterize the environment of that molecule is scanning tunneling microscopy (STM). On the other hand, in electromigrated junctions, the final sample geometry, i.e., the number of molecules in the gap and their arrangement, the presence of spurious metallic clusters, is not under experimental control. In the work presented in this thesis electrical measurements at cryogenic temperatures are used to unravel the sample topology. In some cases, “the picture” is very clear as in figure 3.3 of chapter 3, and in some others the conductance map is more complicated and features which may indicate the presence of more than one dot (or charge traps) are observed [1, 2]. These observations motivated the work presented in this chapter in which we make use of a simple model to numerically calculate some of the observed features which cannot be understood in a single-dot framework. The model makes use of the rate equation approach [3] applied to two capacitively coupled parallel dots.

The parallel double-quantum dot (DQD) is a system that has been used for studying interference, such as in Aharonov-Bohm (AB) type interferometers [4, 5], as well as phenomena in the Coulomb blockade [6] and Kondo regimes [7]. Much theoretical work has been devoted to the Kondo effect in parallel DQD structures [8–11] where, in contrast to our model, tunneling between the dots is taken into account. Here, we will only consider capacitive coupling between the two dots following experimental work [12–14] and theoretical work [15, 16] by others. On what follows, equations for the electrostatic interaction between the dots and the tunneling rates to and from the leads will be derived. At the end of this chapter we present results based on the non-equilibrium Green’s function (NEGF) formalism to account for the line shapes of the observed features.

7.2 Parallel double-dot system

The double dot is modeled as a network of tunnel resistors and capacitors as illustrated in figure 7.1. The number of electrons on dot 1(2) is $N_{1(2)}$. Each dot is capacitively coupled to a gate voltage V_G through a capacitor $C_{g1(2)}$ and to the source (drain) leads through a tunnel barrier represented by a tunnel resistor $R_{L1(2)}$ ($R_{R1(2)}$) and a capacitor $C_{L1(2)}$ ($C_{R1(2)}$) connected in parallel. The dots are coupled to each other by a capacitor C_m . Within this model we make the following assumptions: (i) There is no tunneling between the two dots, i.e., only capacitive coupling is considered. (ii) Transport through each dot is carried by a single (non-spin-degenerate) particle energy level.

Following the same approach as in ref. [17], the electrostatic energy for the network presented in figure 7.1 reads:

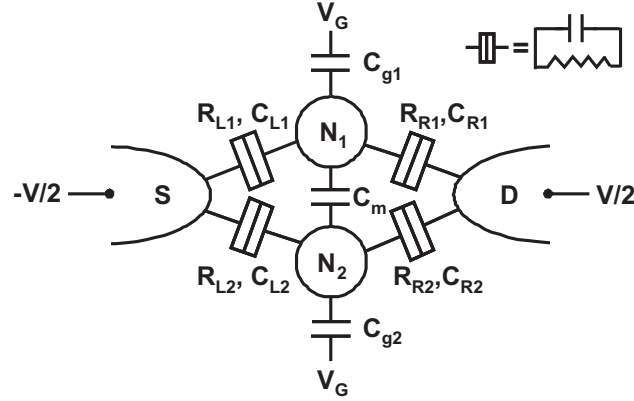


Figure 7.1: Two quantum dots coupled in parallel by tunnel junctions (see inset) to common source and drain electrodes, capacitively to a common gate electrode, and to each other by a mutual capacitance C_m .

$$U(N_1, N_2) = \frac{1}{2}N_1^2 E_{C1} + \frac{1}{2}N_2^2 E_{C2} + N_1 N_2 E_{Cm} + f(V, V_G), \quad (7.1)$$

with

$$\begin{aligned} f(V, V_G) = & \frac{V_G}{-|e|} (C_{g1}(N_1 E_{C1} + N_2 E_{Cm}) \\ & + C_{g2}(N_1 E_{Cm} + N_2 E_{C2})) \\ & + \frac{V_G^2}{-2|e|^2} (C_{g1}^2 E_{C1} + C_{g2}^2 E_{C2} + 2C_{g1}C_{g2} E_{Cm}) \\ & + \frac{V}{-2|e|} ((C_{R1} - C_{L1})(N_1 E_{C1} + N_2 E_{Cm}) \\ & + (C_{R2} - C_{L2})(N_1 E_{Cm} + N_2 E_{C2})) \\ & + \frac{V^2}{-8|e|^2} ((C_{R1} - C_{L1})^2 E_{C1} + (C_{R2} - C_{L2})^2 E_{C2} \\ & + 2(C_{R1} - C_{L1})(C_{R2} - C_{L2}) E_{Cm}), \end{aligned}$$

where $E_{C1(2)}$ is the charging energy of the individual dot 1(2), E_{Cm} is the electrostatic capacitive coupling energy, and $-|e|$ is the electron charge. The energy E_{Cm} is the change in energy of one dot when an electron is added to the other dot. These energies can be written as follows :

$$\begin{aligned}
 E_{C1} &= \frac{e^2}{C_1} \left(\frac{1}{1 - \frac{C_m^2}{C_1 C_2}} \right), \\
 E_{C2} &= \frac{e^2}{C_2} \left(\frac{1}{1 - \frac{C_m^2}{C_1 C_2}} \right), \\
 E_{Cm} &= \frac{e^2}{C_m} \left(\frac{1}{\frac{C_1 C_2}{C_m^2} - 1} \right),
 \end{aligned}$$

where $C_{1(2)} = C_{L1(2)} + C_{R1(2)} + C_{g1(2)} + C_m$.

The electrochemical potential $\mu_{1(2)}(N_1, N_2)$ of dot 1(2) is defined as the energy needed to add the $N_{1(2)}$ -th electron to dot 1(2). Using the expression for the total energy Eq. 7.1, the electrochemical potentials of the two dots are:

$$\begin{aligned}
 \mu_1(N_1, N_2) &= U(N_1, N_2) - U(N_1 - 1, N_2) \\
 &= (N_1 - \frac{1}{2})E_{C1} + N_2 E_{Cm} \\
 &\quad - \frac{V_G}{|e|} (C_{g1} E_{C1} + C_{g2} E_{Cm}) \\
 &\quad - \frac{V}{2|e|} ((C_{R1} - C_{L1})E_{C1} + (C_{R2} - C_{L2})E_{Cm}),
 \end{aligned}$$

$$\begin{aligned}
 \mu_2(N_1, N_2) &= U(N_1, N_2) - U(N_1, N_2 - 1) \\
 &= (N_2 - \frac{1}{2})E_{C2} + N_1 E_{Cm} \\
 &\quad - \frac{V_G}{|e|} (C_{g1} E_{Cm} + C_{g2} E_{C2}) \\
 &\quad - \frac{V}{2|e|} ((C_{R1} - C_{L1})E_{Cm} + (C_{R2} - C_{L2})E_{C2}).
 \end{aligned}$$

If initially the two dots are empty ($N_1 = 0, N_2 = 0$), and we add an electron to the first dot ($N_1 = 1, N_2 = 0$) or to the second dot ($N_1 = 0, N_2 = 1$), the chemical potentials for these processes are respectively:

$$\begin{aligned}
 \tilde{\mu}_1 &= \epsilon_1 - e\alpha_1 V - e\beta_1 V_G, \\
 \tilde{\mu}_2 &= \epsilon_2 - e\alpha_2 V - e\beta_2 V_G,
 \end{aligned}$$

where we have defined $\epsilon_1 = E_{C1}/2$, $\epsilon_2 = E_{C2}/2$, the bias couplings as

$$\begin{aligned}\alpha_1 &= \frac{1}{2} \frac{(C_{R1} - C_{L1})C_2 + (C_{R2} - C_{L2})C_m}{C_1C_2 - C_m^2}, \\ \alpha_2 &= \frac{1}{2} \frac{(C_{R2} - C_{L2})C_1 + (C_{R1} - C_{L1})C_m}{C_1C_2 - C_m^2},\end{aligned}$$

and the gate couplings as

$$\begin{aligned}\beta_1 &= \frac{C_{g1}C_2 + C_{g2}C_m}{C_1C_2 - C_m^2}, \\ \beta_2 &= \frac{C_{g2}C_1 + C_{g1}C_m}{C_1C_2 - C_m^2}.\end{aligned}$$

The bias and gate couplings for each dot can be determined from the slopes of the diamond edges. We will note $\delta+$ and $\delta-$, the positive and negative slopes respectively. With these definitions we have:

$$\alpha_{1(2)} = \frac{1}{2} \frac{\delta_{1(2)}^+ + \delta_{1(2)}^-}{\delta_{1(2)}^+ - \delta_{1(2)}^-}, \quad (7.2)$$

and

$$\beta_{1(2)} = \frac{\delta_{1(2)}^+ \delta_{1(2)}^-}{\delta_{1(2)}^- - \delta_{1(2)}^+}. \quad (7.3)$$

7.3 Rate equation approach

In order to calculate the current through the double dot system for any given (V, V_G) , one has to numerically solve the stationary solution of the master equation for dot 1(2)[3, 18]:

$$\frac{dP_n^{1(2)}}{dt} = \left(W_{n' \rightarrow n}^{1(2)} P_{n'}^{1(2)} - W_{n \rightarrow n'}^{1(2)} P_n^{1(2)} \right) = 0.$$

Here $W_{n \rightarrow n'}^{1(2)}$ is the rate for going from the unoccupied state, n , to the occupied state, n' , in dot 1(2), and $P_n^{1(2)}$ ($P_{n'}^{1(2)}$) is the occupation probability of state n (n'). The rates W are proportional to the coupling to the leads $\Gamma^{L,R}$ and the Fermi function f on the leads. In the case where an electron tunnels on or off dot 1(2), these rates are respectively:

$$\begin{aligned}W_{n \rightarrow n'}^{1(2)} &= \frac{\Gamma_{1(2)}^L}{\hbar} f_{1(2)}^L + \frac{\Gamma_{1(2)}^R}{\hbar} f_{1(2)}^R, \\ W_{n' \rightarrow n}^{1(2)} &= \frac{\Gamma_{1(2)}^L}{\hbar} (1 - f_{1(2)}^L) + \frac{\Gamma_{1(2)}^R}{\hbar} (1 - f_{1(2)}^R),\end{aligned}$$

where

$$f_{1(2)}^L = \frac{1}{e^{\frac{\tilde{\mu}_{1(2)} + n_{2(1)} E_{Cm} + \frac{1}{2}V}{k_B T}} + 1},$$

$$f_{1(2)}^R = \frac{1}{e^{\frac{\tilde{\mu}_{1(2)} + n_{2(1)} E_{Cm} - \frac{1}{2}V}{k_B T}} + 1}.$$

With the constraint that $P_n^{1(2)} + P_{n'}^{1(2)} = 1$, the average occupation for dot 1(2) is:

$$n_{1(2)} = \frac{\Gamma_{1(2)}^L f_{1(2)}^L + \Gamma_{1(2)}^R f_{1(2)}^R}{\Gamma_{1(2)}^L + \Gamma_{1(2)}^R}. \quad (7.4)$$

In order to calculate the total current for any given (V, V_G) , n_1 and n_2 must be first determined *self-consistently*. The current is then calculated using:

$$I = \frac{e}{\hbar} \left[\frac{\Gamma_1^L \Gamma_1^R}{\Gamma_1^L + \Gamma_1^R} (f_1^R - f_1^L) + \frac{\Gamma_2^L \Gamma_2^R}{\Gamma_2^L + \Gamma_2^R} (f_2^R - f_2^L) \right].$$

It's important to note that the current levels through dot 1 and 2 are set respectively by the pre-factors

$$I_1 = \frac{\Gamma_1^L \Gamma_1^R}{\Gamma_1^L + \Gamma_1^R}, \quad (7.5)$$

$$I_2 = \frac{\Gamma_2^L \Gamma_2^R}{\Gamma_2^L + \Gamma_2^R}, \quad (7.6)$$

which depend on the couplings to the leads. The broadening of the resonances on the other hand depends only on the temperature through the Fermi functions of the leads; this is known for the rate equation approach as it does not account for the broadening of the resonant levels as in the NEGF formalism. We note that this is an important detail when accounting for the line shapes of the observed features.

When comparing results calculated with this model with experimental data the electronic couplings and the coupling energy are free parameters which are varied to find the best resemblance. The gate (bias) couplings and the location of the charge degeneracy points are determined from the experimental conductance maps.

7.4 Comparison with experiments

In experiments on transport through molecular junctions, we often observe features (e.g., kinks in diamond edges and switches) that cannot be explained straightforwardly with

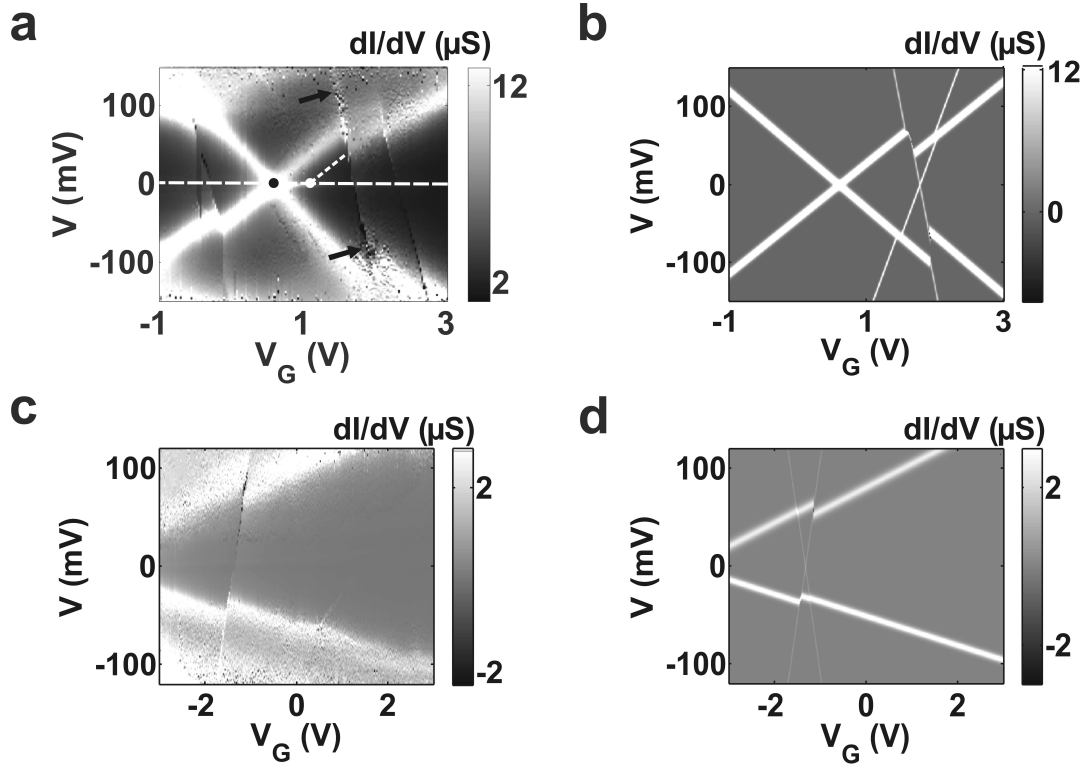


Figure 7.2: Examples of experimental data with “diagonal switches” (left) and their corresponding numerically calculated conductance maps (right). **a**, Measured conductance map at $T = 1.7$ K from a series of measurements carried out on the manganese complex discussed in chapter 5. **b**, Calculated conductance map for the experimental data in **a**. Only the “diagonal switch” pointed by black arrows in **a** was modeled. The fit-parameters are: $\alpha_1 = -0.014$, $\beta_1 = 0.037$, $\Gamma_1^L = \Gamma_1^R = 4$ meV, $\epsilon_1 = 22$ meV, $\alpha_2 = 0$, $\beta_2 = 0.231$, $\Gamma_2^L = 400$ μ eV, $\Gamma_2^R = 40$ meV, $\epsilon_2 = 381$ meV, and the electrostatic coupling energy is $E_{Cm} = 19$ meV. **c**, Same as in **a**, but from measurements carried out on the grid complex discussed in chapter 6. **d**, Numerical fit to the experimental data in **c**. The fit parameters are: $\alpha_1 = 0.117$, $\beta_1 = 0.009$, $\Gamma_1^L = \Gamma_1^R = 0.2$ meV, $\epsilon_1 = -36$ meV, $\alpha_2 = 0$, $\beta_2 = 0.161$, $\Gamma_2^L = 0.2$ meV, $\Gamma_2^R = 20$ μ eV, $\epsilon_2 = -220$ meV, and the electrostatic coupling energy is $E_{Cm} = 5$ meV.

a single dot model. In this section we discuss a few examples and show that they are well reproduced with the parallel double dot model presented above.

A first example of such a measurement is shown in figure 7.2a. A clear crossing point and broad diamond edges are visible which are interrupted by several steep diagonal lines. At the point of intersection a shift (switch) of the broad diamond edge occurs towards smaller bias voltages. An important observation here, is that the switch is not simply a translation of the conductance map along the gate axis: this would be the case for a charge trap in the vicinity of the junction which upon charging acts as an effective (sudden) change in gate voltage. Another important remark is that the position at which these steep diagonal lines occur is reproducible upon repeating the measurement. Furthermore, detailed measurements on these diagonal lines reveal that they belong to steep diamond edges in which one of the edges is not visible or appears very faintly.

In figure 7.2b we show the result of a calculation carried out with the parallel double dot model which reproduces the main features in figure 7.2a. We will now discuss the determination of the parameter range for which the calculation agrees with the experiment. The input for the calculation is the location of the main charge degeneracy point at $V_G = 0.65$ V (dot 1) and the position of the steep diagonal line (dot 2). The gate (bias) couplings are determined using Eqs. 7.2 and 7.3 together with the measured slopes of the diamond edges of each dot. We note that for the second dot, i.e., the steep diagonal line, the value of the positive slope is not crucial and has no effect on the output of the calculation: in this case it has been taken to be equal to the negative slope.

The remaining set of parameters in the calculation are the couplings to the leads for each dot, $\Gamma_{1(2)}^{L,R}$, and the electrostatic coupling energy E_{Cm} between the dots. The result of the calculation presented in figure 7.2b is obtained if (i) the ratio of the current levels between dot 2 and 1 is not larger than two orders of magnitude, i.e., $I_2/I_1 \not\ll 10^{-2}$ (see also Eqs. 7.5 and 7.6), and (ii) the electronic coupling of dot 2 to the left lead is at least a hundred times smaller than to the right lead, i.e., $\Gamma_2^L/\Gamma_2^R \leq 10^{-2}$. Overall, this means that the individual values of the couplings are not relevant as long as they fulfill the above conditions and give the current levels of the experimental data.

The only remaining parameter is the electrostatic coupling energy. To estimate E_{Cm} from the experimental data, one has to extrapolate the diamond edges as illustrated in figure 7.2a, after the switch has occurred, to the zero-bias axis and read the gate voltage at the crossing: the difference between this voltage and the gate voltage of the charge degeneracy point of dot 1, multiplied by the corresponding gate coupling gives an estimated value for E_{Cm} . One can understand this by taking a look at the mechanism of the switch itself. As extracted from the calculation, the average occupation of dot 2 on the left hand side of the steep diagonal line with negative slope is zero, and on the right hand side it is one. Therefore by crossing this line the average occupation increases by one and this is “felt” by dot 1 via the capacitive coupling between the dots as an effective gate voltage change which causes its ground state transition to be shifted upwards in energy; hence the displacement of the diamond edge of dot 1 which is proportional to E_{Cm} .

In figure 7.2c,d we show another measurement, with the corresponding numerically

calculated conductance map, in which steep diagonal lines and switching were observed. We note that the only difference with respect to the previous case is that in order to reproduce the experimental picture it is necessary to set $\Gamma_2^R/\Gamma_2^L \leq 10^{-2}$ (instead of $\Gamma_2^L/\Gamma_2^R \leq 10^{-2}$ as in the previous case). Therefore the asymmetry in couplings sets the slope the switch: whether along a negative or positive sloped line. We also note that in these calculations both diamond edges are visible for dot 2 whereas in the previous experiment only one of them is faintly visible. Furthermore as we shall see in the next section, the diamond edges possess particular line shapes different from a simple peak in the dI/dV . These are details the rate equation approach cannot account for, nevertheless it is quite remarkable that the simple model already qualitatively captures the experimental picture.

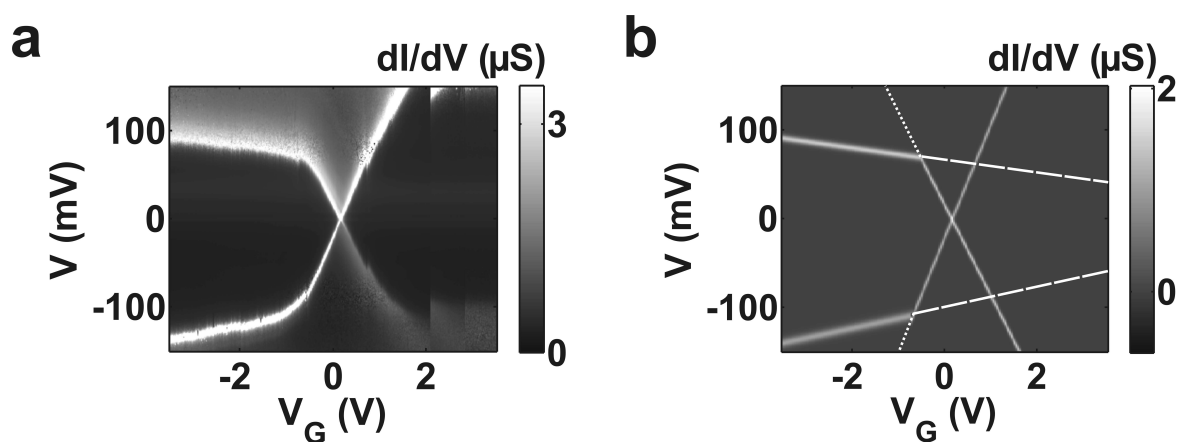


Figure 7.3: **a**, Measured conductance map at $T = 1.7$ K from a OPV-5 molecular junction. **b**, Calculated conductance map for the data in **a**. Dashed and dotted lines are not part of the calculation (see main text for discussion). The fit parameters are: $\alpha_1 = 0.054$, $\beta_1 = 0.057$, $\Gamma_1^L = \Gamma_1^R = 0.1$ meV, $\epsilon_1 = 8.5$ meV, $\alpha_2 = 0.103$, $\beta_2 = 0.004$, $\Gamma_2^L = \Gamma_2^R = 0.1$ meV, $\epsilon_2 = 40$ meV, and the electrostatic coupling energy $E_{Cm} = 120$ meV.

Another experimental feature which our double-dot model reproduces is a kink-like structure in the diamond edge, such as the one shown in figure 7.3a. The corresponding calculated map is presented in panel b. In this case, the steep diamond edges are attributed to conduction through dot 1 and the almost horizontal ones mark the onset of conduction through dot 2 which has a much lower gate coupling. In order to understand this picture we first describe what would have been the result of the calculation if capacitive coupling between the two dots were taken to be zero. In this case, the output would have given exactly the same conductance map with lines continuing where we have now extrapolated, as illustrated in figure 7.3b with dashed (dotted) lines. The charge degeneracy point of dot 2, the weakly coupled one, would have been located at the crossing of the dashed lines at approximately $V_G \approx 9$ V.

By turning “on” the capacitive coupling, shifts in ground states occur when one of the dots acquires a certain amount of charge (fractional or integer). This is clear on the right hand side of the visible charge degeneracy point, where dot 1 gets charged, and the ground

state transition of dot 2 shifts out of the bias range used in figure 7.3b. This transition is located at the dashed line position for $E_{Cm} = 0$. We note that in this calculation the electrostatic coupling energy, E_{Cm} , was adjusted such that none of the transitions indicated by dashed and dotted lines were visible any longer in the conductance map. Therefore the value of E_{Cm} represents a lower bound since any larger value would have given the same result. In the absence of more information, such as for instance the location of the charge degeneracy of dot 2, the value of this parameter cannot be fixed.

Finally, in order to reproduce the results in figure 7.3a we remark that the electronic couplings to the right and left lead should not differ by more than 50% for each dot. Since the conductance levels are more or less equal, the couplings for both dots were chosen to be the same in the calculation resulting in figure 7.3b, where their values are adjusted to match the current levels of the measurement.

Comparing the fit parameters to the previous switches (figure 7.2), we see that one of the gate couplings is small and that the mutual capacitance is larger. This generally holds for the appearance of “kinks” in this model. It is important to note that “kinks” in the diamond edge have been observed in measurements carried out with the different molecules investigated in the work presented in this thesis. Other examples can be found in figure 4.2a and figure 6.3a. This feature has also been observed in other systems such as metallic multigrain dots [1], epitaxial nanowires [19], semiconducting quantum dots [2, 20], and carbon nanotubes [21]. In alternative explanations, the appearance of these kinks is attributed to excited states of the dot with varying capacitances [21] or to replicas of Coulomb diamonds due to traps in the tunnel barriers of a single dot [2]. We note that the large difference in gate couplings (more than a factor 10 in figure 7.3) makes the former explanation unlikely in our molecular junctions. The lower gate coupling for one of the dots can then be explained by a larger distance from the Al_2O_x gate dielectric or screening of the gate potential by the leads.

As a last example, in figure 7.4a we show yet another set of experimental data that can be numerically reproduced with the double dot model. We observe a poorly gated coupled dot (almost horizontal line) which crosses the SET region of a second dot displaying a clear crossing point at $V_G = 1.3$ V. Going from right to left, we see that as soon as the diamond edge of the first dot hits the diamond edge of the second one, it shifts downwards. To reproduce such a picture from our model we extract from the data the gate (bias) couplings, the position of the charge degeneracy points, and an estimation of E_{Cm} , as discussed before.

For the first dot, the weakly coupled one, the positively sloped diamond edge, which is not visible in figure 7.4a, is taken such that it does not appear in the calculated conductance map; therefore an arbitrary value has been assigned for this slope when calculating the gate coupling (see Eq. 7.3). The location of the charge degeneracy point of dot 2 is determined by extrapolating the visible diamond edge to the zero-bias axis. An estimation of E_{Cm} is given by the diamond edge displacement, Δ (see figure 7.4), multiplied by the corresponding gate coupling of dot 1.

With respect to the electronic couplings the following conditions apply when reproducing the experimental data: (i) $\Gamma_1^L/\Gamma_1^R \geq 10$ and (ii) $\Gamma_2^L/\Gamma_2^R \leq 10^{-1}$. This means that the

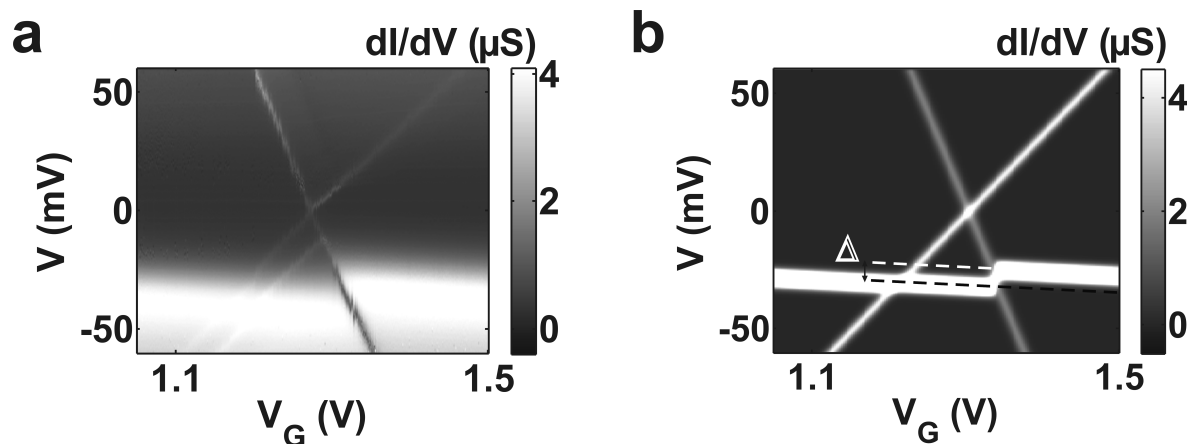


Figure 7.4: **a**, Measured conductance map at $T = 1.7$ K from a Grid molecular junction. **b**, Numerically calculated conductance map of the data in **a**. The fit parameters are: $\alpha_1 = 0.454$, $\beta_1 = 0.015$, $\Gamma_1^L = 20$ meV, $\Gamma_1^R = 200$ μeV , $\epsilon_1 = -11$ meV, $\alpha_2 = -0.201$, $\beta_2 = 0.235$, $\Gamma_2^L = 2$ μeV , $\Gamma_2^R = 2$ meV, $\epsilon_2 = 299$ meV, and the electrostatic coupling energy is $E_{Cm} = 8$ meV.

lead to which the two dots couple strongly is different for the two dots; i.e., dot 1 couples strongly to the source and dot 2 to the drain or vice versa. Setting a strong coupling to the same lead for both dots changes the position at which the diamond edge of dot 1 shifts upwards; it would then occur at the positive sloped diamond edge of dot 2 instead of the negative sloped edge as in figure 7.4a.

7.5 Non-equilibrium Green's function approach

Figure 7.5a gives a high resolution dI/dV map of the steep diagonal line indicated by black arrows in figure 7.2a. We observe a zero-bias Kondo resonance on both sides of the charge degeneracy point (which we will not consider here since it is a second order process) and also, very faintly, the second diamond edge with positive slope. In figure 7.5b we plot the dI/dV versus V_G trace across the steep diagonal line both at positive and negative bias. The line shape appears to be bias dependent: at positive bias it has the structure of a sharp asymmetric peak while at negative bias it exhibits a dip.

With the rate equation approach it is not possible to fit these line shapes. Therefore we turn to a more sophisticated approach which uses the non-equilibrium Green's functions (NEGF) method; the method will not be outlined in this thesis and we refer to a forthcoming publication for this. With this approach the system and the number of parameters remain the same; the only difference is the way the current is calculated. As with the rate equation approach, the gate (bias) couplings and the charge degeneracy points for both dots are determined from figure 7.2a. An estimation of the electronic couplings, Γ , and the coupling energy, E_{Cm} , is also extracted from the data. For the former, the width of the respective resonances for each dot is determined. The final result of the calculation is

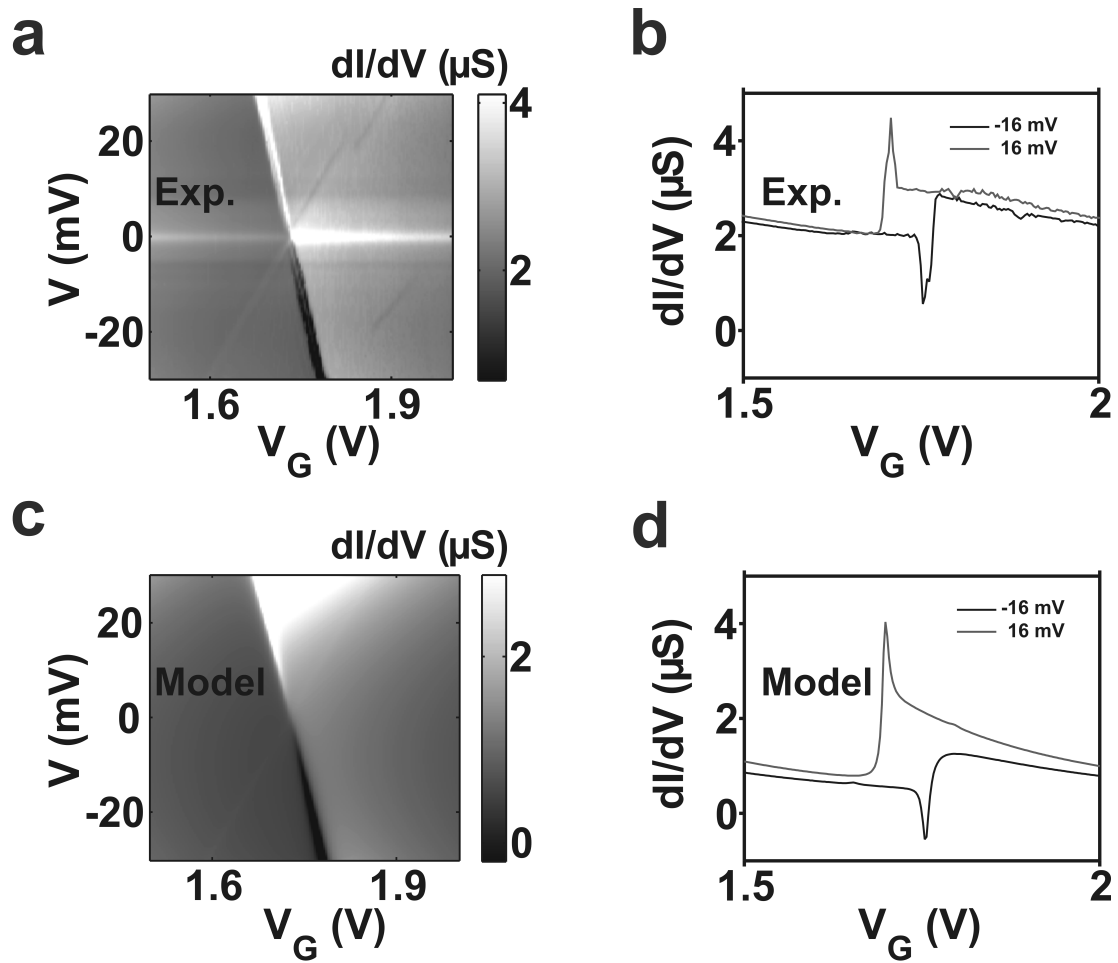


Figure 7.5: **a**, Expanded view of the diagonal line pointed by arrows in figure 7.2. **b**, dI/dV versus V_G traces at $V = \pm 16$ mV taken from **a**. **c**, Numerical calculated map of **a** using the NEGF formalism. The fit-parameters are: $\alpha_1 = -0.072$, $\beta_1 = 0.048$, $\Gamma_1^L = \Gamma_1^R = 6$ meV, $\epsilon_1 = 31$ meV, $\alpha_2 = -0.220$, $\beta_2 = 0.160$, $\Gamma_2^L = 0.7$ μeV , $\Gamma_2^R = 2$ meV, $\epsilon_2 = 254$ meV, and the electrostatic coupling energy is $E_{Cm} = 22$ meV. **d**, dI/dV versus V_G traces at $V = \pm 16$ mV taken from **c**.

shown in figure 7.5c for the calculated conductance map. As we can see in figure 7.5d the model reproduces the line shapes and the experimental conductance map shown in figure 7.5a well.

References

- [1] A. V. Danilov, D. S. Golubev, and S. E. Kubatkin, “Tunneling through a multi-grain system: Deducing sample topology from nonlinear conductance,” *Phys. Rev. B*, vol. 65, no. 12, p. 125312, 2002.
- [2] M. Pierre, M. Hofheinz, X. Jehl, M. Sanquer, G. Molas, M. Vinet, and S. Deleonibus, “Offset charges acting as excited states in quantum dots spectroscopy,” *cond-mat.*, no. 0810.0672v1, 2008.
- [3] E. Bonet, M. M. Deshmukh, and D. C. Ralph, “Solving rate equations for electron tunneling via discrete quantum states,” *Phys. Rev. B*, vol. 65, no. 4, p. 045317, 2002.
- [4] J. König and Y. Gefen, “Aharonov-Bohm interferometry with interacting quantum dots: Spin configurations, asymmetric interference patterns, bias-voltage-induced aharonov-bohm oscillations, and symmetries of transport coefficients,” *Phys. Rev. B*, vol. 65, no. 4, p. 045316, 2002.
- [5] A. W. Holleitner, C. R. Decker, H. Qin, K. Eberl, and R. H. Blick, “Coherent coupling of two quantum dots embedded in an Aharonov-Bohm interferometer,” *Phys. Rev. Lett.*, vol. 87, no. 25, p. 256802, 2001.
- [6] A. S. Adourian, C. Livermore, R. M. Westervelt, K. L. Campman, and A. C. Gossard, “Evolution of Coulomb blockade spectra in parallel coupled quantum dots,” *Appl. Phys. Lett.*, vol. 75, no. 3, pp. 424–426, 1999.
- [7] J. C. Chen, A. M. Chang, and M. R. Melloch, “Transition between quantum states in a parallel-coupled double quantum dot,” *Phys. Rev. Lett.*, vol. 92, no. 17, p. 176801, 2004.
- [8] L. G. G. V. D. da Silva, N. P. Sandler, K. Ingersent, and S. E. Ulloa, “Zero-field Kondo splitting and quantum-critical transition in double quantum dots,” *Phys. Rev. Lett.*, vol. 97, no. 9, p. 096603, 2006.
- [9] R. López, R. Aguado, and G. Platero, “Nonequilibrium transport through double quantum dots: Kondo effect versus antiferromagnetic coupling,” *Phys. Rev. Lett.*, vol. 89, no. 13, p. 136802, 2002.
- [10] C.-H. Chung and W. Hofstetter, “Kondo effect in coupled quantum dots with RKKY interaction: Effects of finite temperature and magnetic field,” *Phys. Rev. B.*, vol. 76, no. 4, p. 045329, 2007.

- [11] Y. Tanaka and N. Kawakami, “Interference effects on Kondo-assisted transport through double quantum dots,” *Phys. Rev. B.*, vol. 72, no. 8, p. 085304, 2005.
- [12] I. H. Chan, P. Fallahi, R. M. Westervelt, K. D. Maranowski, and A. C. Gossard, “Capacitively coupled quantum dots as a single-electron switch,” *Physica E.*, vol. 17, pp. 584 – 588, 2003.
- [13] I. H. Chan, R. M. Westervelt, K. D. Maranowski, and A. C. Gossard, “Strongly capacitively coupled quantum dots,” *Applied Physics Letters*, vol. 80, no. 10, pp. 1818–1820, 2002.
- [14] F. Hofmann, T. Heinzl, D. Wharam, J. Kotthaus, G. Böhm, W. Klein, G. Tränkle, and G. Weimann, “Single electron switching in a parallel quantum dot,” *Phys. Rev. B*, vol. 51, no. 19, pp. 13872–13875, 1995.
- [15] M. R. Galpin, D. E. Logan, and H. R. Krishnamurthy, “Dynamics of capacitively coupled double quantum dots,” *J. Phys.: Condens. Matter.*, vol. 18, no. 29, pp. 6571–6583, 2006.
- [16] F. Chi and S.-S. Li, “Interdot interaction induced zero-bias maximum of the differential conductance in parallel double quantum dots,” *J. Appl. Phys.*, vol. 99, no. 4, p. 043705, 2006.
- [17] W. G. van der Wiel, S. De Franceschi, J. M. Elzerman, T. Fujisawa, S. Tarucha, and L. P. Kouwenhoven, “Electron transport through double quantum dots,” *Rev. Mod. Phys.*, vol. 75, no. 1, pp. 1–22, 2002.
- [18] C. W. J. Beenakker, “Theory of Coulomb-blockade oscillations in the conductance of a quantum dot,” *Phys. Rev. B*, vol. 44, no. 4, pp. 1646–1656, 1991.
- [19] Z. Zhong, Y. Fang, W. Lu, and C. M. Lieber, “Coherent single charge transport in molecular-scale silicon nanowires,” *Nano. Lett.*, vol. 5, no. 6, pp. 1143–1146, 2005.
- [20] T. H. Oosterkamp, J. W. Janssen, L. P. Kouwenhoven, D. G. Austing, T. Honda, and S. Tarucha, “Maximum-density droplet and charge redistributions in quantum dots at high magnetic fields,” *Phys. Rev. Lett.*, vol. 82, no. 14, pp. 2931–2934, 1999.
- [21] S. J. Tans, M. H. Devoret, R. J. A. Groeneveld, and C. Dekker, “Electron-electron correlations in carbon nanotubes,” *Nature*, vol. 394, no. 6695, pp. 761–764, 1998.

Summary

Quantum transport through single molecules

This thesis describes three-terminal transport measurements through single molecules. The interest in this field stems from the dream that *single* molecules will form the building blocks for future nanoscale electronic devices. The advantages are their small size -nanometers-, and their synthetic tailorability which allows the molecules to be designed with built-in functionality. Many efforts in experimental research are nowadays devoted to understand electrical transport through single molecules. Several techniques are used for this purpose: scanning tunneling microscopy (STM), mechanical controllable break junctions (MCBJ), atomic force microscopy (AFM), and shadow evaporation; we discuss some of these in chapter 2. In that chapter we also discuss in detail the method used throughout this thesis to fabricate nanogaps, namely electromigration. We show that after trapping a molecule in the nanogap, a molecule at low temperatures behaves as a quantum dot (QD), i.e., a system where electrons can be placed in discrete energy states. The control over the number of electrons that can sit on the molecule is achieved by the voltage on a third electrode, the gate, which is capacitively coupled to the QD. Transport measurements, which consist of taking current-voltage characteristics as a function of this gate voltage, reveal important spectroscopic information about the molecule.

The first molecule we studied is a rod-like structure consisting of five aromatic building blocks (OPV-5). In this type of molecules, an alternating sequence of single and double bonds forms a delocalized-electron system over the whole length, making this system a so-called molecular wire. Earlier experiments by others, conducted on the same type of molecule showed that the properties of the molecule are drastically changed when connected to metal electrodes. The transport measurements revealed a HOMO-LUMO gap and addition energies which are an order of magnitude smaller than the HOMO-LUMO gap of the isolated molecule. Our measurements provide the first independent experimental evidence that the addition energies are indeed reduced; however, we were not able to perform a direct measurement of the HOMO-LUMO gap. In addition, our data presented in chapter 3 shows clear evidence of vibrational excitations induced by phonon-scattering in the molecular junction, consistent with spectroscopic vibrational excitations of OPV-5 determined by IR and Raman techniques.

In the next chapter, we show that as the transparency of the tunneling barriers at the molecule-lead interface increases, higher-order tunnelling processes also become important.

An example of such a process is the Kondo effect which enhances the conductance at zero bias. This intermediate transparency regime is studied in chapter 4 for an OPV-5 molecular junction. The dependence of the cotunneling features as a function of temperature and magnetic field allows us to infer the charge-filling sequence, i.e., how charges are added one by one. Furthermore, the charge-dependent couplings to gate, source and drain electrodes suggest a scenario in which charges and spins are localized at the ends of the molecule, close to the electrodes.

In chapter 5, we study transport through another type of molecular system in which a *Mn*-ion is surrounded on either side by ligands. Besides their vast importance in bio-inorganic chemistry, this class of molecules is particularly interesting for future molecular-spintronic devices. The transport measurements presented in chapter 5 occur in the intermediate coupling regime and show that by changing the gate voltage the spin ground-state of the molecule can be tuned. To understand this finding the molecule is viewed as a system divided in three sub-units: two ligands plus the metal ion. Due to differences in coupling to the electrostatic-gate field, the orbitals in these three different units “shift” at different rates with the gate voltage. We find that the electronic configuration of the ground state, and thus the resulting spin of the system depends on the gate field. Hence, the gate provides an additional “knob” for controlling the spin of single-molecule devices.

Switching in molecular junctions is a topic which has attracted a lot of attention. Not only from a fundamental point of view it is interesting, but also from a practical one; in future applications molecular junctions should be able to perform basic electronic functions such as switching. Although switching has been observed in numerous experiments, the nature of the mechanism itself remains controversial: conformational changes, molecule-bond fluctuations, and charge traps are among the proposed mechanisms. In chapter 6, we study transport through a grid type molecule, which can undergo a maximum number of twelve reduction-waves in cyclic voltammetry studies; this indicates that up to 12 electrons can be put onto the molecule. The transport measurements occur in the weak coupling regime and show a particular type of switching behavior. The gate (bias) dependence of the switching suggests that the cause of this effect is electrostatic in nature. We notice that a similar switching behavior is observed in measurements carried out with the *Mn*-complex studied in chapter 5, however, it has never been observed with OPV-5. We suspect that counter-ions, which are present in the grid and manganese compound but absent in the OPV-5, remain after deposition in the vicinity of the molecular junction. When these counter-ions move around they effectively act as moving offset charges for the molecular quantum dot; sudden changes in their position then leads to abrupt switching events in the response of the molecules.

In experiments on transport through molecular junctions, we often observe features (e.g., kinks in the Coulomb-diamond edges or switches) that cannot straightforwardly be explained with a single quantum dot model. The last chapter of this thesis is devoted to a comparison of experimental data with calculations based on a parallel double-quantum-dot model which reproduce these features. We make use of the rate-equation approach and only take into consideration capacitive coupling between the two quantum dots. To account for the line shapes of the observed features we use a more sophisticated approach to calculate

the current through the double-dot system: the non-equilibrium Green's function (NEGF) formalism. A good agreement with the data is found.

Edgar Alberto Osorio Oliveros
February, 2009

Samenvatting

Kwantum transport door een enkel molecuul

Dit proefschrift beschrijft *three-terminal* transportmetingen door een enkel molecuul. De interesse in dit onderzoeksgebied komt voort uit de droom dat moleculen de bouwstenen zullen worden voor toekomstige elektronische systemen op nanoschaal. De voordelen die ze hebben zijn de kleine afmeting – nanometers – en de mogelijkheid om ze te ontwerpen met ingebouwde functionaliteit. Veel inspanningen in experimenteel onderzoek zijn tegenwoordig gericht op het begrijpen van elektrisch transport door een enkel molecuul. Hiervoor worden verscheidene technieken gebruikt: *scanning tunneling microscopy* (STM), *mechanically controllable break junctions* (MCBJ), *atomic force microscopy* (AFM) en *shadow evaporation*; we bespreken enkele van deze in hoofdstuk 2. In dat hoofdstuk bespreken we ook in detail de methode die gedurende dit proefschrift gebruikt is om nano-openingen te fabriceren, namelijk elektromigratie. We laten zien dat na het opsluiten van een molecuul in de nano-opening, een molecuul zich bij lage temperatuur gedraagt als een kwantumeiland, d.w.z. een systeem waarin elektronen in discrete energietoestanden geplaatst kunnen worden. Controle over het aantal elektronen dat op het molecuul kunnen zitten, wordt verkregen door de spanning op een derde elektrode, de *gate*, welke capacitief gekoppeld is aan het kwantumeiland. Transportmetingen, welke bestaan uit het bepalen van stroom-spanning karakteristieken als functie van de *gate*-spanning, onthullen belangrijke spectroscopische informatie over het molecuul.

Het eerste molecuul dat we bestudeerd hebben met deze methode in dit proefschrift is een staafachtige structuur bestaande uit vijf aromatische bouwstenen (OPV-5). Een afwisselende reeks van enkele en dubbele bindingen vormt in dit type moleculen een gede-localiseerd elektron systeem over de gehele lengte, wat dit systeem een zogeheten moleculaire draad maakt. Eerdere experimenten, uitgevoerd door anderen op hetzelfde type molecuul hebben aangetoond dat de eigenschappen van het molecuul drastisch worden veranderd als het verbonden is aan metaalelektroden. De transportmetingen onthulden een *HOMO-LUMO gap* en additie-energieën welke een orde van grootte kleiner zijn dan de *HOMO-LUMO gap* van het gesoleerde molecuul. Onze metingen geven het eerste onafhankelijke experimentele bewijs dat de additie-energieën inderdaad verminderd worden. We waren echter niet in staat een directe meting van de *HOMO-LUMO gap* uit te voeren. Daarnaast laat de data die in hoofdstuk 3 gepresenteerd wordt, duidelijk bewijs zien van trillingsexcitaties welke veroorzaakt worden door fonon-verstrooiing in de moleculaire

junctie, consistent met de spectroscopische trillingsexcitaties van OPV-5 als bepaald met IR en Raman technieken.

In het volgende hoofdstuk laten we zien dat als de transparantie toeneemt van de tunnelbarrières op het grensvlak van het molecuul en het contact, tunnelprocessen van hogere orde ook van belang worden. Een voorbeeld van een dergelijk proces is het Kondo effect, dat de geleiding zonder aangelegde spanning verhoogt. Dit tussengebied van transparantie wordt bestudeerd in hoofdstuk 4 voor een OPV-5 moleculaire junctie. De afhankelijkheid van de cotunnelkenmerken als functie van de temperatuur en het magneetveld maken het voor ons mogelijk om af te leiden hoe ladingen één voor één toegevoegd worden. Bovendien suggereert de ladingsafhankelijke koppeling aan de *gate*-, *source*- en *drain*-elektroden een scenario waarin ladingen en spins gelokaliseerd zijn op de uiteinden van het molecuul, vlakbij de elektroden.

In hoofdstuk 5 bestuderen we transport door een ander type moleculair systeem, waarin een *Mn*-ion aan beide zijden omgeven wordt door liganden. Naast het feit dat deze klasse van moleculen van groot belang is in bio-anorganische scheikunde, zijn deze systemen bijzonder interessant voor toekomstige moleculaire *spintronic devices*. De transportmetingen die in hoofdstuk 5 gepresenteerd worden, vinden plaats in het tussengebied van koppeling en laten zien dat het veranderen van de *gate*-spanning de spin-grondtoestand van het molecuul kan afstemmen. Om deze bevinding te begrijpen wordt het molecuul beschouwd als een systeem dat verdeeld is in drie sub-onderdelen: twee liganden plus het metaalion. Vanwege verschillen in koppeling aan het elektrostatische *gate*-veld, ‘verschuiven’ de orbitalen in deze drie onderdelen in verschillende mate met de *gate*-spanning. We hebben vastgesteld dat de elektronische configuratie van de grondtoestand, en dus de resulterende spin van het systeem, afhangt van het *gate*-veld. Derhalve voorziet de *gate* in een extra ‘knop’ voor het regelen van de spin van enkel-molecuul systemen.

Schakelen in moleculaire juncties is een onderwerp wat een hoop aandacht heeft weten te trekken. Niet alleen vanuit een fundamenteel oogpunt is het interessant, maar ook vanuit praktisch oogpunt, omdat in toekomstige toepassingen een moleculaire junctie in staat zou moeten zijn om elektronische basisfuncties zoals schakelen uit te voeren. Hoewel schakelen in talloze experimenten is waargenomen, blijft de aard van het mechanisme zelf controversieel: veranderingen in conformatie, fluctuaties in molecuulbinding en ladingsvallen behoren tot de voorgestelde mechanismen. In hoofdstuk 6 bestuderen we transport door een rastermolecuul, welke een maximumaantal van twaalf reductiestappen kan ondergaan in cyclische voltametrie studies; dit geeft aan dat er tot 12 elektronen op het molecuul geplaatst kunnen worden. De transportmetingen zijn in het regime van zwakke koppeling en laten een bepaald type schakelgedrag zien. De *gate*-(*bias*-) afhankelijkheid van het schakelgedrag suggereert dat de oorzaak elektrostatisch van aard is. We merken op dat een soortgelijk schakelgedrag waargenomen is in de metingen uitgevoerd met het *Mn*-complex bestudeerd in hoofdstuk 5, maar nooit waargenomen is met OPV-5. We vermoeden dat tegenionen, welke aanwezig zijn in het raster- en mangaan compound, maar afwezig in OPV-5, in de nabijheid blijven van de moleculaire junctie na depositie. Als deze tegenionen heen en weer bewegen, gedragen ze zich effectief als bewegende offset ladingen voor het moleculaire kwantumeiland; plotselinge veranderingen in hun positie leiden tot abrupte

schakel-gebeurtenissen in de reactie van de moleculen.

In experimenten waarin transport door moleculaire juncties wordt gemeten, nemen we vaak kenmerken waar (bijv. schakelen of knikken in Coulomb-diamond randen) die niet eenvoudig uitgelegd kunnen worden met een model van een enkel kwantumeiland. Het laatste hoofdstuk van dit proefschrift is gewijd aan een vergelijking van experimentele data met berekeningen gebaseerd op een parallel dubbel-kwantumeiland model wat deze kenmerken kan reproduceren. We maken gebruik van de rate-vergelijking methode en we nemen alleen capacitieve koppeling tussen de twee eilanden mee in de beschouwing. Om de lijnvorm van de waargenomen kenmerken te verklaren, maken we gebruik van een meer verfijnde aanpak om de stroom door het dubbel-kwantumeiland systeem te berekenen: het formalisme van non-equilibrium Green's functions (NEGF). Er wordt een goede overeenkomst met de data gevonden.

Edgar Alberto Osorio Oliveros
Februari, 2009

Curriculum Vitae

Edgar Alberto OSORIO OLIVEROS

- 05-11-1979 Born in Cali, Colombia.
- 1984-1997 Primary and secondary school, Lycée Français Paul Valéry, Cali, Colombia.
- 1998-2004 M.Sc. Physics,
University of Orsay, Paris, France.
Graduate research in the group of prof. dr. ir. B. J. van Wees.
Subject: Spin transport through carbon nanotubes.
- 2004-2008 Ph.D. research at Delft University of Technology.
Supervision by prof. dr. ir. H. S. J van der Zant.
Subject: Quantum transport through single molecules.

List of Publications

1. *Three-terminal transport measurements through metal nano particles combined with ex-situ TEM inspection.*
B. Gao, E. A. Osorio, K. B. Gaven, and H. S. J. van der Zant.
To be submitted to Nanotechnology (2009).
2. *Room-temperature stability of Pt nanogaps formed by self-breaking.*
F. Prins, B. J. A. de Vos van Steenwijk, B. Gao, E. A. Osorio, and H. S. J. van der Zant.
Submitted to Applied Physics Letters (2009).
3. *Electrical manipulation of spin states in a single gated transition-metal complex.*
E. A. Osorio, K. Moth-Poulsen, H. S. J. van der Zant, J. Paaske, P. Hedegård, K. Flensberg, J. Bendix, and Thomas Bjørnholm.
Submitted to Nature (2009).
4. *Single-molecule transport in three-terminal devices.*
E. A. Osorio, T. Bjørnholm, J. M. Lehn, M. Ruben, and H. S. J. van der Zant.
J. Phys.:Condens. Matter. **20**, 374121 (2008).
5. *Electronic excitations of a single molecule contacted in a three-terminal configuration.*
E. A. Osorio, K. O'Neill, M. Wegewijs, N. Stuhr-Hansen, J. Paaske, T. Bjørnholm, and H.S.J. van der Zant.
Nano. Lett. **7**, 3336 (2007).
6. *Self-breaking in planar few-atom au constrictions for nanometer-spaced electrodes.*
K. O'Neill, E. A. Osorio, and H. S. J. van der Zant.
Appl. Phys. Lett. **90**, 133109 (2007).
7. *Addition Energies and Vibrational Fine Structure Measured in Electromigrated Single-Molecule Junctions Based on an Oligophenylenevinylene Derivative*
E. A. Osorio, K. O'Neill, N. Stuhr-Hansen, O. F. Nielsen, T. Bjørnholm, and H. S. J. van der Zant.
Adv. Mater. **19**, 281 (2007).
8. *Electromigrated molecular junctions.*
H. S. J. van der Zant, E. A. Osorio, M. Poot, and K. O'Neill.
Phys. Stat. Sol. (b)**243**, 3408 (2006).
9. *Temperature dependence of three-terminal molecular junctions with sulfur end-functionalized tercylohexylidenes.*

M. Poot, E. Osorio, K. O'Neill, J. M. Thijssen, D. Vanmaekelbergh, C. A. vanWalree, L. W. Jenneskens, and H. S. J. van der Zant.
Nano. Lett. **6**, 1031 (2006).